Thesis

Anomalous electron hydrodynamics in noncentrosymmetric materials

---

Riki Toshio

Abstract

Recent remarkable developments of experimental techniques, such as microfabrication and quantum sensing with diamond nitrogen-vacancy centers, have opened up a new non-equilibrium regime of electronic dynamics in solids, dubbed the *hydrodynamic regime*. It is believed to be realized in clean metals/semiconductors with high conductivity and strong electronic correlations, where the electronic dynamics is described in the framework of *electron hydrodynamics*. Interestingly, in the novel regime, electron systems exhibit a variety of fascinating and unconventional transport phenomena, such as the Gurzhi effect, negative nonlocal resistance, preturblent-induced current fluctuation, and negative magnetoresistance. Since these phenomena originate from the nonlocality due to the electron viscosity and the nonlinearlity of the fluid dynamics, they are considered to characterize electron dynamics in the hydrodynamic regime.

In recent years, hydrodynamic signatures mentioned above have been confirmed through transport experiments in various clean materials, including GaAs quantum wells, 2D monovalent layered metal $PdCoO_2$, monolayer/bilayer graphene, and Weyl semimetal WP_2. Furthermore, because the hydrodynamic approach gives us clear and intuitive understading of the cross-interaction between various quasiparticles, such as magnons and phonons, and nonlocal/nonlinear optical response, its applications to the field of spintronics and plasmonics has also begun to be discussed. For these reasons, electron hydrodynamics has been attracting much interest in recent years and is quickly growing into a mature field of condensed matter physics.

More recently, symmetry of crystals and quantum geometry give a new twist to the concept of electron hydrodynamics. These aspects are irrelavant to usual fluids such as water, and thus clearly highlight the difference between electron fluids in crystals and conventional fluids. In fact, enthusiastic researches in the last few years have clarified rich and novel hydrodynamic phenomena, such as anisotropic viscosity effects and anomalous collective modes.

In this thesis, we focus on electron fluids in noncentrosymmetric crystals and clarify a variety of hydrodynamic phenomena peculiar to the systems. Our main purpose in this thesis can be summarized as follows:

1. Formulation of an electron hydrodynamic theory in noncentrosymmetric crystals.

2. Proposal of novel hydrodynamic phenomena peculiar to noncentrosymmetric systems and observables with existing experimental technologies.

3. Application of the obtained hydrodynamic theories to novel plasmonic devices.

Specifically, this thesis includes some brief introductions to the topics required to understand our work, including electron hydrodynamics and plasmonics, and the following research results:

Formulation of an anomalous hydrodynamic theory in nocentrosymmetric systems (Chapter 3) —— Focusing on the crystal symmetry (especially inversion symmetry) and the geometrical properties of the Bloch electrons, we have investigated what roles these factors play in hydrodynamic transport in noncentrosymmetric materials. To this end, we have formulated an anomalous hydrodynamic theory for noncentrosymmetric electron fluids, starting from the Boltzmann equation and the semiclassical equations. In the obtained theory, quantum geometrical effects appear as anomalous driving forces on electron fluids, leading to various anomalous transport phenomena. Based on this framework, we have proposed a novel type of hydrodynamic flows, dubbed asymmetric Poiseuille flow and anomalous edge current, which would be detectable with state-of-the-art experimental techniques. Moreover, we have provided group-theoretic analyses to classify the classes of electron fluids, and we have specified experimental setups where novel anomalous hydrodynamic flow mentioned above can be realized.

Analysis of plasmonically-driven geometical photocurrent in plasmonic devices (Chapter 4) —— We have investigated an interplay between quantum geometrical effects and surface plasmons through surface plasmonic structures, based on an anomalous hydrodynamic theory formulated in Chap. 3. Specifically, we have discussed how plasmonic resonances modulate photogalvanic effects originating from quantum geometrical effects. As a result, we have clarified that the quantum nonlinear Hall effect can be dramatically enhanced over a very broad range of frequency by utilizing plasmonic resonances and near-field effects of grating gates. We have further clarified a universal relation between the optical absorption and the amplitude of photocurrent induced by the Berry curvature dipole. This relation is essential for computational material design of long-wavelength photodetectors. Moreover, We have discussed a novel type of geometrical photocurrent driven by oscillating magnetic fields, which is related with the orbital magnetic moment of Bloch wavepackets. These findings might provide us with a promising route toward a novel type of highly sensitive, broadband terahertz photodetectors.

Contents

List of publications

Papers related to the thesis

1. **Riki Toshio**, Kazuaki Takasan, and Norio Kawakami
   "Anomalous Hydrodynamic Transport in Interacting Noncentrosymmetric Metals"
   Phys. Rev. Research **2**, 032021(R) (2020).

2. **Riki Toshio** and Norio Kawakami
   "Plasmonic quantum nonlinear Hall effect in noncentrosymmetric 2D materials"
   Phys. Rev. B 106, L201301 (2022).

Papers not included in the thesis

1. Ryotaro Sano, **Riki Toshio**, and Norio Kawakami
   "Nonreciprocal electron hydrodynamics under magnetic fields: Applications to nonreciprocal surface magnetoplasmons"
   Phys. Rev. Research **2**, 032021(R) (2021).

2. Hiroshi Funaki, **Riki Toshio**, and Gen Tatara
   "Vorticity-induced anomalous Hall effect in an electron fluid"
   Phys. Rev. Research **3**, 033075 (2021).

Chapter 1

Electron Hydrodynamics

In this chapter, we introduce the concept of *electron hydrodynamics*, which is the main topic throughout this thesis, and provide a brief review of its historical background and current studies for this issue. First, in Sec. 1.1, we mention the diversity of nonequilibrium phenomena in solids, and point out that they can be roughly divided into three nonequilibrium regime. Especially, through this discussion, we can clarify the importance of electron hydrodynamics. In the next section (Sec. 1.2), we explain what materials realize the hydrodynamic regime and what novel phenomena are observable in such materials, overviewing recent experiments. Furthermore, in Sec. 1.3, we also give a overview of recent theoretical developments in this context. Finally, in Sec. 1.4, we suggest several open problems in electron hydrodynamics, and present our goals in this thesis.

1.1 Hierarchical structure in electron dynamics

Non-equilibrium phenomena in solids have ever been fascinating a lot of condensed matter physicists. In the past decades, we have been witnessed remarkably rapid progress in the context, which ranges from amazing discoveries in the 20th century, such as superconductivity, Anderson localization, the Kondo effect, the quantum Hall effect, and photo-induced phase transitions, to modern topics including quantum chaos, many-body localization, high harmonic generation, photo-induced superconductivity. These researches privide us with not only deep insights into quantum properties, such as topology, entanglement, and quantum coherence, but also a variety of novel functional devices such as optics, spintronics, and valleytronics.

Now a natural question is why non-equilibrium phenomena in solids are so diverse and complex. Of course, we do not know the complete answer to the question, since it will strongly depend on problems at hand, but an important clue to it might be found in the *temporospatial hierarchical structure* in the microscopic dynamics, which is created by the interplay between the various indepedent degrees of freedom. To illustrate this, in Fig 1.1, we shows the momentum flow in a solid accompanied with various scattering processes. In general, quasi-particles in solids, such as electrons and phonons, are constantly exposed to various scattering processes. Each of these scattering processes has its own characteristic time and length scale, and especially, the shortest one, i.e., the most dominant scattering process, plays an important role in providing an effective description of electron dynamics. As easily imagined, it is generally a very difficult problem to determine which scattering processes are the major contributors to the phenomena at hand. However, as long as we blindly analyze the dynamics of all the degrees of freedom, we can never reveal the universal description of non-equilibrium phenomena in solids.

For example, we can understannd most of transport phenomena in conventional metals

(a) Momentum flow in general

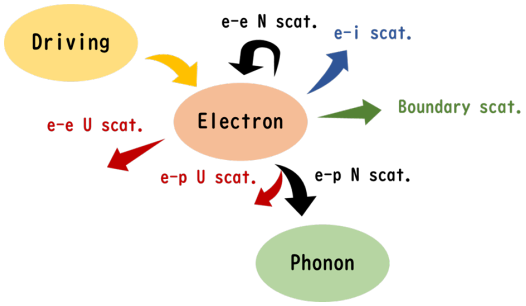

(b) Momentum flow in the hydrodynamic regime

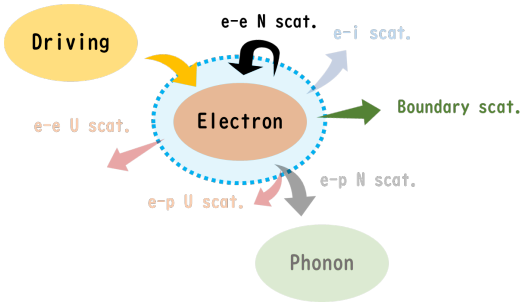

Figure 1.1: Schematic diagram of momentum flow in solids. We have shown typical scattering processes and associated momentum flows in solids. In particular, the scattering process shown in black is a process that conserves the crystal momentum of the entire system. In reality, these scattering processes are further subdivided into some processes depending on the degrees of freedom (valley, spin, orbital) of the electron systems and the characters of phonon modes. (b) Schematic diagram of the momentum flow in the hydrodynamic regime. In the hydrodynamic regime, normal electron-electron scattering is the most dominant, and the momentum of the electron system is regarded as an approximately conserved quantity. In the Poiseuille flow, the boudary scatterings are the main origin of the momentum dissipation.

or semiconductors by using a quite simplified approximation where we ignore the contributions of electron-electron scattering and finite-size effects, and treat momentum-relaxing scattering processes, such as electron-impurity scattering and electron-phonon scattering, within the relaxation-time approximation. Such a prescription is allowed (at least in a qualitative level) for many bulk materials, and actually have ever had a lot of success [1, 2]. In the intuitive picture of electron dynamics, we regard an electron wave packet in a solid as a ball and scatterers as a pinball, as shown in the left of Fig. 1.2. In the simplest case, this problem is described by the Drude theory [1], and we refer to such a non-equilibrium region as the *Ohmic region* in this thesis.

On the other hand, mesoscopic physics, represented by various quatnum trasnport such as the Aharanov-Bohm effect, weak localization, and universal conductivity fluctuation, usually focus on another non-equilibrium regime where decoherent scattering processes, including electron-electron scattering and phonon scattering, are small enough to be ignored. Such a regime is realized in ultra-clean systems micro-fabricated in the nm-scale [3]. In this case, we should regard electrons as quantum "waves" rather than as "particles (balls)". The nonequilibrium regime described here is often referred to as the *ballistic regime*.

Based on similar arguments so far, we could find another universal behavior of electrons, assuming an extreme situation where (normal) electron-electron scattering is most dominant in the all scattering processes. Such a regime is closely related to the main theme of this thesis, namely *electron Hydrodynamics*, and the idea of scale separation is crucially important to understand it. In the above situation, a large scale separation occurs between the characteristic scales τ_{mc}, l_{mc} for momentum-conserving scattering (i.e., normal electron-electron scattering) and τ_{mr}, l_{mr} for momentum-dissipating scattering (i.e. any scattering other than normal electron-electron scattering), as well as characteristic scales L, T of external perturbations, leading to the following inequality:

$$\tau_{mc} \ll \tau_{mr}, T, \qquad l_{mc} \ll l_{mr}, L. \tag{1.1}$$

Under these conditions, first the electron system quickly forms a local equilibrium state

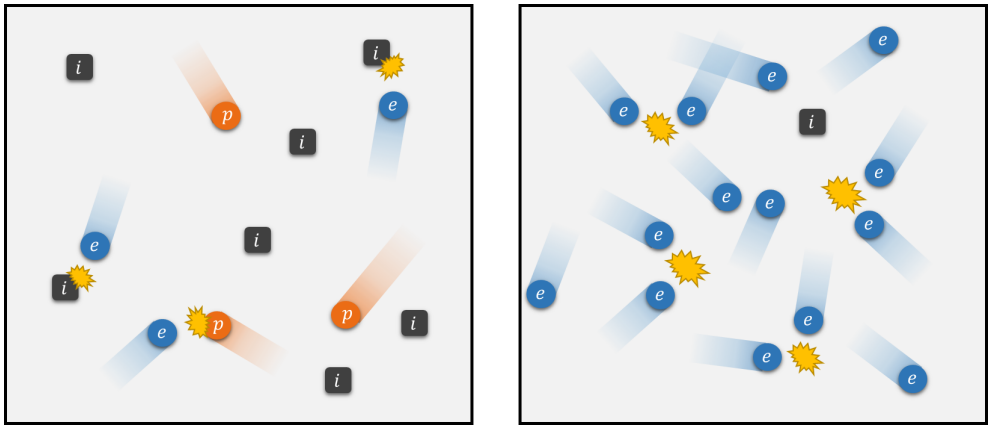

Figure 1.2: Difference of the intuitive pictures in electron transport. Blue and orange spheres denote electrons and phonons respectively, and gray boxes denote impurity scatterers. (Left) In conventional metals or semiconductors ($l_{mr} \ll l_{mc}$), we can understand an electron wave packet in a solid as a ball, and scatterers as a pinball. (Right) In the hydrodynamic regime ($l_{mr} \gg l_{mc}$), electron systems form a viscous fluids through strong electron-electron scattering processes, and show a peculiar collective dynamics. In this case, we can often regard the scatterers as obstacles damming the flow of water.

at each point in space through electron-electron scattering. Therefore, it is no longer important to track each electron's dynamics individually, and the macroscopic electron state at each spatial point can be described by several hydrodynamic variables, such as the density of conserved quantity, order paramters, and temperature. In particular, since momentum relaxation scattering occurs in a time scale sufficiently slower than momentum-conserving scattering, the total momentum and energy of electrons can be considered as an approximate conserved quantity, and thus should be treated as a part of the dynamical variables characterizing the local equilibrium state of the system. In this case, the electron system exhibits collective dynamics which behaves as a kind of viscous fluid, and whose time evolution is described by hydrodynamic equations such as the Navier-Stokes equation (see also Fig. 1.2). In the hydrodynamic picture, impurity scatterings occur in slower time scales, and then act as an obstruction to the flow of electron fluids. As a result, the electron dynamics in the hydrodynamic regime shows completely different dynamics from either the conventional Drude regime or the ballistic regime. In particular, it is well-known today that nonlocality due to viscosity and nonlinearity due to mode couplings give rise to a variety of unconventional transport phenomena unique to the hydrodynamic regime (For the details, see the following sections).

Some researchers maybe feel it strange at first glance that electronic systems in solids, which exhibit various exotic and "quantum" phenomena than usual fluids like water, can be described by such a classical description as hydrodynamics. However, looking back to the history of theoretical physics, we will notice that such an hydrodynamic approach is traditionally applied to various problems in the condesed matter physics. For example, it is well-known that the two-fluid model plays an essential role in understanding the superfluid phase of liquid helium. Such a phenomenological description in a macroscopic scale is still applied to various problems of superfluidity, and it is very useful for intuitive understanding of the phenomena of superconductivity and superfluidity. Furthermore, hydrodynamic theory also provides a very powerful analytical tool to describe extremely complex quantum systems with "strong interactions", such as the Quark-Gluon plasma. Various fascinating phenomena in these fluids, such as the chiral vortical effect [4] and

the chiral magnetic effect [5], can be understood from a hydrodynamic description, and it plays a very important role in explaining experimental results in heavy ion collisions [6]. Thus, strongly correlated quantum systems and fluid dynamics are not unrelated, but rather, fluid dynamics is widely used as an extreme theoretical method to intuitively and concisely understand complex strongly correlated quantum systems from a macroscopic viewpoint, which may be difficult to attack based microscopic descriptions.

Then, is it actually possible to realize materials that satisfy the hierarchical conditions for electron hydrodynamics (1.1)? One naively expects that, in priciple, if we can prepare a sufficiently clean metal (to avoid impurity scattering) and cools it to a sufficiently low temperature (to prevent phonon scattering), one could realize the hydrodynamic behavior of electron systems as described above. Nevetheless, in reality, hydrodynamic regime had never been realized for a long time, despite many experimental efforts. However, very recently, such a situation has completely changed. A lot of hydrodynamic signatures in electron trasnport have been reported since 2016 in various ultraclean metals such as graphene [7, 8, 9, 10, 11, 12, 13, 14], PdCoO2 [15], GaAs quantum wells [16, 17, 18, 19, 20, 21, 22], Weyl semimetal WP_2 [23], and WTe_2 [24, 25, 26]. Nowadays, electron hydrodynamics is rapidly growing up into a mature field of condensed matter physics.

In the following subsections, to give a overview, we briefly describe the details of the experimental backgrounds and recent developments in electron hydrodynamics. Based on this overview, I would like to conclude this chapter by mentioning in the last section what kind of problems remain to be solved in the study of electron hydrodynamics.

1.2 Experimental realization

Here we briefly discuss the historical background of electron hydrodynamics and essential difficulties in realizing the hydrodynamic regime in realistic materials. The following explanation is partially based on Ref. [27].

Gurzhi effect —— Electron hydrodynamics traces its origins to a paper submitted by the Soviet theoretical physicist Radii Gurzhi in 1963 [28]. He postulated an imaginary metal with a cylindrical shape that would satisfy the hierarchical conditions (1.1) (see also Fig. 1.3), and he predicted that, when an electric field is applied to the metal, the electrical resistance scales as

$$\rho \propto l_{ee} \propto T^{-2}, \tag{1.2}$$

where l_{ee} is the mean free path of the (normal) electron-electron scatterings and it is essentially equivalent to the paramter l_{mc} introduced in the previous subsection.

This phenomenon is in contrast to the standard understanding of metallic transport (electrical resistance increases with temperature due to the enhancement of phonon scatterings), and the result might seem to be very strange. However, this result can be intuitively understood by regarding the electron system as a viscous fluid: First, when a viscous fluid flows in a sample with a finite width, its resistance is proportional to the magnitude of the electric viscosity ν against the sample boundaries ($\rho \propto \nu$). On the other hand, viscosity itself is known to be proportional to the mean free path of electron-electron scattering l_{ee} from microscopic arguments. Since l_{ee} scales with temperature as $1/T^2$ from the basic Fermi liquid theory, we can conclude that the resistivity behaves as shown in Eq. (1.2). Nowadays, this phenomenon is known as the *Gurzhi effect* and several recent experiments have reported the observations [10, 18, 20, 29]. More generally, in realistic materials, we can observe the crossover from the ballistic regime to the hydrodynamic regime and then to the Ohmic regime. This was also discussed by R. Gurzhi and the main points are summarized in the caption of Fig. 1.3.

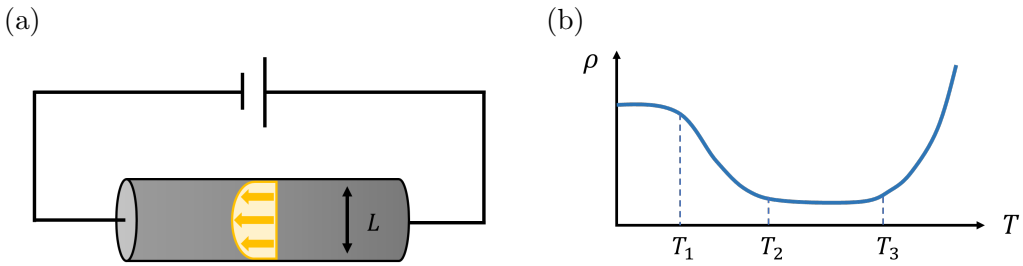

Figure 1.3: (a) Experimental setup for the Gurzhi effect [28]. (b) R. Gurzhi discussed the temperature dependence of electric resistivity $\rho(T)$ in the crossover from the ballistic regime to the hydrodynamic regime and then to Ohmic regime [28]. Each characteristic temperature T_1, T_2, T_3 is defined to satisfy $l_{ee}(T_1) \sim L$, $l_{mr}(T_2) \sim L^2/l_{ee}(T_2)$, and $l_p(T_3) \sim l_{imp}$ respectively. Here l_p and l_{imp} are the mean free paths of electron-phonon scatterings and impurity scatterings respectively. In the temperature range of $T \leq T_1$, since l_{ee} surpass the sample size L, the effective mean free path for the resistivity, l_{eff}, is completely determined by the sample size L: $l_{\text{eff}} \propto L$. As a result, the resistivity does not depend on the temperature. In the temperature range of $T_1 \leq T \leq T_2$, the electron system satisfies the hydrodynamic conditions (1.1) and it behaves obeying electron hydrodynamics. Consequently, the effective mean free path l_{eff} is proprtional to the inverse of the electron viscosity, which is usually proportional to the electron-electron mean free path l_{ee}. Since l_{ee} scales as $1/T^2$ in Fermi liquids, the resistivity decreases as temperature increases. This is the origin of so-called the Gurzhi effect. In the temperature range of $T_2 \leq T \leq T_3$, the electron viscosity becomes too small and the impurity scattering dominates as the orgin of the electric resistance. In the temperature range of $T \geq T_3$, the rate of electron-phonon scatterings surpasses that of impurity scatterings, leading to positive differential resistivity.

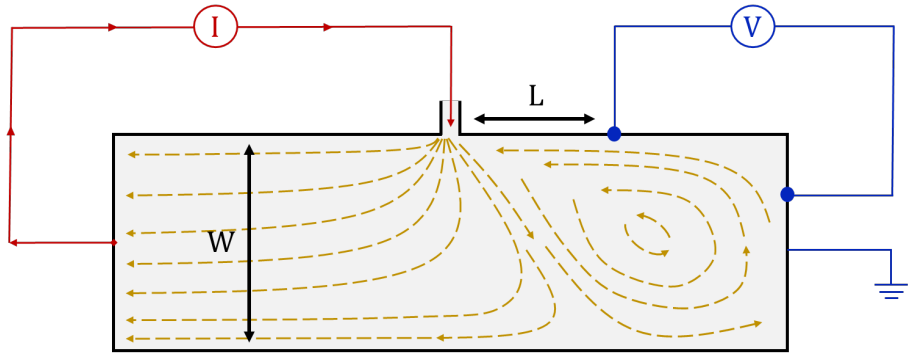

Figure 1.4: The schematic of the vicinity geometry for nonlocal resistance measurements in Ref. [7]. Yellow dashed line represents the flow lines of electric currents. In the hydrodynamic regime, the system exhibits a eddy current pattern (or viscous backflow) near the current injector because of nonlocal forces due to the electron viscosity, leading to sign changes of nonlocal resistances from those in the Ohmic regime.

Difficulties in realizing the hydrodynamic regime —— Unfortunately, after decades of experimental efforts, it had become gradually clear that, in reality, it was not feasible to realize a sample that satisfies the requirements of electron hydrodynamics with the experimental techniques of the time. The reasons are as follows: First, in order to keep the impurity scattering length l_{imp} sufficiently small, it is required to prepare extremely clean metallic samples. On the other hand, to increase the electron-phonon scattering length l_p, the system must be cooled sufficiently to strongly suppress the thermal excitation of phonons. However, according to the Fermi liquid theory, the electron-electron scattering length l_{ee} ($= l_{mc}$) also increases with cooling according to the scaling $1/T^2$. Therefore, the hydrodynamic regime is actually realized only in a very limited temperature range satisfying $l_{ee}(T) \ll l_{imp}, l_p(T)$. Especially for usual three-dimensional metals, the above restrictions are quite severe because l_p scales as T^{-3} and decays much faster than l_{ee} as the temperature increases [1].

Promising candidate —— One turning point to overcome these difficulties was the appearance of graphene technology. At the time of the Nobel Prize for it, the impurity scattering length of graphene barely exceeded 100 nm, and it was far from the realization of the hydrodynamic regime. However, encapsulation techniques with hexagonal boron nitride (hBN) made it possible to achieve an unprecedented level of high mobility, and the hydrodynamic regime became increasingly likely to realize.

In particular, in contrast to 3D metals, the electron-phonon scattering length in 2D materials shows a slow decrease accompaning with increasing temperature, which scale as l_p/T^{-1}. Especially in graphene, due to the stiffness of its lattice, it has a large amplitude of the scaling coefficient. This temperature dependence is sufficiently slower than that for $l_{ee} \propto T^{-2}$, so that it is possible to satisfy $l_{ee} \ll l_p$ above a certain temperature T^*.

Realization of the hydrodynamic regime and negative nonlocal resistance —— Eventually, in 2016, the hydrodynamic behavior in graphene was experimentally reported in Ref. [7, 30] (At the same time, hydrodynamic behavior in $PdCoO_2$ was also

[1] In practice, it is also important to consider another momentum relaxation process due to the Umkrapp scattering. The Umkrapp scattering is strongly dependent on the shape of the Fermi surface, and it is completely forbidden in the limit where the Fermi surface is sufficiently small. Therefore, in systems with sufficiently small Fermi surfaces such as graphene, Dirac/Weyl semimetals, and semiconductors, the contribution of such momentum relaxation is considered negligible, and in fact most of materials that realize the hydrodynamic regime belong to these classes of materials.

reported) In Ref. [7], the authors have observed negative nonlocal resistance due to viscosity in graphene samples with a special geometry called "vicinity geometry". First, they injected an electric current I into the graphene sample with width W under the geometry shown in Fig. 1.4, and they measured the electric potential at two different points at various temperatures and carrier densities to estimate the nonlocal resistance. According to the theoretical calculations [31], systems in the Ohmic regime exhibit simple local electrical transport in accordance with the Ohm's law, resulting in a positive nonlocal resistance as naively expected. In contrast, in the hydrodynamic regime, unconventional nonlocal transport is realized due to the electron viscosity, leading to the breakdown of the Ohm's law or negative nonlocal resistance. Such a current distribution is realized because of the large gradient of velocity fields around the contact into which the current flows. The big stream of electrons from the contact drags electron fluid around the contact with viscous forces, creating an unconventional electron flow that goes against the potential gradient. This eventually generates an eddy current distribution, leading to a negative nonlocal resistance. In actual experiments, the crossover between the Ohmic regime and the hydrodynamic regime is also observed as the temperature of the system changes.

Electric Poiseuille flow —— As just described above, in order to observe viscous fluid-like behavior of electron systems, it may be a good strategy to prepare ultraclean samples microfabricated in the μm-scale, and let the current profile due to the viscosity manifest in the electron transport under some specific geometry. In fact, a similar strategy has been employed in many other papers to detect hydrodynamic signatures in electron flows [9, 11, 18, 19, 20, 32, 33, 34, 35, 36, 37]. For example, in experiments using the delafossite metals $PdCoO_2$ [15] and the Weyl semimetal WP_2 [23], they prepared an elongated channel with a finite width W as shown in Fig. 1.3 (a) and observed the so-called Poiseuille flow. In particular, the experimental results for WP_2 are shown in Fig. 1.3. When a sufficiently large momentum relaxation free path $l_{mr}(\gg l_{mc}, W)$ realizes in a metall sample with such an elongated structure, the electric resistance of the system is no longer determined by scattering by impurities, but by the viscous force generated near the boundary. In this case, the electron fluid will exhibit a nearly parabolic profile of electric current, which is well-known as the Poiseuille flow, and the electrical resistance will show a scaling as follows (see also the appendix for this chapter):

$$\rho \propto \eta,\ W^{-2}. \tag{1.3}$$

Here η is the sheer viscosity of electron fluids. In both experiments in $PdCoO_2$ and WP_2, width-dependence like Eq. (1.3) is indeed observed in a certain temperature regime (Figure 1.4 (d)), and therefore, we believe that the hydrodynamic regime is realized in these materials in the certain window of temperature (Fig. 1.4 (f)). In addition, Refs. [15, 23] have reported a remarkable negative magnetoresistane in each system (Figure 1.4 (e)). Actually, this phenomena can be understood from the fact that the magnetic field dependence of the shear viscosity $\eta(B)$, which determines the electric resistance, is obtained in the following form [38]:

$$\eta(B) \propto \frac{\eta(0)}{1+(2\tau_{mc}\omega_c)^2} \qquad (\omega_c \equiv eB/m). \tag{1.4}$$

In this way, just by investigating the Poiseuille flow, various unconventional phenomena due to viscosity can be found in hydrodynamic systems, and thus transport experiments in some special geometries, such as Fig. 1.3 (a) and Fig. 1.4, will be a good touchstone for detecting the hydrodynamic regime.

1.3 Recent developments

Here we briefly summarize recent theoretical and experimental developments in the context of electron hydrodynamics. They provide us with various experimental probes for the hydrodynamic flow, as well as novel hydrodynamic phenomena which might characterize electron fluids in solids.

Breaking of the Wiedemann-Franz law —— Breaking of the Wiedemann-Franz law — a universal relation between electric conductivity σ and thermal conductivity κ in typical Fermi liquid systems — has been reported in several semi-metallic materials such as graphene [8, 30, 39, 40], bulk antimony [41], MoP [42], $ZrTe_5$ [43] and WP_2 [44], as indirect evidence for the realization of electron hydrodynamics. Similar discussion can also be found in the studies of magnon fluids [45]. For example, in Ref. [30], the authors have suggested that this violation can be attributed to non-Fermi liquid nature of the Dirac fluid originating from frequent electron-hole scatterings, which leads to an emergent friction between electron and hole flows. Under a temperature bias, both of these carriers flow in the same direction, and thus the friction between them never causes an additional thermal resistance. On the other hand, under an electric field, these carriers flow in the opposite directions, and thus additional electric resistance arises due to the friction between the opposite flows. This leads to the strong enhancement of the Wiedemann-Franz ratio $L = \kappa/\sigma T$, compared to the standard value in Fermi liquids.

However, very recent work [46] has performed a further quantitative analysis using the Boltzmann transport theory which is based on the Fermi liquid considerations, and they have concluded that experimental results in Ref [30] may not actually have anything to do with Dirac fluid hydrodynamics, but relates to finite-temperature low-density bipolar diffusive transport by electrons and holes in the presence of short- and long-range disorder, and phonons. In this way, it is still controversial whether the breaking of Wiedemann-Franz law is related with the appearance of the hydrodynamic behavior, and thus further discussions are needed for this problem.

Visualization of electron flow —— Modern developments of magnetic sensors with diamond nitrogen-vacancy (NV) centers, enable us even to visualize the nonuniform hydrodynamic flow directly with high spatial resolution [24, 33, 47, 48]. In these experiments, the authors have performed scanning measurement of the spatial profile of magnetic fields that originates from the local electric current. Then, by performing a proper transformation, they have reconstructed the original profile of electric current from the obtained data. As a result, it has been verified well that there are clear differences between current profile in the Ohmic and the hydrodynamic regime. Similar experiments for imaging hydrodynamic flow has also been reported with another type of scanning techniques based on single-electron transistor (SET) [49, 50], scanning gate microscopy (SGM) [21], or superconducting quantum interference device (SQUID) [51]. On the other hand, in Ref. [25], the authors have performed a measurement using polarization-sensitive laser microscopy, and they have demonstrated the emergence of anomalous sign-alternating patterns in charge density in multilayer WTe_2 at room temperature, which is visually similar to that predicted from electron hydrodynamics. However, they have also indicated that this material does not exhibit true electronic hydrodynamics, but pseudo-hydrodynamic behavior due to a subtle interplay between the diffusive transport of electrons and holes. These observations imply that we might need to have more careful discussion when we try to detect the hydrodynamic regime via these scanning techniques.

Nonlinear hydrodynamic flow —— Nonlinearity in electron flows, which may lead to turbulant or unsteady current dynamics, is also a fascinating aspect of the hy-

drodynamic regime. As is well known in conventional hydrodynamic theory, the relative important of nonlinearity is evaluated well by the so-called *Reynolds number* $\mathcal{R}$, which is defined as the ratio of inertial forces to viscous forces:

$$\frac{(\text{inertial force})}{(\text{viscous force})} \sim \frac{|(\boldsymbol{u}\cdot\boldsymbol{\nabla})\boldsymbol{u}|}{|\nu\Delta\boldsymbol{u}|} \sim \frac{LV}{\nu} \equiv \mathcal{R}, \tag{1.5}$$

where L and V are characteristic scales of length and velocity in the flow at hand, and ν is kinematic viscosity. Generally, at low Reynolds numbers ($\mathcal{R} \ll 1$), viscous forces dominate the fluid dynamics and the flows tend to be smooth, stable, sheet-like, and constant (or periodic) in time. Such a flow is often refered to as *laminar flow*. On the other hand, at high Reynolds numbers ($\mathcal{R} \gg 1$), inertial forces (nolinearity) dominate the fluid dynamics, and the flows tend to be unstable and produce many chaotic eddies, which are the so-called *turbulances*. Although there is no clear difinition of them, well-developed turbulences are known to be characterized by chaotic behavior, high diffusivity, energy cascades from small-scales to large-scales, universal power law of energy spectrum. For typical examples, steady laminar flow becomes unstable around $\mathcal{R} \sim 10$ - 100 and exhibits the preturbulent flow such as the so-called vortex shedding. Then, at $\mathcal{R} > 10^3$ - 10^4, hydrodynamic flows reach the turbulent regime.

In electron hydrodynamics, whether turbulence can occur in realistic experimental setups is an important issue of great interest. For example, by using the typical parameters in Ref. [7], we can estimate the Reynolds number as $\mathcal{R} \sim 10^{-3}$ ($\ll 1$). Here we have assumed that $I \sim 0.1$ μA, $n = 10^{12}$ cm^{-2}, $L = 1$ μm, and $\nu = 10^3$ cm^2/s, where I is an apllied electric current and n is the carrier density of graphene[2]. Clearly, this value is too small to realize a turbulent electron flow, and thus we need further ingenuity to realize the turbulent electron flow in actual experiments.

One possible strategy to improve the Reynolds number is seeking for novel hydrodynamic materials with a sufficiently small kinematic viscosity since the Reynolds number becomes large as kinematic viscosity decreases. For example, Ref. [52] has analyzed the shear viscosity of graphene at the charge neutral point (CNP), and shown that the ratio η/s of shear viscosity η to the entropy density s comes close to a lower bound conjectured by the AdS-CFT correspondence [53]:

$$\frac{\eta}{s} \leq \frac{1}{4\pi}\frac{\hbar}{k_B}, \tag{1.6}$$

where s is the entropy density. This bound is called the Kovtun-Son-Starinets (KSS) bound, after the name of the authors of Ref. [53]. Especially for graphene near the CNP, the Reynolds number should be modified as

$$\mathcal{R} = \frac{LV}{\nu_{\text{eff}}}, \quad \nu_{\text{eff}} = \frac{c^2\eta}{Ts}, \tag{1.7}$$

due to the relativistic nature, and these values are estimated as $\mathcal{R} \sim 100$ and $\nu_{\text{eff}} \sim 5\times10^{-3}$ m^2/s respectively, assuming that $\eta/s \sim 0.2\hbar/k_B$, $T = 300$ K, $u \sim 10^5$ m/s, and $L = 5$ μm [54]. More recent work [55] has performed ab-initio calculations for scandium Herbertsmithite $ScCu_3(OH)_6Cl_2$, which is a two-dimensional Dirac semimetal with a small Fermi velocity. As a result, it has been suggested that this material has sufficiently suppressed electron-phonon coupling below 80 K and much smaller viscosity than that of graphene at the CNP, which corresponds to the Reynolds number 63 - 156 times larger than graphene. In this way, these fine-tuned materials might enable us to realize turbulent electron flows experimentally in the near future.

[2]This setup corresponds to the amplitude of velocity fields aroud $u \sim 10^2$ m/s.

Detailed theoretical analyses for preturbulent flow have already been obtained, assuming realistic experimental setups, in several works [54, 56]. For example, inspired by these results, Ref. [54] has performed numerical simulations of relativistic hydrodynamic equations for Dirac fluids around a micron-sized constriction geometry, which is implementable with modern experimental techniques. They have numerically cofirmed that constriction geometry leads Dirac fluids to the preturbulent regime at Reynolds number as small as $\mathcal{R} \sim 25$. Such a preturbulent electron flow might be detectable through weak current fluctuation with a broad spectrum in the range of several hundred MHz. Further detailed analyses have been provided in Ref. [56]. They have assumed that applied elctric currents are within the range between 10^{-3} mA and 1 mA, and account for electrostatic interactions and momentum-relaxing processes. As a consequence, they have concluded that preturbulence is predicted to occur at experimentally attainable values of the Reynolds number between 10 and 50, leading to time-series fluctuation of electrochemical potential over a broad spectrum of frequencies between 10 and 100 GHz.

Moreover, dynamical instability of electron fluids is also an interesting phenomenon in electron hydrodynamics. M. Dyakonov and M. Shur have revealed in their seminal work [57] that, above a certain threshold of applied vias, electron flows become unstable in plasmonic cavity with an specific boundary conditions (often refered to as Dyakonov-Shur boundary conditions) and show a spontaneous current oscillation without dynamical perturbations. This instability orginates from the plasma wave amplification due to the reflection from the device boundaries, and thus, long lifetime of plasmons is essential for the realization. Nowadays, this phenomenon is known as the *Dyakonov-Shur instability*, and regarded as a promising mechanism of the generation of coherent THz radiations. More detailed numerical simulations have also been performed beyond the linear response theory in several recent works [58, 59, 60, 61]. Furthermore, Ref. [62] has generalized the concept of hydrodynamic instabilities driven by a direct current into Dirac and Weyl semimetals. This paper has clarified that, these materials exhibit a new type of instability dubbed entropy wave instability, in addition to the conventional Dyakonov–Shur instability for plasmons. On the other hand, Ref. [63] has developed a magnetohydrodynamic theory for Weyl semimetals and discussed their Dynamo instability, which is a well-known astrophysical phenomenon and believed to be responsible for generating and sustaining magnetic fields in galaxies, stars, and planets, including the Sun and Earth [64, 65, 66]. The authors have formulated a magnetohydrodynamic theory for Weyl electron-hole plasma, taking chiral anomaly terms into account, and discussed the scaling of (magnetic) Renolds number for Weyl fluids. As a result, they has suggested that chiral anomaly term plays an important role to reduce the threshold magnetic Reynolds number for the dynamo instability, and Weyl semimetals might serve as a novel platform to observe the dynamo effect due to the relatively large Reynolds number.

In addition, Ref. [67] has discussed how to observe nonlinear electron flows in acutual experiments, as a alternative approach to nonlocal transport measurements for detecting the hydrodynamic regime. Based on the conventional Navier-Stokes equation, they have proposed how to realize some of nonlinear phenomena well-known in classical fluids, including the electronic Bernoulli effect, Eckart streaming, and Rayleigh streaming. Then, they have concluded that these phenomena are within reach of graphene-based devices with realistic paramter values.

1.4 Questions and our goals

At the end of this chapter, we would like to mention open questions in the context of electron hydrodynamics, and show our goals in this thesis. For more detailed techniques

used in this work, we give an overview in the following several sections.

First, as already mentioned, most of previous studies on electron hydrodynamics, except for recent challenging works, usually assume that electron fluids have unrealistic high symmetries such as spatial isotropy and the Galilean symmetry, and they have not taken into account the effects of crystal symmetries. At the same time, this also leads to ignoring the geometrical effects of the Bloch wavefunction, which is described by such terms as the Berry curvature and the anomalous velocity, in the transport response. As a result, these studies might have overlooked so far a lot of facinating phenomena peculiar to electron fluids in solids. More notable is that some of recent experiments have reported the realization of the hydrodynamic regime in *noncentrosymmetric* materials, such as MoP [42], WP_2 [23], WTe_2 [24, 25, 26], bilayer-graphene [7, 68, 69, 70], and GaAs quantum wells [16, 17, 19, 20, 21]. In these materials, we know that the inversion symmetry breaking and the resulting quantum geometrical effects play an important role to understand their anomalous transport or optical phenomena.

Second, it is well-known that electron hydrodynamics provides us with a powerful tool to analyze collective modes and nonlocal responses of electron systems in an intuitive manner, since it provides us with a macroscopic description of slow variables' dynamics. For these reasons, hydrodynamic approach itself has long been used to describe the plasmon dynamics in the context of plasmonics. Our question is whether we can develop a new type of plasmonic devices that utilize quantum geometrical effects in the noncentrosymmetric hydrodynamic systems discussed above.

Based on these backgrounds and motivations, we have conducted the following research:

Formulation of an anomalous hydrodynamic theory in nocentrosymmetric systems (Chapter 3) —— Focusing on the crystal symmetry (especially inversion symmetry) and the geometrical properties of the Bloch electrons, we have investigated what roles these factors play in hydrodynamic transport in noncentrosymmetric materials. For this purpose, we have formulated an anomalous hydrodynamic theory for noncentrosymmetric electron fluids, and we have proposed unconventional hydrodynamic transport phenemena that will be detectable by state-of-the-art experimental techniques.

Analysis of plasmonically-driven geometical photocurrent in plasmonic devices (Chapter 4) —— We have investigated an interplay between quantum geometrical effects and surface plasmons through surface plasmonic structures, based on an anomalous hydrodynamic theory we proposed. First we have discussed how resonant excitation of surface plasmons and near-field effects influence photogalvanic effects due to the quantum geometrical effects. Next we have clarified a universal relation between the optical absorption and the amplitude of photocurrent induced by the Berry curvature dipole. This work might provide us with a promising route toward a novel type of highly sensitive, broadband terahertz photodetectors.

1.5 Appendix for this chapter

Here we briefly show how to obtain the scaling in Eq. (1.3). In the hydrodynamic regime, we assume that electron dynamics can be described by the usual hydrodynamic theory, i.e. the Navier-Stokes equation:

$$\frac{\partial \boldsymbol{u}}{\partial t} + (\boldsymbol{u}\cdot\boldsymbol{\nabla})\boldsymbol{u} + \frac{\boldsymbol{\nabla} P}{\rho} - \nu\boldsymbol{\Delta}\boldsymbol{u} + \frac{e}{m}\boldsymbol{E} = -\frac{\boldsymbol{u}}{\tau_{\mathrm{mr}}}, \tag{1.8}$$

where $\nu = \eta/\rho$ is the kinetic viscosity, ρ is the particle density, P is the pressure, m is the mass of electric carriers. Here we have introduced the friction term $-\boldsymbol{u}/\tau_{\rm mr}$ due to the momentum-relaxing scattering processes. Assuming the setup for the Poiseuille flow, where the systems has finite width W in the x-direction and an electric field is applied in y-direction, the above equation is simplified for $\boldsymbol{u} = (0, u_y(x), 0)$ as follows:

$$\frac{\partial u_y}{\partial t} - \nu \frac{\partial^2 u_y}{\partial x^2} + \frac{e}{m} E = -\frac{\boldsymbol{u}}{\tau_{\rm mr}}. \tag{1.9}$$

This equation can be solved easily, and we obtain the following solution for the velocity field:

$$u_y(x) = \frac{e\tau_{mr} E}{m} \left[1 - \frac{\cosh(x/l)}{\cosh(W/2l)} \right], \tag{1.10}$$

where $-W/2 \leq x \leq W/2$ and $l \equiv \sqrt{\nu \tau_{\rm mr}}$. The total electric current is calculated by integrating the current density $j_y(x) = -enu_y(x)$ over the channel width. Finally, we obtain the following form of electric resistivity:

$$\rho = \frac{m}{e^2 n \tau_{\rm mr}} \frac{1}{1 - \tanh(W/2l)/(W/2l)} \tag{1.11}$$

Compared to the Drude resistivity $\frac{m}{en\tau_{\rm mr}}$, this result can be interpreted as the mean free time $\tau_{\rm mr}$ is replaced by the effective mean free time

$$\tau_{\rm eff} = \tau_{\rm mr} \left(1 - \frac{\tanh(W/2l)}{(W/2l)} \right) \tag{1.12}$$

Especially in the case of $w \ll l$, the effective mean free time reduces to the form

$$\tau_{\rm eff} = \frac{W^2}{12\nu} + \mathcal{O}\big((W/l)^5\big), \tag{1.13}$$

which corresponds to the desired scaling rule shown in Eq. (1.3).

Chapter 2

Nonlocality and Plasmonics

In this chapter, to provide background knowledge about our studies in Chap. 3 and Chap. 4, we briefly discuss the importance of nonlocality in electric responses and previous applications of electron hydrodynamics in plasmonics. Moreover, since terahertz applications are one of the main concerns of our research as well as plasmonics, we also give a brief overview of this area.

2.1 Nonlocality in responses

In this section, we discuss the importance of nonlocality in electromagnetic responses of solids. First, we introduce the concept of "local" response and implicit assumptions to make it valid. Next we clarify the cases where the assumptions are broken, which include the plasmonic systems and ultra-clean metals in the hydrodynamic regime. Then, relating them with some symmetry considerations, we explain that nolocality in responses provoke various fascinating phenomena such as nonreciprocal directional dichroism and plasmonic resonances.

Local responses —— When discussing electromagnetic responses of matters, we often assume that the responses of the systems $A(\boldsymbol{r}, t)$, such as electric current and electric polarization, are determined only by the value of the electromagnetic perurbation $B(\boldsymbol{r}, t)$ at the same point $\boldsymbol{r}$, though taking the delay in time into account. This assumption can be expressed formally in the following form:

$$A(\boldsymbol{r}, t) = \int d\tau \chi(t - \tau) B(\boldsymbol{r}, \tau). \tag{2.1}$$

By performing a Fourier transformation, this formula can be rewritten in another familiar form,

$$A(\boldsymbol{r}, \omega) = \chi(\omega) B(\boldsymbol{r}, \omega). \tag{2.2}$$

For example, the Drude theory, which is one of the most simpified models of electric conduction, leads to the famous relation between electric currents j and optical electric fields $\boldsymbol{E}$, i.e., the so-called Drude formula,

$$j(\boldsymbol{r}, \omega) = \sigma(\omega) E(\boldsymbol{r}, \omega), \quad \sigma(\omega) = \frac{\sigma_0}{1 - i\omega\tau} \tag{2.3}$$

where τ is the momentum-relaxing time, n is the carrier density, and $\sigma_0 = ne^2\tau/m$. Especially in the limit of $\omega \to 0$, this leads to the familiar (local) Ohm's law: $j(\boldsymbol{r}) = \sigma_0 E(\boldsymbol{r})$. In usual dirty or hot metals, such a naive assumption is guaranteed by large separation of length scales between the wavelength of incident lights and characteristic

length in the microscopic level, which typically corresponds to the mean free path of impurity scatterings or electron-phonon scatterings.

Nonlocal responses —— However, the above assumption is sometimes broken when we consider some physical systems that have a characteristic length scale comparable to the scale of its microstructure or the wavelength of incident lights. For example, we encounter these situations when treating such objects as ultra-clean metals [27], polaritons [71], photonic crystals or metamaterials [72, 73, 74, 75, 76, 77], and other nanostructured devices [78, 79]. In particular, polaritons have a finite momentum, and thus we have to achieve a momentum matching between the polaritons and the incident free lights to resonantly excite these collective modes. In addition, polaritons have an interesting property to trap and confine incident lights into a small space, leading to a strong enhancement of nonlocal effects [71, 80]. For these reasons, to discuss the interplay between polaritons and optical responses, nonlocality can never be ignored, but rather plays a central role in understanding the polariton physics.

Nonlocality in electron hydrodynamics —— Nonlocality in responses is also one of important aspects of electron hydrodynamics, where viscous effects and boundary frictions become nonnegligible to undestand the transport and optical properties of electron systems. As already mentioned, in the hydrodynamic regime, the (local) Ohm's low is broken down and the nonlocality due to electron viscosity dominates electric transport in microfabricated devices, leading to strange eddy flows and negative nonlocal resistance. These unique behaviors are essentially attributed to the scale separation, $l_{mc} \ll L \ll l_{mr}$, which realizes in the hydrodynamic regime. Here, L is the characteristic length scale of the responses at hand. Since hydrodynamic formalism provides a clear description of collective motion of electrons under non-uniform perturbations, it has ever been applied to describe electronic collective modes [81, 82, 83, 84, 85, 86, 87, 88, 89] and nonlocality of optical responses [79, 90, 91, 92, 93, 94, 95, 96, 97, 98, 99, 100, 101, 102, 103, 104, 105], as well as nonlocal transport phenomena with non-uniform current profiles in structured channels [38, 95, 106, 107, 108, 109, 110, 111, 112, 113, 114] and the resulting electron preturbulence [54, 56].

Onsager reciprocal theorem —— From the symmetry viewpoint, we find that nonlocality is also an important source of nonreciprocity in responses. According to the Onsager reciprocal relations [115, 116], electric conductivity σ_{ij} must satisfy the following constraint:

$$\sigma_{ij}(\boldsymbol{q}, \omega, \boldsymbol{B}) = \sigma_{ji}(-\boldsymbol{q}, \omega, -\boldsymbol{B}), \tag{2.4}$$

where $\boldsymbol{q}$ and ω are the wavevector and the frequency of the external electric fields, and $\boldsymbol{B}$ is an applied magnetic field or other perturbations that break the time-reversal symmetry. As can be easily understood from this equation, nonlocality (finite wavevector) and magnetic fields play essentially similar roles in the constraint of conductivity tensor. For example, applying external magnetic field yields a finite anti-symmetric component of electric conductivity, which leads to the Hall current in transport experiments, or the Kerr and Faraday effect in optical experiments. On the other hand, the finite wavevector of an incident light also yields a component with the same commutativity, which causes natural optical activity, i.e., a rotation of the polarization plane (natural optical gyrotropy) and differential absorption between different helicities (natural circular dichroism).

Directional dichroism —— Although the latter case (i.e., natural optical activity) is quite similar to the former case (i.e., Kerr and Faraday effect), there is a crucial difference between them. For a demonstration, let us assume that the magnetic field is sufficiently small and the external perturbation varies much more smoothly than the microscopic length scale that the system has. Then we can expand the conductivity tensor up to the

first order in B and k as follows:

$$\sigma_{ij}(\boldsymbol{q},\omega,\boldsymbol{B}) \simeq \sigma_{ij}(\omega) + q_k \frac{\partial \sigma_{ij}}{\partial q_k}(\omega) + B_k \frac{\partial \sigma_{ij}}{\partial B_k}(\omega) + q_k B_l \frac{\partial \sigma_{ij}}{\partial q_k \partial B_l}(\omega) + \cdots . \tag{2.5}$$

Here we note that each component satisfies the following relation in accordance with the Onsager's reciprocal theorem:

$$\sigma_{ij} = \sigma_{ji}, \quad \frac{\partial \sigma_{ij}}{\partial q_k} = -\frac{\partial \sigma_{ji}}{\partial q_k}, \quad \frac{\partial \sigma_{ij}}{\partial B_k} = -\frac{\partial \sigma_{ji}}{\partial B_k}, \quad \frac{\partial \sigma_{ij}}{\partial q_k \partial B_l} = \frac{\partial \sigma_{ji}}{\partial q_k \partial B_l}, \tag{2.6}$$

which means that $\frac{\partial \sigma_{ij}}{\partial q_k}$ and $\frac{\partial \sigma_{ij}}{\partial B_k}$ are anti-symmetric in comutation of (i,j), and the others are symmetric. Especially in optical responses, the second and third terms in the right side correspond to the natural optical activity and the Kerr (or Faraday) effect respectively. Since the wavevector q changes the sign when the direction of light is reversed, we notice that these terms have different dependences on the direction of light. Such light direction-dependent optical response is often referred to as directional dichroism or directional birefringence. From the same arguments, we find that the last term in Eq. (2.5) describes various directional dichroic responses. For example, nonreciprocal phenomena related to this term include the so-called magnetochiral effect [115, 117, 118], nonreciprocal magnon [119, 120, 121, 122], and noreciprocal plasmon with and without magnetic fields [123, 124, 125, 126]. Interestingly, especially in bulk crystals, these nonreciprocal phenomena are often related with geometrical structures of Bloch electrons in the Brillouin zone [124, 126, 127, 128, 129, 130, 131, 132, 133, 134, 135], which provide us with a deep insight to the band structure of crystals through optical responses.

Relation with inversion symmetry —— Since electric currents, electric fields, and wavevectors are all odd under inversion symmetry, $\frac{\partial \sigma_{ij}}{\partial q_k}$ and $\frac{\partial \sigma_{ij}}{\partial q_k \partial B_l}$ always vahish in centrosymmetric materials, except for the responses on the surface. This is the reason why we usually consider chiral or other noncentrosymmetric materials when discussing nonreciprocal phenomena. In a similar sense, nonlocality also plays an important role in optical rectification or, more generally, second order optical responses. This is because the output quantities such as electric currents are odd under inversion symmetry while the second order term of electric field always even under inversion symmetry. Therefore, in centrosymmetric materials, surface contributions and intrinsic nonlocal contributions become dominant sources of the second order optical responses, and the latter is also often closely related to the quantum geometrical effects [136].

In this way, nonlocality often plays an important role in understanding some classes of optical phenomena in both of centrosymmetric and noncentrosymmetric materials. In Chap. 3, focusing on the hydrodynamic regime, we will discuss anomalous nonlocal transport phenomena due to inversion symmetry breaking.

2.2 Introduction to plasmonics

Plamonics is an active research area that explores the interaction between free lights and surface plasmons on structured metallic surfaces to achieve highly efficient generation, detection, and manipulation of lights [137, 138, 139]. It enables us to break the diffraction limit of free lights and acquire strong field enhancements by utilizing a peculiar property of plasmons to confine the light locally. These features are fascinating to realize nanophotonic devices such as waveguide circuit [140, 141, 142], highly-sensitive photodetectors [143, 144], and sollar cells [145, 146, 147]. Furthermore, surface plasmons inherent in two-dimensional (2D) layered systems, such as graphene, have remarkably long lifetimes and electrically-tunable dispersions in the terahertz or mid-infrared region [71, 148, 149]. These properties

are particularly ideal for developing novel tunable terahertz to mid-infrared plasmonic devices [139, 143, 150, 151].

In what follows, we give a brief overview of plasmonics, mentioning to its relation with electron hydrodynamics. First we introduce the concept of the mid-infrared and terahertz technology, which is one of the main concerns in plasmonics, and explain its practical importance and its major challenges. Next, we explain several promising applications of plasmonics and how to excite and control surface plasmons. Finally, taking plasmonic ratchet effect and Dyakonov-Shur theory as examples, we demonstrate how powerful electron hydrodynamics is in describing various plasmonic phenomena.

2.2.1 Terahertz technology

The terahertz regime is widely considered as a next frontier between electronics and optics, and it promises a lot of cutting-edge applications, including imaging, wireless communications, ultrafast computing, quality control of food and agricultural products, homeland security, molecular exploration, and biomedical sensing [152]. In a nutshell, the potential for these applications would be attributed to the following characteristics of terahertz waves:

1. High permitivity through many materials
2. Operation in a non-destructive manner
3. Resonant coupling to various collective modes in solids or molecules
4. Spatiotemporal resolution higher than microwaves

In particular, collective modes resonant to terahertz waves, such as surface plasmons, are crucially important to understand the mechanism of various THz techniques, since they not only act as a trigger for imaging and driving of materials [153, 154], but also enhance or expand the functionality of terahertz technologies as in plasmonics [71, 139, 155].

According to the review article, Ref. [156], the central problems that might hinder future developments of terahertz technology can be summarised as follows; (1) the lack of intense THz sources and sensitive THz detector, (2) the lack of commercial optical components and instrumentations that operate in the terahertz regime, (3) strong water vapour absorption that prohibits sensing and imaging of water-rich targets, as well as limiting the range of THz wave propagation for remote applications. In what follows, we give more detailed explanation of these dificulties, and introduce several possible applications of THz technology in bio-chemistry, condensed matter physics, and wireless communications.

Terminology and terahertz gap —— Although there exist some diffrent definitions, the terminology "terahertz (THz) regime" usually denotes the frequency region between the infrared and microwaves, typically referred to as the frequencies from 300 GHz to 3 THz (or 30 THz). Electromagnetic waves in this regime have photon energies smaller than the band-gap energy of typical narrow-gap semiconductors[1], but larger than the energy scales corresponding to clock frequencies of typical central processing units (CPUs), which are around several GHz. Consequently, our conventional techniques to contol electromagnetic waves, that is, *electronics* and *optics*, are typically inaccessible to the terahertz regime. Nowadays, this issue is referred to as the *terahertz* "*gap*", and the word "gap" means that our THz technology is still in infancy to achieve mass production

[1]For example, the band-gap energies of narrow-gap semiconductors InAs and SnTe are around 350 meV and 180 meV. These are comparable to the photon energy in the mid-infrared regime.

of THz devices and its operation at room temperature [150, 152] (As for the current status of THz technology, for example, please refer to Ref. [156, 157] for THz sources, and Refs. [151, 158] for THz detectors). Therefore, to promote THz science into real applications, we still need to develop novel THz sources, detectors, modulators, and waveguide of high efficiency, which work even at room temperature. On the other hand, the terminology "mid-infrared (MIR) regime" usually refers to the frequencies window between 30 THz and 100 THz[2].

THz imaging in biochemistry and medicine —— Radiations with terahertz to mid-infrared frequncy have various physical meanings in diffrent reasearch areas. For example, in biochemistry and medicine, terahertz spectroscopy plays a crucial role in biological or medical imaging. In this case, most important is the fact that characteristic frequencies of vibrational modes in macromolecules, such as proteins, typically lie in terahertz to mid-infrared frequencies [153]. Since the energy scale of thermal fluctuation at room temperature is also around several terahertz, these collective modes are believed to relate closely to the mechanism of conformational changes and biological functions of biological polymers [159]. By applying THz lights onto chemical or biological systems, we can excite a specific vibrational mode of some molecule coherently, leading to the detection or imaging of target molecules without destroying the electron structure of molecules [160, 161, 162]. Moreover, THz waves can penetrate into many materials that is not transparent in visible light region, and give much higher spatiotemporal resolution than the conventional microwave imaging technology. These properties enable us to utilize the terahertz waves, for example, to develop skin-cancer diagnosis in vivo or other non-destructive biological imaging [163, 164]. Furthermore, the spatial resolution of such THz imaging can be dramatically improved by using metamaterial or plasmonic devices, which can confine THz lights into a small space beyond the diffraction limit [165, 166, 167, 168].

Moreover, the light absorption by water also becomes very strong in the terahertz regime, whose spectrum has a broad peak centred at 5.6 THz due to the resonant stretching of the hydrogen bond between water molecules [169]. As a result, the absorption spectrum in THz regime is highly sensitive to water concentration, which leads to clear contrasts between muscle and adipose tissue [170] and between tumour and normal tissue [171]. These properties are also utilized as an indicator to evaluate the solubility of crystalline drugs in living organisms [169]. Moreover, THz spectroscopy techniques also can be utilized to characterize crystallinity in pharmaceutical drugs, estimate the thickness of tablet coatings, and identify their chemical composition [172]. In this way, THz technologies have promising applications even in the pharmaceutical industry.

THz wireless commnucation —— Furthermore, THz wireless commnucation is also a promising application of terahertz technologies [173, 174, 175]. Accompanied with rapidly growing demand for data communication load and the remarkable speed-up of fiber-optic networks, unoccupied and unregulated communication band is eagerly demanded to construct novel wireless communication, which naturally require the extension of operation frequencies toward the sub-terahertz regime. Fortunately, even though electromagnetic absorption by the atmosphere, or atmosperic attenuation, becomes remarkable at frequencies above 100 GHz, it is known from experiments and numerical simulations that there are certain frequency windows[3] where light attenuation becomes relatively small [176, 177, 178]. Moreover, it is also noteworthy that the antennas with a fixed physical size becomes more directional and gets more gain quadratically as the frequency becomes higher, and the Friis transmission equation suggests that the received

[2]Photon energies of terahertz and mid-infrared radiations range in the energy window 1 - 10 meV and 100 - 400 meV.

[3]Such windows are located at 120 GHz, 300GHz, 350 GHz, 410 GHz, 670 GHz and 850 GHz.

power is proportional to the gain of receiving and transmitting antennas and the inverse of the square of frequency [179]. Therefore, theoretically, the path loss in free space decreases quadratically as the frequency increases, if the antenna size remains constant over frequency at both link ends [175, 180, 181, 182]. Therefore, the common statement that electromagnetic waves with higher frequency surffer from a greater loss is not nocessarily true, and the transmission distance achievable in THz communication crucially depends on the choice of antenna designs and frequency band. One of the major challenges in current terahertz technology is to establish wireless communication techniques in the above frequency windows.

Compared to the conventional wireless communication using radio or millimeter waves, THz wireless communication has a great advantage of ultra-high-speed data transmission. According to the Shannon–Hartley theorem, the maximum rate at which information is transmitted over a noisy communication channel with a certain bandwidth is obtained as

$$C = B \log_2(1 + S/N). \tag{2.7}$$

Here C is the channel capacity, i.e, the tight upper bound on the rate at which information can be reliably transmitted over the communication channel, B is the bandwidth of the channel in Hz, S/N is the signal-to-noise ratio of the communication signals. This means that the channel capacity is proportional to the bandwidth, and thus a higher frequency regime is favorable to achieve high-speed wireless communication. Actually, THz wireless communication is expected to achieve data communication rates of 100 Gbps or higher [175, 183], while the current communication system (5G) typically achieves only several Gbit/s (Gbps) using millimeter waves at several GHz[4]. For example, if 100 Gbps wireless communications are realized, movies in a Blu-ray disc with 25 GB can be downloaded in just two seconds, and uncompressed 4K/8K videos can be transmitted in wireless communications [173, 184].

Furthermore, while THz waves might be disadvantageous in long-distance telecommunication due to inevitable atmosperic attenuation, they have some unique characteristics such as the high directivity and extremely small antennas, in addition to the ultra-high-speed data transmission. High directivity is beneficial in a sense that it reduces spatial interference with other communication systems, even though it makes difficult to construct non-line-of-sight communications and requires an alignment of ransmitter/receiver. Therefore, simultaneous communication between multiple devices are achieved in THz communication by separating high-speed communications spatially, whereas the conventional radio wave communication makes it possible by dividing frequencies into several narrow bands radiate signals even under spatial interferences of signals. Considering the above features, THz communication will have a great potential especially in indoor wireless LAN, device-to-device/intra-device communications, and fixed wireless link in outdoor environment [173, 185]. Moreover, Ref. [175] has discussed the possibility of THz mobile communication by using highly directional steerable antennas.

THz physics in condensed matter physics —— In condensed matter physics, it is well-known that optical phonon modes typically lie in the mid-infrared regime [154], while there exist various collective modes, such as electromagnons in multiferroics [186], magnons in antiferromagnets [187, 188], and the Higgs modes in superconductor [189] in the terahertz regime. Interestingly, the recent developments of high-power light sources in teraherz frequencies enable us to make a high-speed control of the solid states by exciting coherent optical phonon modes [154]. The most prominent example is light-induced superconductivity [190, 191, 192], where the crystal lattice was distorted by a

[4]On the other hand, Wired communications with fiber optic, such as Ethernet and passive optical network (PON), are now reaching data rates of several hundreds Gbps and tens Gbps, respectively [173].

mid-infrared pump pulse, driving the electron systems to nonequilibrium phases, and then superconductor-like behavior, such as Josephson plasma resonances, was observed in the spectrum of the optical conductivity by time-resolved THz spectroscopy. As another example, nonadiabatic excitations of the Higgs mode in superconductors has also been reported by using Terahertz pump pulse, and the temporal evolution is observed via the change of the intensity of transmitted probe THz pulses [193]. Furthermore, Refs. [194, 195] have also reported that a resonance between the optical field and the pumped Higgs modes provokes a remarkably large terahertz third-harmonic generation.

Similarly, polaritons in two-dimensional layered systems typically reside in terahertz to mid-infrared region [71, 139]. Here polariton is a quasiparticle originating from the coupling between electromagnetic waves and some excitation with an electric dipole such as optical phonon and plasmon. For these modes, most remarkable is that they have very long lifetimes and their dispersion is highly controllable by gating, doping, photoexcitation, and dielectric environment, leading to electric or optical tunability of light-matter coupling. Furthermore, these collective modes typically have one or two orders of magnitude smaller wavelength than that of free-lights. This property enables us to achieve a strong light confinement and field enhancement for high-resolution imaging or nano-photonic devices, but at the same time, makes it difficult to couple the polariton modes to lights in free space. As explained latter for plasmonics, by taking advantage of these features, we can attain various novel functionalities [71, 196], including electro-optical modulation or switching [197, 198, 199], subdiffractional focusing and imaging [165, 166, 200, 201], polariton laser [202, 203], strong enhancement of light-matter interaction and optical nonlinearities [204, 205, 206], quantum information processing [207, 208, 209], and nano-photonic waveguides or circuits [210, 211].

2.2.2 Plasmonics

Plasmonics is an active subfield of photonics that utilize surface plasmon-polaritons, which are collective modes resulting from the coupling between electromagnetic waves and charge excitation of electrons, to develop unconventional optoelectronic devices. As with other polaritons, surface plasmon provides a strong light-matter coupling effect, which supports various sensing, imaging, or energy harvesting technology [137, 138, 139, 145, 146, 147, 165, 166], and leads to strong confinement of light and enhancement of local near field, which are favorable for developing nano-photonic devices such as plasmonic nanowaveguides [140, 141, 142]. Moreover, it is noteworthy that the scope of plasmonic applications covers a remarkably broad range of frequency from sub-terahertz to ultraviolet waves. This is attributed to the plasmon's property that the dispersion relation of surface plasmon drastically changes depending on the composition of host materials (Au, Ag, Al, graphene, etc.), their dimensionality (bulk, thin film, nanoribbon, nanoparticle, etc.), the gate voltage, and their dielectric enviroment (dielectric composition, spacer thickness from metallic back-gate, plasmonic lattice). In particular, in the past decade, graphene plasmonics and its hybridization with other 2D nanomaterials are attracting much interest as a new frontier of plasmonics that is suitable for terahertz to mid-infrared applications [137, 138, 139, 149, 212].

Noble metal plasmonics —— The early stage of plasmonics has focused on mainly the surface plasmons on noble metals, such as gold and silver. In the late 1990s, several seminal works have demonstrated extraordinary performance of plasmonic devices over conventional dielectric photonics, which includes one-dimensional optical waveguides with nanometer diameter [213], surface enhanced Raman spectroscopy for single molecule detection [214, 215], extraordinary optical transmission through metal films with nanoscale hole arrays [216], and optical superlens with simple thin slab of silver [217]. Then, these

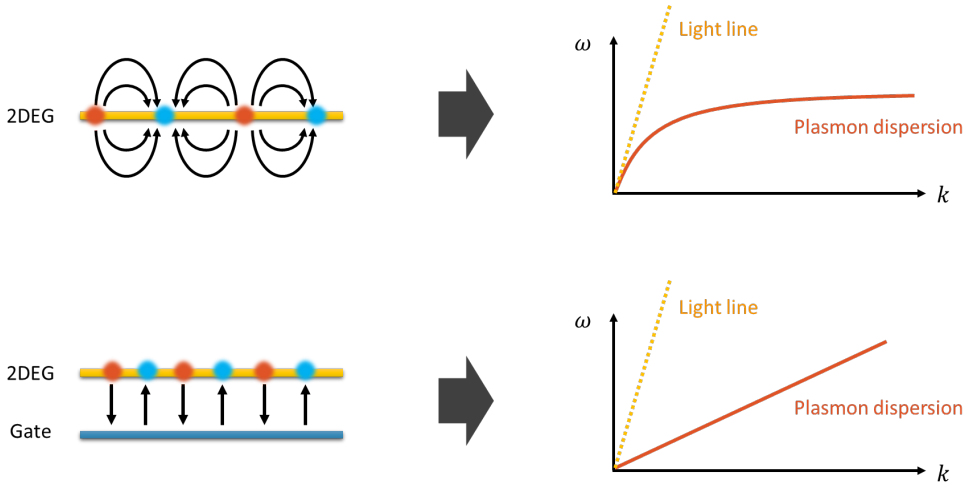

Figure 2.1: Dispersion relations of two-dimensional surface plasmons in ungated and gated cases. The light line in vacuum has also depicted with dotted yellow line.

astonishing discoveries open the way to explosive growth of plasmonics field. The term "plasmonics" was originally coined in 1999 for a promising new device technology that deal with optical properties of metallic nanostructures and aims to achieve routing and active manipulation of light at the nanoscale [140]. Nowadays, noble metal plasmonics deals with various form of plasmonic systems that include metallic nanoparticles and their arrays [218], nanorods, nanoantennas, nanoring resonators [219], plasmonic metamaterial and metasurfaces [220], and chiral plasmonic structures [221]. These plasmonic systems have broad-ranging applications in the visible to near-infrared frequency region, and their promising aplications include nanophotonic devices aiming for integrated photonic systems [222, 223, 224], metamaterials with unusual electromagnetic properties [220, 225, 226, 227, 228], biosensing with metallic nanostructures [229, 230, 231, 232], plasmonic sollar cells [145, 146, 147], and single photon transistors for quantum computing [233, 234, 235]. However, although noble metals are the best choice of plasmonic systems among bulk materials, they are lacking in tunability and always suffer from large Ohmic losses, which limit their applicability as plasmonic devices.

graphene plasmonics —— In this context, graphene has emerged as a novel 2D plasmonic material alternative to conventional noble metallic systems [137, 138, 139, 149, 212]. Graphene plasmon exhibits an remarkably long lifetime and extremely strong light confinement, and it has some unusual properties due to the linear band structure of graphene. Its further appealing property is its high tunability by gating, doping, and chemical means. This enable us to control optical properties of plasmonic devices, such as resonant frequency of surface plasmons, even after the fabrication of the device. Another fascinating point of graphene plasmonics is that the resonances of graphene plasmons typically reside in terahertz to mid-infrared region, which enables new and discriminatory plasmonic application from conventional metal plasmonics. As already mentioned in previous subsection, the terahertz regime has a wide variety of applications from biological imaging to ultrafast wireless communication, and at the same time, it has a lot of difficulties in developing highly efficient THz detectors and sources. Graphene plasmonics and its hybridizaion with other 2D material devices might overcome these difficulties, and are expected to enable the development of highly tunable, compact, and broadband THz devices.

Plasmon coupler —— To explore the utilization of surface plasmons, we have to consider how we can excite and detect surface plasmons. In both cases of noble metal plas-

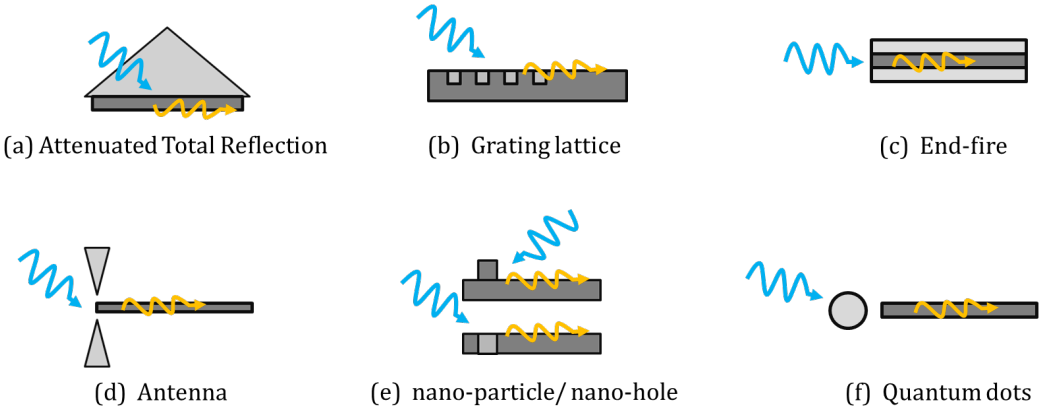

Figure 2.2: Typical examples of plasmonic coupler.

monics and graphene plasmonics, the key concept to solve this problem is the momentum matching between surface plsmons and light in free space. For example, in two-dimensional cases, the dispersion relations of surface plasmons are described as in Fig. 2.1 for ungated and gated cases [150, 236]. From the figures, we readily notice that the dispersion of surface plasmons is decoupled from the light line, and never satisfy the momentum matching without structuring the material's surface. In traditional methods in plasmonics, there are roughly two types of approaches to excite surface plasmons [155]. First one is the attenuated total reflection method (Fig. 2.1 (a)), which utilizes the property of an evanescent wave resulting from the total reflection on interface. For example, in the Kretschmann configuration, the metallic thin film is evaporated onto the glass block. The incident light from glass sides is reflected on the interface between the metal and the glass, and an evanescent wave penetrates through the metal film. This penetrated electric fields excite the surface plasmons at the outer side of the metallic film.

On the other hand, approaches depicted in Fig. 2.1 (b-f) are based on the subwavelength microstructures on the surface or at the edge, such as grating lattices and plasmonic antennas. These microstructures break the continuous translational symmetry on the surface, and relax the strict constraint from momentum matching. Interestingly, recent developments of scanning near-field optical microscopy have enabled us to locally excite the surface plasmons and track the time evolution through real-space imaging of plasmon fields [237, 238].

2.2.3 Electron hydrodynamics in plasmonics

Electron hydrodynamic theory often plays a crucial role to describe the dynamics of plasmon modes and the related optical phenomena [57, 219, 239, 240, 241, 242]. This is mainly because the plasmonics usually focuses on ultra-clean systems with high mobility, where a long lifetime of plasmons is guaranteed and the hydrodynamic conditions are also maybe satisfied, and hydrodynamic theory deals with the macroscopic slow dynamics of conserved quantities and order perameters, which gives a clear description of particle density oscillations, i.e., plasmons and their strong nonlocality/nonlinearity.

Actually, as mentioned in the previous sections, some important plasmonic systems, including two dimensional electron gas in GaAs quantum well [16, 17, 18, 19, 20, 21, 22] and graphene [7, 8, 9, 10, 11, 12, 13, 14], have been reported to realize the hydrodyamic regime via nonlocal transport measurements recently. These astonishing discoveries have encouraged many researchers to study nonlinear and nonlocal optical properties in the novel transport regime. For example, recent theoretical works have investigated the

hydrodynamic-to-ballistic crossover of the plasmon's dispersion, and showed that plasmons could exhibits a phase velocity lower than the Fermi velocity v_F (but greater than $v_F/\sqrt{2}$) in the hydrodynamic regime [85, 243, 244], while the free-particle models predict that the phase velocity of plasmons always lies above the Fermi velocity [245, 246, 247]. In a series of works [82, 86, 87], the authors have developed an anomalous hydrodynamic theory for Weyl semimetals, and predicted the appearance of novel collective modes such as chiral magnetic plasmons and transverse anomalous Hall waves. More recent work [126] has developed the "nonreciprocal hydrodynamic theory", which describes the magneto-hydrodynamic dynamics of electrons in noncentrosymmetric 2D metals under magnetic fields and treats the quantum geometrical properties of the Bloch electrons, and analyzed the enhancement of the directional dichroism in optical reflectance due to the resonant excitation of nonreciprocal magnetoplasmons.

Especially in the context of plasmonics, there are two types of important concepts, the Dyaknov-Shur instability (and related photovoltaic phenomena) [57, 248] and the (plasmonic) ratchet effect [249, 250, 251, 252, 253], both of which are considered as a promising mechanism to develop highly-efficient and tunable plasmonic THz photodetectors or sources. In what follows, we demonstrate how electron hydrodynamic theories are apllied to describe these plasmonic phenomena.

Dyakonov-Shur instability —— Under specific boundary conditions, surface plasmons in ballistic field effect transistors are known to get unstable by applying a dc current, leading to a spontaneous radiation of THz waves of a few mW for a single device and much higher for device arrays [254, 255, 256, 257]. This instability is called as the Dyakonov-Shur instability, and originates from the plasma wave amplification due to the reflection at the device boundaries. This mechanism is somewhat similar to that of sound production in musical instruments, such as organ pipes and flutes [258], which make a beautiful sound by utilizing the sound wave instability under steady flows.

The authors of Ref. [57] have originally predicted the Dyakonov-Shur instability based on a simple hydrodynamic model, which has a form analogous to those for shallow water [259]. Assuming 2D electron systems in a ballistic field effect transistor, their macroscopic dynamics in the hydrodynamic regime can be described with the Euler equation

$$\frac{\partial u}{\partial t} + u\frac{\partial u}{\partial x} = -\frac{e}{m}\frac{\partial U}{\partial x}, \tag{2.8}$$

and the contuity equation for the electron density

$$\frac{\partial U}{\partial t} + \frac{\partial U u}{\partial x} = 0, \tag{2.9}$$

where u is the velocity fields of electron fluids, m is the electron mass, U is the local gate-to-channel voltage. Here, we have assumed that the local electron density n is proportional to the local gate-to-channel voltage U as follows:

$$n = CU/e. \tag{2.10}$$

This approximation is known as the gradual channel approximation. If we consider a static voltage $U = U_0$ and no current bias, we can easily obtain the dispersion relation of surface plasmons $\omega(k) = \pm sk$ ($s = \sqrt{eU_0/m}$) by performing a Fourier transformation of the above equations. On the other hand, if we assume the existence of finite electric current $J_0 = nu_0$, we can predict the Doppler effect of surface plasmons, which have dispersion relations $\omega(k) = (u_0 \pm s)k$.

To accomplish the analysis of plasmon's steady dynamics, we have to solve a boundary value problem under some appropriate boundary conditions. In Ref. [57], M. Dyakonov

and M. Shur have assumed the situation when the source and drain are connected to a current source, and the gate and source are connected to a voltage source. This setup leads to the following boundary conditions:

$$J(x=L) = J_0 = nu_0, \quad U(x=0) = U_0, \tag{2.11}$$

where the source is located at $x = 0$ and the drain is located at $x = L$. Under these boundary conditions (sometimes called the Dyakonov-Shur boundary conditions), we need to determine the coefficients A and B for the plasmonic modes that move in another direction in the following equations:

$$U = U_0 + U_1, \quad U_1(x,t) = \frac{U_0}{s}(Ae^{ik_+x} - Be^{-ik_-x})e^{-i\omega t}, \tag{2.12}$$

$$u = u_0 + u_1, \quad u_1(x,t) = (Ae^{ik_+x} + Be^{-ik_-x})e^{-i\omega t}, \tag{2.13}$$

where $k_\pm = \frac{\omega}{u_0 \pm s}$ This problem can be readily solved as in common exercises in one-dimentional quantum mechanics, and finally, we obtain the following expressions for the real and imaginary parts of the $\omega = \omega' + i\omega''$:

$$\omega' = \frac{|s^2 - u_0^2|}{2Ls}\pi n, \quad \omega'' = \frac{s^2 - u_0^2}{2Ls}\ln\left|\frac{s+u_0}{s-u_0}\right| \tag{2.14}$$

where n is an odd integer for $|u_0| < s$ and an even integer for $|u_0| > s$. As easily understood by plotting the curve of ω'' against the Mach number $M = u_0/s$, we notice that the imaginary part ω'' becomes positive when $u_0 < -s$ or $0 < u_0 < s$. This means that infinitesimal positive current make plasma waves unstable, leading to their spontaneous excitation. Taking the momentum relaxing processes into consideration, the formula for the imaginary part ω'' is modified as follows:

$$\omega'' = \frac{s^2 - u_0^2}{2Ls}\ln\left|\frac{s+u_0}{s-u_0}\right| - \frac{1}{2\tau_{\mathrm{mr}}}. \tag{2.15}$$

This means that plasma waves in realistic clean materials become unstable under finite current bias larger than a specific threshold.

Ratchet effect

In the context of optics or plasmonics, the term "ratchet effect" is used to refer to radiation-induced direct currents in 2DEGs with spatially periodic noncentrosymmetric lateral potential on the surfaces [249, 250, 251, 252, 253]. From a symmetry viewpoint, such a current can be understood to originate from the inversion breaking by built-in asymmetry. On the other hand, the original idea of ratchet effect itself is actively discussed in the context of statistical physics, chemistry and biology, where researchers focus on physical targets such as the Brownian motions and molecular motors [260, 261, 262]. In this context, Ratchet effects in a broad sense means some directed particle transport originating from simultaneous breaking of both thermal equilibrium and spatial inversion symmetry [250]. In this broad sense, any photogalvanic effect might be considered to relate with the ratchet effect, but in the context of plasmonics, the terminology seems to be used only when we refer to the photocurrent due to some artificial noncentrosymmetric lateral potential.

The hydrodynamic formulation of plasmonically-enhanced ratchet effect is also composed of the Euler equation and the continuity equation of particle density [251]:

$$\frac{\partial n'}{\partial t} + \frac{\partial u_x}{\partial x} = -\frac{\partial n' u_x}{\partial x}, \tag{2.16}$$

$$\frac{\partial u_x}{\partial t} + \frac{u_x}{\tau_{\rm mr}} + s^2 \frac{\partial n'}{\partial x} = F_x - u_x \frac{\partial n u_x}{\partial x}, \tag{2.17}$$

$$\frac{\partial u_y}{\partial t} + \frac{u_y}{\tau_{\rm mr}} = F_y - u_x \frac{\partial n' u_y}{\partial x}, \tag{2.18}$$

where $n' = (n - n_0)/n_0$, n_0 is the static electron density, and $\boldsymbol{F} = -(e/m)(\boldsymbol{E} - \boldsymbol{\nabla} V)$, V is a static spatially periodic in-plane potential. In a simplified model of asymmetrical grating gate structures, we can describe the static in-plane potential

$$V(x) = V_0 \cos(qx), \tag{2.19}$$

and the incident electric field is spatially modulated by a grating lattice with the same wavenumber q:

$$\boldsymbol{E}(t, x) = [1 + \hat{h} \cos(qx + \phi)] \boldsymbol{E}_0(t), \tag{2.20}$$

where $E_x(t) = E_{0x} \cos \omega t$ and $E_y(t) = E_{0y} \cos(\omega t + \theta)$. By solving the above equations perturbatively in the following form,

$$n = n^{(0,1)} + n^{(1,0)} + \cdots, \quad \boldsymbol{u} = \boldsymbol{u}^{(0,1)} + \boldsymbol{u}^{(1,0)} + \cdots, \tag{2.21}$$

we can obtain the nonvanishing correction to the dc current in the order $(2, 1)$ as $\boldsymbol{j}_x^{(2,1)} \propto \left\langle n^{(1,0)} \boldsymbol{u}^{(1,1)} \right\rangle$. Here the two indices (a, b) $(a, b = 0, 1, \cdots)$ denote the order of the perturbation with regard to $\tilde{\boldsymbol{E}}_0$ and V_0. By performing the detailed perturbative analyses, we obtain the final results for the plasmonically-enhanced ratchcet current as follows [251]:

$$j_x = j_{0x} \frac{2\omega_q^5 \tau}{(1 + \omega^2 \tau^2)[(\omega^2 - \omega_q^2)^2 + \omega^2/\tau^2]}, \tag{2.22}$$

$$j_y = j_{0y} \frac{\omega_q^3 [(\omega^2 - \omega_q^2)\tau \cos\theta + \omega \sin\theta]}{(\omega^2 - \omega_q^2)^2 + \omega^2/\tau^2}. \tag{2.23}$$

Here $j_{0x} = e^4 V_0 N_0 E_{0x}^2 h_x \sin\phi/(4m^3 s^3 \omega_q^2)$ and $j_{0y} = -e^4 V_0 N_0 E_{0x} E_{0y} h_y \sin\phi/(4m^3 s^3 \omega_q^2)$. As easily understood, these direct currents have a sharp peak at the plasmonic resonance $(\omega = \omega_q)$ under the resonant condition $\omega_q \tau \gg 1$.

Chapter 3

Formulation of anomalous hydrodynamic theory

In this chapter, focusing on crystal symmetries (in particular, spatial inversion symmetry breaking) and the geometry structure of the Bloch wavefunctions, we clarify how they modify hydrodynamic behaviors of electron fluids. This is mainly motivated by the recent observations of hydrodynamic signatures in various noncentrosymmetric conductive materials, including bilayer-graphene, WP_2, and GaAs quantum wells. As a result of this study, we have shown that there is an interesting analogy between electron fluids in noncentrosymmetric materials and chiral fluids, which are believed to be realized in systems with chiral anomalies such as quark gluon plasma. In other words, this means that a new class of electron fluids ("anomalous electron fluids") is realized in these materials, which has not been pointed out so far to our knowledge. At the same time, we have also revealed that such a novel fluid exhibits a variety of fascinating non-linear or non-local phenomena such as *generalized vortical effect*, *asymmetric Poiseuille flow*, *anomalous edge current*, *quantum nonlinear Hall effect*.

In what follows, we first clarify the motivation of this work in more details (Sec. 3.1). Then, we formulate the *generalized Euler equation* that incorporates the quantum geometrical effect into the conventional hydrodynamic equation (Sec. 3.2). Next, based on the obtained theory, we predict several unconventional anomalous transport phenomena mentioned above (Sec. 3.3). It also includes hydrodynamic generalization of already-known phenomena such as the Quantum nonlinear Hall effect and the Magnus Hall effect. Our formulation provides us with a simpler and more unified picture of these phenomena. In Sec. 3.4, we give group-theoretic considerations to classify the universal classes of electron fluids, and we specify experimental setups where novel anomalous transport phemonena mentioned above can be realized. In Sec. 3.5, we also show a quantitative estimation as for the asymmetric Poiseuille flow, based on a strained graphene model with a sublattice potential. In addition, we give a brief comment on the recent studies that follows our work in this chapter (Sec. 3.6). Finally, in Sec. 3.7, we summarize this study with some prospects for future researches.

3.1 Motivation

First, in what follows, let us clarify the main concerns in this chapter. In the indroduction, we have already mentioned various fascinaing transport/optical phenomena and their intuitive intepretation in the hydrodynamic regime, which includes negative nonlocal resistance, violation of the Widemann-Frantz law, and giant negative magnetoresistance. As a conclusion, we have found that these phenomena essentially originate from (i) nonlo-

cality due to the viscosity, (ii) nonlinearlity of hydrodynamics, (iii) non-Fermi liquid-like nature due to the quasiparticle scatterings, most of which can be understood by using the conventional hydrodynamic theory (i.e. the Navier-Stokes equation) or its naive extension. In other words, many of these phenomena can also be realized in conventional fluids such as water and plasma, and are not necessarily unique to electron fluids *in solids*.

Then, what is the essential difference between an *electron fluid in a solid* and a usual fluid in free space, and what characterizes the former more clearly? Possible answers to these questions might be found when considering the symmetry of electron fluids[1]. Unlike fluids in free space, such as water or plasma, electron fluids in solids always exist under the background of a crystal lattice, and hydrodynamic dynamics of the fluids reflects its discrete crystal symmetry. In particular, such a symmetry lowering will lead to novel anisotropic and non-galilean hydrodynamic flows and viscous effects, creating a new class of fluid that cannot be realized in a fluid in free space. From these viewpoints, it seems to be very important challenges to incorporate the effect of symmetry lowerings due to crystal structures into electron fluid dynamics, which would clarify the phenomena unique to electron fluids "in solids".

In particular, electrons in noncentrosymmetric crystals exhibit anomalous transport due to the finite Berry curvature in k-space, which reflects the nontrivial geometrical structure of their Bloch wavefunctions. From a macroscopic viewpoint, such geometrical effects will lead to anomalous nonlinear and nonlocal hydrodynamic flow, enabling a new class of electron fluid ("anomalous electron fluid") to realize. Remarkably, recent experiments in the past few years have reported the realization of hydrodynamic regimes in metals without inversion symmetry, such as MoP, WP_2, WTe_2, bilayer-graphene, and GaAs quantum wells. Consequently it is an urgent problem to clarify how such noncentrosymmetric electron fluids differ from conventional ones and what kind of dynamics they exhibit. Recalling that the Berry curvature essentially represents the inter-band nature under an electromagnetic field, these points might highlight multi-band nature of Bloch electrons in electron hydrodynamics in solids, which is also one of the essential differences between electron fluid in solids and usual fluids in free space.

Motivated by the above viewpoints, in the following, we formulate the hydrodynamic theory for time-reversal-symmetry (TRS) preserved noncentrosymmetric metals, which is correct up to the second order in electric fields. Then, we aim to propose novel hydrodynamic phenomena observable in these materials with modern experimental techniques.

3.2 Formulation of anomalous electron hydrodynamics

In this section, we formulate the electron hydrodynamic theory for time-reversal symmetric and noncentrosymmetric metals. First, starting from the Boltzmann and the semi-classical equations, we derive the continuity equations for each conserved quantity, and give the microscopic expressions for the fluxes of the conserved quantities. Then, assuming the nonequilibrium distribution function can be approximated by a local equilibrium distribution due to the strong electron-electron scatterings, we give hydrodynamic descriptions for these fluxes. In particular, we obtain the generalized Euler equation from the hydrodynamic form of continuity equation of electron momentum. Interestingly, this equation clearly describes the role of crystal symmetry and geometric effects in electron hydro-

[1]Cross-interaction between many internal degrees of freedom (such as spin, orbital, and valley) and various quasiparticles (such as phonons and magnons) is also one of the important features of fluid dynamics in solids. Actually, very recent studies have proposed several frameworks for the spin and valley hydrodynamics [81, 83, 113, 263, 264, 265, 266, 267, 268], or electron-phonon fluids [269, 270], and predicted a variety of unconventional hydrodynamic transport.

dynamics. We also formulate the relations between electric current and hydrodynamic variables such as velocity fields.

3.2.1 Theoretical setups

The first step to derive the hydrodynamic equations is to formulate the continuity equation for (approximately) conserved quantities, such as momentum and particle number [271, 272], by starting with the Boltzmann equation and the so-called semiclassical quation [2]. For electrons in crystals, their dynamics can be described by the following set of equations:

Our starting point for the derivation

$$\text{Boltzmann equation}: \quad \frac{\partial f_\alpha}{\partial t} + \dot{\boldsymbol{r}}\frac{\partial f_\alpha}{\partial \boldsymbol{r}} + \dot{\boldsymbol{k}}\frac{\partial f_\alpha}{\partial \boldsymbol{k}} = \mathcal{C}[f_\alpha]. \tag{3.1}$$

$$\text{Semi-classical equations}: \quad \hbar\dot{\boldsymbol{k}}_\alpha = -e\boldsymbol{E}, \quad \dot{\boldsymbol{r}}_\alpha = \frac{1}{\hbar}\frac{\partial \varepsilon_\alpha(\boldsymbol{k})}{\partial \boldsymbol{k}} - \dot{\boldsymbol{k}}_\alpha \times \boldsymbol{\Omega}_\alpha(\boldsymbol{k}). \tag{3.2}$$

Here α is a valley index, $f_\alpha(t, \boldsymbol{r}, \boldsymbol{k})$ is the nonequilibrium distribution function, $-e$ is the electron charge, ε_α is the energy dispersion for the α band, and $\boldsymbol{\Omega}_\alpha$ is the Berry curvature of Bloch electrons, defined as $\boldsymbol{\Omega}_\alpha \equiv \boldsymbol{\nabla}_{\boldsymbol{k}} \times \boldsymbol{A}_\alpha$ with Bloch wave functions $u_{\alpha\boldsymbol{k}}$ and the Berry connection $\boldsymbol{A}_\alpha \equiv i\langle u_{\alpha\boldsymbol{k}}|\boldsymbol{\nabla}_{\boldsymbol{k}} u_{\alpha\boldsymbol{k}}\rangle$. The last term in the second equation in Eq. (3.2) is known as the anomalous velocity, which is the origin of various anomalous transport phenomena, such as the anomalous Hall effect and the valley Hall effect. It should be noted in particular that the Berry curvature only appears when the systems break the time-reversal or spatial inversion symmetry. Consequently, in time-reversal symmetric systems (i.e. non-magnetic systems), the inversion symmetry should be broken for the systems to exhibit an anomalous hydrodynamic flow due to the Berry curvature.

The right side of Eq. (3.1) is the so-called scattering term. In general, we can decompose it into two different processes, momentum-conserving scattering process and momentum-relaxing scattering process as follows:

$$\mathcal{C}[f_\alpha] = \mathcal{C}^{\mathrm{mr}}[f_\alpha] + \mathcal{C}^{\mathrm{mc}}[f_\alpha]. \tag{3.3}$$

Specifically, the latter term corresponds to normal electron-electron scattering processes, and the former term corresponds to any other scattering processes such as impurity scatterings, electron-phonon scatterings, Umklapp elecron-electron scatterings. Especially when applying the relaxation time approximation to the momentum-relaxing term, we can express it as

$$\mathcal{C}^{\mathrm{mr}}[f_\alpha] = -\frac{f_\alpha - f_{0\alpha}}{\tau_{\mathrm{mr}}}, \tag{3.4}$$

where we have introduced the momentum-relaxing time τ_{mr} and the local Fermi distribution function : $f_{0\alpha}(\boldsymbol{x}, \boldsymbol{p}, t) \equiv [1 + e^{-\beta(\varepsilon_\alpha(\boldsymbol{p})-\mu)}]^{-1}$. Here, for the latter discussion, we note that the momentum integral of the product of some scattering term and its conserved quantity under process is exactly zero [271, 272]. Particularly, this means that momentum integral of $\mathcal{C}^{mc}[f_\alpha]$ always vanishes:

$$\int [d\boldsymbol{p}] p_i \mathcal{C}^{mc}[f_\alpha] = 0, \tag{3.5}$$

where we have used the notation $\int [d\boldsymbol{p}] \equiv \int d\boldsymbol{p}/(2\pi\hbar)^d$.

In the following discussion, the relaxation time approximation is needed only when deriving the continuity equation for electron momentum. On the other hand, for the continuity equation for the particle number, we can treat any scattering terms exactly, since the number of particles is conserved in arbitrary scattering processes. In the following, the Boltzmann equation under the relaxation time approximation is used as our starting point to derive anomalous hydrodynamic equations:

Boltzmann equation under the relaxation time approximation

$$\frac{\partial f_\alpha}{\partial t} + \left(\frac{1}{\hbar} \frac{\partial \varepsilon_\alpha(\boldsymbol{k})}{\partial \boldsymbol{k}} + \frac{e}{\hbar} \boldsymbol{E} \times \boldsymbol{\Omega}_\alpha(\boldsymbol{k}) \right) \frac{\partial f_\alpha}{\partial \boldsymbol{r}} - e\boldsymbol{E} \frac{\partial f_\alpha}{\partial \boldsymbol{k}} = -\frac{f_\alpha - f_{0\alpha}}{\tau_{\mathrm{mr}}} + \mathcal{C}^{\mathrm{mc}}[f_\alpha]. \quad (3.6)$$

3.2.2 Derivation of continuity equations

Following the standard approach [271, 272], we can derive the continuity equations for each conserved quantity, such as momentum, particle numbers and energy. First we multiply the both sides of the Boltzmann equation by the conserved quantity. Then, we integrate it over all the momentum space, which leads to the desired equations. Let us check these procedures below.

(1) Case of particle number

First let us integrate the both sides of the Boltzmann equation, Eq. (3.1), over all the momentum space. Since any scattering process conserves the particle number, the right side of Eq. (3.1) satisfies

$$\int C[f] \frac{d\boldsymbol{p}}{(2\pi\hbar)^d} = 0, \quad (3.7)$$

and then we obtain the continuity equation for particle number:

Continuity equation for particle number

$$\frac{\partial n}{\partial t} + \boldsymbol{\nabla} \cdot \mathbf{J_n} = \mathbf{0}. \quad (3.8)$$

Here we have defined the particle density $n(\boldsymbol{r}, t)$ and the particle flux $\mathbf{J}_n(t, \boldsymbol{r})$ as follows:

$$n(t, \boldsymbol{r}) = \sum_\alpha n_\alpha(t, \boldsymbol{r}) = \sum_\alpha \int f_\alpha(t, \boldsymbol{r}, \boldsymbol{p}) \frac{d\boldsymbol{p}}{(2\pi\hbar)^d}, \quad (3.9)$$

$$\mathbf{J}_n(t, \boldsymbol{r}) = \sum_\alpha \int [d\boldsymbol{p}] \left(\frac{\partial \varepsilon_\alpha}{\partial \boldsymbol{p}} + \frac{e\boldsymbol{E}}{\hbar} \times \boldsymbol{\Omega}_\alpha \right) f_\alpha. \quad (3.10)$$

In particular, under the parabolic approximation $\frac{\partial \varepsilon_\alpha(\boldsymbol{p})}{\partial \boldsymbol{p}} = \frac{\boldsymbol{p}}{m_\alpha}$ for each valley α, the above formulas reduce to more explicit form:

$$\boldsymbol{J}_n(t, \boldsymbol{r}) = \sum_\alpha \langle \boldsymbol{v}_\alpha \rangle = \sum_\alpha \left[\frac{1}{m_\alpha} \boldsymbol{P}_\alpha(t, \boldsymbol{r}) + \frac{e}{\hbar} \boldsymbol{E} \times \tilde{\boldsymbol{\Omega}}_\alpha(t, \boldsymbol{r}) \right],$$

where we have defined the momentum density $\boldsymbol{P}_\alpha$ and the Berry curvature fields $\tilde{\boldsymbol{\Omega}}_\alpha$ as follows:

$$\boldsymbol{P}_\alpha(t, \boldsymbol{r}) \equiv \int \boldsymbol{p} f_\alpha(t, \boldsymbol{r}, \boldsymbol{p}) \frac{d\boldsymbol{p}}{(2\pi\hbar)^d},$$

$$\tilde{\boldsymbol{\Omega}}_\alpha(t,\boldsymbol{r}) \equiv \int \boldsymbol{\Omega}_\alpha(\boldsymbol{p}) f_\alpha(t,\boldsymbol{r},\boldsymbol{p}) \frac{d\boldsymbol{p}}{(2\pi\hbar)^d}.$$

(2) Case of momentum

Next let us integrate the both sides of the Boltzmann equation after multiplying them by crystal momentum $\boldsymbol{p}$. In this case, the scattering terms lead to

$$\int \boldsymbol{p} \cdot C^{mc}[f] \frac{d\boldsymbol{p}}{(2\pi\hbar)^d} = 0, \tag{3.11}$$

$$\int \boldsymbol{p} \cdot C^{mr}[f] \frac{d\boldsymbol{p}}{(2\pi\hbar)^d} \simeq -\sum_\alpha \int \boldsymbol{p} \cdot \frac{f_\alpha(t,\boldsymbol{x}) - f_{0\alpha}(t,\boldsymbol{x})}{\tau_{mr}} \frac{d\boldsymbol{p}}{(2\pi\hbar)^d} = -\frac{\boldsymbol{P}}{\tau_{mr}}. \tag{3.12}$$

Here we have introduced $\boldsymbol{P} = \sum_\alpha \boldsymbol{P}_\alpha$. Combining these results, we obtain the continuity equation for momentum under the relaxation time approximation as follows:

Continuity equation for crystal momentum

$$\frac{\partial P_i}{\partial t} + \frac{\partial \Pi_{ij}}{\partial x_j} + enE_i = -\frac{P_i}{\tau_{mr}}. \tag{3.13}$$

Here $\boldsymbol{P}$ are the momentum density of electrons, Π_{ij} are the momentum flux, which are described microscopically as

$$\Pi_{ij} \equiv \sum_\alpha \int [d\boldsymbol{p}]\ p_i \left(\frac{\partial \varepsilon_\alpha}{\partial p_j} + \frac{e}{\hbar} \varepsilon_{jkl} E_k \Omega_{\alpha,l} \right) f_\alpha. \tag{3.14}$$

Compared to the case of particle number, we notice that the momentum dissipation term and the driving force term have appeared due to the violation of the conservation law of crystal momentum. Under the parabolic approximation, momentum flux can be described as

$$\begin{aligned} \hat{\Pi}(t,\boldsymbol{r}) &\simeq \sum_\alpha \left[\frac{1}{m_\alpha} \int (\boldsymbol{p} \otimes \boldsymbol{p}) f_\alpha(t,\boldsymbol{r},\boldsymbol{p}) \frac{d\boldsymbol{p}}{(2\pi\hbar)^d} + \int \boldsymbol{p} \otimes \left(\frac{e\boldsymbol{E}}{\hbar} \times \Omega_\alpha(\boldsymbol{p}) \right) f_\alpha(t,\boldsymbol{r},\boldsymbol{p}) \frac{d\boldsymbol{p}}{(2\pi\hbar)^d} \right] \\ &= \sum_\alpha \left[\frac{1}{m_\alpha} \langle \boldsymbol{p} \otimes \boldsymbol{p} \rangle_\alpha + \left\langle \boldsymbol{p} \otimes \left(\frac{e\boldsymbol{E}}{\hbar} \times \Omega_\alpha(\boldsymbol{p}) \right) \right\rangle_\alpha \right] \end{aligned} \tag{3.15}$$

and the first term in the last line can be decomposed as follows:

$$\begin{aligned} \langle \boldsymbol{p} \otimes \boldsymbol{p} \rangle_\alpha &= \frac{1}{n_\alpha} \langle \boldsymbol{p} \rangle_\alpha \otimes \langle \boldsymbol{p} \rangle_\alpha + \langle \delta\boldsymbol{p} \otimes \delta\boldsymbol{p} \rangle_\alpha \\ &= \frac{1}{n_\alpha} \boldsymbol{P}_\alpha \otimes \boldsymbol{P}_\alpha + \langle \delta\boldsymbol{p} \otimes \delta\boldsymbol{p} \rangle_\alpha , \end{aligned} \tag{3.16}$$

where we have introduced $\langle \cdots \rangle_\alpha \equiv \int [d\boldsymbol{p}] (\cdots) f_\alpha$ and $\delta\boldsymbol{p} = \boldsymbol{p} - \langle \boldsymbol{p} \rangle_\alpha / n_\alpha$. This means that the first term of momentum flux can be decomposed into the advection term (macroscopic momentum flow) and dissipative term due to momentum fluctuation (microscopic momentum flow).

3.2.3 Local equilibrium approximation

In the hydrodynamic regime, the most essential assumption is that we can describe the distribution functions with the perturbation theory from the following *local equilibrium function* [271, 272]

$$f_{\boldsymbol{u}\alpha}(\boldsymbol{x},\boldsymbol{p},t) \equiv \frac{1}{1+e^{\beta(\varepsilon_\alpha(\boldsymbol{p})-\boldsymbol{u}\cdot\boldsymbol{p}-\mu)}}. \tag{3.17}$$

Here, β, μ and $\boldsymbol{u}$ are the spatiotemporal functions specifying the hydrodynamic variables: (inverse) temperature, chemical potential and velocity. In the following discussion, we further assume that each band structure can be approximated by an isotropic parabolic dispersion with the same effective mass m around some valleys: $\varepsilon_\alpha(\boldsymbol{p}) \simeq \boldsymbol{p}^2/2m$, where $\boldsymbol{p}$ is defined as a deviation from the valley. For example, when considering graphene with inversion breaking or typical ML-TMDs such as MoS_2, the centers of valleys correspond to K and K' point in the Brillouin zone and the above condition is satisfied. On the other hand, hydrodynamic materials with linear dispersion, such as WP_2, do not satisfy this condition for the dispersion. In particular, WP_2 is considered as a Weyl semimetal, and thus it could show a peculiar hydrodynamic flow due to the chiral anomaly. However, we believe that the anomalous hydrodynamic flows predicted by our theory will capture the nature of hydrodynamics in these materials partially, since some of following analyses rely on symmetry consideration of the hydrodynamic materials. Of course, to clarify the role of the linear dispersion or the chiral anomaly at the microscopic level, further discussions beyond our theory will be needed.

Under the above assumptions, for example, we can estimate the momentum density in the zeroth-order approximation for the distribution function as

$$\begin{aligned}\boldsymbol{P} &\equiv \sum_\alpha \int [d\boldsymbol{p}]\boldsymbol{p} f_\alpha \simeq \sum_\alpha \int [d\boldsymbol{p}]\boldsymbol{p} f_{\boldsymbol{u}\alpha} \\ &= \sum_\alpha \int [d\boldsymbol{p}](\boldsymbol{p}+m\boldsymbol{u}) f_{0\alpha}(\boldsymbol{p}) + \mathcal{O}(u^3) \\ &= mn\boldsymbol{u} + \mathcal{O}(u^3),\end{aligned} \tag{3.18}$$

where we have performed a variable transformation $\boldsymbol{p} \to \boldsymbol{p}+m\boldsymbol{u}$ in the second line and used the fact that $f_{\boldsymbol{u}\alpha}(\boldsymbol{p}+m\boldsymbol{u}) = f_{0\alpha}(\boldsymbol{p})+\mathcal{O}(u^3)$ due to the parabolic dispersion. Consequently, the first of the particle flux (3.10) can be described in terms of the velocity field as

$$\begin{aligned}&\sum_\alpha \int [d\boldsymbol{p}] \frac{\partial \varepsilon_\alpha}{\partial \boldsymbol{p}} f_\alpha(\boldsymbol{p}) \\ &\simeq \frac{1}{m}\sum_\alpha \int [d\boldsymbol{p}]\boldsymbol{p} f_{\boldsymbol{u}\alpha}(\boldsymbol{p}) = \frac{\boldsymbol{P}}{m} = n\boldsymbol{u} + \mathcal{O}(u^3).\end{aligned} \tag{3.19}$$

On the other hand, the second term of the particle flux are calculated as follows:

$$\begin{aligned}&\sum_\alpha \int [d\boldsymbol{p}] \frac{e}{\hbar}\varepsilon_{ijk}E_j\Omega_{\alpha,k} f_\alpha \\ &\simeq \sum_\alpha \int [d\boldsymbol{p}] \frac{e}{\hbar}\varepsilon_{ijk}E_j\Omega_{\alpha,k} f_{\boldsymbol{u}\alpha} \\ &= \sum_\alpha \int [d\boldsymbol{p}] \frac{e}{\hbar}\varepsilon_{ijk}E_j\Omega_{\alpha,k}(\boldsymbol{p}+m\boldsymbol{u}) f_{0\alpha} + \mathcal{O}(E^3) \\ &= \frac{em}{\hbar}\sum_\alpha \varepsilon_{ijk}E_j u_l \int [d\boldsymbol{p}] \frac{\partial \Omega_{\alpha,k}}{\partial p_l} f_{0\alpha} + \mathcal{O}(E^3),\end{aligned} \tag{3.20}$$

where, in the third line, we have used the transformation $\boldsymbol{p} \to \boldsymbol{p}+m\boldsymbol{u}$ and the fact that the dispersion can be approximated as a parabolic one. Furthermore, in the final line, we have expanded the Berry curvature in powers of $m\boldsymbol{u}$ and used the fact that the Berry curvature is an odd function of momentum around the Γ point due to the TRS, which means that the sum of the integral of $\boldsymbol{\Omega}_\alpha$ at each valley always becomes zero: $\sum_\alpha \int [d\boldsymbol{p}] \boldsymbol{\Omega}_\alpha f_\alpha = 0$. Moreover, in the both lines, we assume that the velocity field $\boldsymbol{u}$ is driven by an electric field $\boldsymbol{E}$ and drop the terms with more than third order in $\boldsymbol{u}$ and $\boldsymbol{E}$. Finally, we end up with the hydrodynamic expression of the particle flux, which is correct up to the second order in $\boldsymbol{u}$ and $\boldsymbol{E}$, as follows:

Hydrodynamic expression of the particle flux

$$\boldsymbol{J}_n = n\boldsymbol{u} + \frac{em}{\hbar} \boldsymbol{E} \times {}^t\hat{D}\boldsymbol{u}. \tag{3.21}$$

where the symbol t denotes the transpose of a matrix and D_{il} is a geometrical coefficient, so-called Berry curvature dipole, defined as

$$D_{il} = \sum_\alpha D_{il}^\alpha, \quad D_{il}^\alpha \equiv -\int [d\boldsymbol{p}] \Omega_{\alpha,l} \frac{\partial f_{0\alpha}}{\partial p_i}, \tag{3.22}$$

As for the momentum flux (3.14), by performing similar procedures, we can obtain the hydrodynamic expression. First, as already mentioned, we can decompose the first term of Eq. (3.14) into two terms as

$$\begin{aligned} \sum_\alpha \int [d\boldsymbol{p}]\ p_i \frac{\partial \varepsilon_\alpha}{\partial p_j} f_\alpha &= \frac{1}{m} \sum_\alpha \int [d\boldsymbol{p}]\ p_i p_j f_\alpha \\ &= \frac{1}{m} \sum_\alpha \left[\frac{1}{n_\alpha} \langle p_i \rangle_\alpha \langle p_j \rangle_\alpha + \langle \delta p_i \delta p_j \rangle_\alpha \right], \end{aligned} \tag{3.23}$$

where $\langle \cdots \rangle_\alpha \equiv \int [d\boldsymbol{p}] (\cdots) f_\alpha$, $n_\alpha \equiv \int [d\boldsymbol{p}] f_\alpha$ and $\delta\boldsymbol{p} \equiv \boldsymbol{p} - \langle \boldsymbol{p} \rangle_\alpha / n_\alpha$. From the calculation in Eq. (3.18), we obtain $\langle \boldsymbol{p} \rangle_\alpha = m n_\alpha \boldsymbol{u}$ and thus, the first term of Eq. (3.23) can be described in terms of the velocity field as

$$\frac{1}{m} \sum_\alpha \frac{1}{n_\alpha} \langle p_i \rangle_\alpha \langle p_j \rangle_\alpha . = m n u_i u_j \tag{3.24}$$

Next, we estimate the the second term of Eq. (3.23) can be estimated as follows. As can be easily seen, the off-diagonal term of $\langle \delta p_i \delta p_j \rangle_\alpha$ is always zero due to the isotropy of the band around each valley: $\langle \delta p_i \delta p_j \rangle_\alpha = 0$ $(i \neq j)$. On the other hand, the diagonal terms of $\langle \delta p_i \delta p_j \rangle_\alpha$ are calculated as follows:

$$\begin{aligned} \frac{1}{m} \sum_\alpha \langle \delta p_i \delta p_i \rangle_\alpha &= \frac{1}{m} \sum_\alpha \int [d\boldsymbol{p}] (p_i - m_\alpha u_i)^2 f_{\boldsymbol{u}\alpha}(t, \boldsymbol{r}, \boldsymbol{p}) \\ &= \frac{1}{m} \sum_\alpha \int [d\boldsymbol{p}] p_i^2 f_{0\alpha}(t, \boldsymbol{r}, \boldsymbol{p}) \\ &= \frac{1}{m} \sum_\alpha \frac{1}{d} \int [d\boldsymbol{p}] \boldsymbol{p}^2 f_{0\alpha}(t, \boldsymbol{r}, \boldsymbol{p}) \\ &= \frac{1}{m} \sum_\alpha \frac{2m}{d} \int [d\boldsymbol{p}] \varepsilon_\alpha(\boldsymbol{p}) f_{0\alpha}(t, \boldsymbol{r}, \boldsymbol{p}) \\ &= \frac{2}{d} \varepsilon(\boldsymbol{r}, t) = P \end{aligned} \tag{3.25}$$

where, in the first line, we have used the relation $\delta\boldsymbol{p} \equiv \boldsymbol{p} - \langle\boldsymbol{p}\rangle_\alpha / n_\alpha = \boldsymbol{p} - m\boldsymbol{u}$ and, in the second line, we have performed the transformation $\boldsymbol{p} \to \boldsymbol{p} + m\boldsymbol{u}$. Furthermore, in the final equality, we have applied the familiar formula between the energy density ε and the pressure P for the Fermi gas system: $P = 2\varepsilon/d$ [273].

Next, we estimate the second term of Eq. (3.14). Performing the usual transformation $\boldsymbol{p} \to \boldsymbol{p} + m\boldsymbol{u}$, this term can be transformed as

$$\begin{aligned} &\frac{e}{\hbar}\varepsilon_{jkl}E_k \sum_\alpha \int [d\boldsymbol{p}]\Omega_{\alpha,l}(\boldsymbol{p}) f_\alpha(\boldsymbol{p}) \\ &= \frac{e}{\hbar}\epsilon_{jkl}E_k \sum_\alpha \int [d\boldsymbol{p}](p_i + m_\alpha u_i)\Omega_{\alpha,l}(\boldsymbol{p} + m_\alpha\boldsymbol{u}) f_{0\alpha}(\boldsymbol{p}). \end{aligned} \tag{3.26}$$

As with the procedure in Eq. (3.20), by expanding this term in powers of $\boldsymbol{u}$, we can approximate it within the second order in $\boldsymbol{u}$ and $\boldsymbol{E}$ as follows:

$$\begin{aligned} &= \frac{e}{\hbar}\epsilon_{jkl}E_k \sum_\alpha \int [d\boldsymbol{p}](p_i + m_\alpha u_i) \\ &\qquad \times \left(\Omega_{\alpha,l} + m_\alpha u_n \frac{\partial\Omega_{\alpha,l}}{\partial p_n}\right) f_{0\alpha}(\boldsymbol{p}) + \mathcal{O}(E^3) \\ &= \frac{e}{\hbar}\epsilon_{jkl}E_k \sum_\alpha \int [d\boldsymbol{p}] p_i \Omega_{\alpha,l} f_{0\alpha}(\boldsymbol{p}) + \mathcal{O}(E^3) \\ &= \frac{e}{\hbar}\epsilon_{jkl}C_{il}E_k + \mathcal{O}(E^3), \end{aligned} \tag{3.27}$$

where C_{il} is the second geometrical coefficient, defined as

$$C_{il} = \sum_\alpha C_{il}^\alpha, \quad C_{il}^\alpha \equiv \int [d\boldsymbol{p}]\ p_i \Omega_{\alpha,l} f_{0\alpha}. \tag{3.28}$$

In the second line, we have used the fact that the Berry curvature is an odd function of momentum around the Γ point due to the TRS and, in addition, dropped the term proportional to $E_k u_i u_n$ since it is in the order of E^3.

Finally, substituting Eqs. (3.23)-(3.27) into Eq. (3.14), we end up with the hydrodynamic expression of the momentum flux, which are correct up to the second order in $\boldsymbol{u}$ and $\boldsymbol{E}$:

Hydrodynamic expression of the momentum flux

$$\Pi_{ij} = mnu_iu_j + P\delta_{ij} + \frac{e}{\hbar}\epsilon_{jkl}C_{il}E_k. \tag{3.29}$$

We note that, at least in our assumption for band dispersions, it is shown that the trace component of $\hat{C}$ always vanishes because the Berry curvature is divergence free. This can be easily seen as follows:

$$\begin{aligned} C \equiv \mathrm{Tr}[\hat{C}] &= \int [d\boldsymbol{p}] p_i \Omega_{\alpha,i} f_{0\alpha} \\ &\propto \int [d\boldsymbol{p}] \frac{\partial\varepsilon}{\partial p_i} \Omega_{\alpha,i} f_{0\alpha} \\ &= \int d\varepsilon f_{0\alpha}(\varepsilon) \oint_{\varepsilon_\alpha(\boldsymbol{k})=\varepsilon} (d\boldsymbol{S}\cdot\Omega_\alpha(\boldsymbol{k})) \\ &= 0. \end{aligned} \tag{3.30}$$

Here, at the third line, we have performed the variable transformation $d\boldsymbol{k} = dSdk_\perp = \frac{dS}{|\boldsymbol{\nabla}_{\boldsymbol{k}}\varepsilon|}d\varepsilon$, where dS is the area element on the isoenergy surface with $\varepsilon_\alpha(\boldsymbol{k}) = \varepsilon$. Furthermore, at the final equation, we have used the fact that the Berry curvature is divergence free.

3.2.4 Hydrodynamic equations

Substituting the above expression into the continuity equations (3.13) and (3.8), we obtain the desired hydrodynamic equations for noncentrosymmetric metals, in the approximation up to the second order in $\boldsymbol{u}$ and $\boldsymbol{E}$:

$$\frac{\partial n}{\partial t} + \boldsymbol{\nabla}\cdot(n\boldsymbol{u}) + \frac{em}{\hbar}\boldsymbol{\nabla}\cdot\left(\boldsymbol{E}\times{}^t\hat{D}\boldsymbol{u}\right) = 0, \tag{3.31}$$

$$\begin{aligned}&\frac{\partial u_i}{\partial t} + (\boldsymbol{u}\cdot\boldsymbol{\nabla})u_i + \frac{1}{\rho}\frac{\partial p}{\partial x_i} + \\ &\frac{e}{mn\hbar}\epsilon_{jkl}\left[C_{il}\frac{\partial E_k}{\partial x_j} + \frac{\partial C_{il}}{\partial x_j}E_k\right] + \frac{e}{m}E_i = -\frac{u_i}{\tau_{mr}}.\end{aligned} \tag{3.32}$$

Furthermore, the derivative of the coefficient C_{il}^α can be estimated explicitly as

$$\begin{aligned}\frac{\partial C_{il}^\alpha}{\partial x_j} &= \int [d\boldsymbol{p}]p_i\Omega_{\alpha,l}\frac{\partial}{\partial x_j}f_0(t,\boldsymbol{r},\boldsymbol{p}) \\ &= \int [d\boldsymbol{p}]p_i\Omega_{\alpha,l}\left[-\frac{1}{T^2}\frac{\partial T}{\partial x_j}\frac{\partial f_{0\alpha}}{\partial\beta} + \frac{\partial\mu}{\partial x_j}\frac{\partial f_{0\alpha}}{\partial\mu}\right] \\ &= \frac{mF_{il}^\alpha}{T}\frac{\partial T}{\partial x_j} + mD_{il}^\alpha\frac{\partial\mu}{\partial x_j}\end{aligned} \tag{3.33}$$

where we have defined the third geometrical coefficients as

$$F_{il}^\alpha \equiv -\int [d\boldsymbol{p}]p_i\varepsilon_\alpha\Omega_{\alpha,l}\frac{\partial f_{0\alpha}}{\partial\varepsilon}. \tag{3.34}$$

Substituting this formula into Eq. (3.32), we reach the generalized Euler equation as follows, which is one of our main results:

Generalized Euler equation for noncentrosymmetric electron fluids

$$\begin{aligned}&\frac{\partial\boldsymbol{u}}{\partial t} + (\boldsymbol{u}\cdot\boldsymbol{\nabla})\boldsymbol{u} + \frac{\boldsymbol{\nabla}P}{\rho} + \frac{e}{n\hbar}\left[\frac{1}{m}\hat{C}(\boldsymbol{\nabla}\times\boldsymbol{E})\right. \\ &\left.+\hat{F}\left(\boldsymbol{E}\times\frac{\boldsymbol{\nabla}T}{T}\right) + \hat{D}(\boldsymbol{E}\times\boldsymbol{\nabla}\mu)\right] + \frac{e}{m}\boldsymbol{E} = -\frac{\boldsymbol{u}}{\tau_{mr}}.\end{aligned} \tag{3.35}$$

This result indicates that the symmetry lowering of the crystal leads to the emergence of novel anomalous forces in the conventional Euler equation and, as seen below, these forces drive an unusual electric flow accompanied by non-uniformity of hydrodynamic variables. In the later parts of this chapter, we will give a further analysis on the relation between the equation and the crystal symmetry.

Here it is also remarkable that, even though our fluids have no chiral anomaly, the obtained equation has a quite similar form to that of inviscid chiral fluids, which is believed to realize in quark-gluon plasmas [4, 274]. This fact is expected to pave the way for the realization of the anomalous nonlinear transport analogous to that in chiral fluids, even in condensed matter systems without chiral anomaly.

3.2.5 Hydrodynamic expression for the transport current

Next, we move on to the derivation of the hydrodynamic expression for the transport current. To relate the hydrodynamic theory with an observable current, we further need to describe the so-called "transport current" [275] in terms of velocity field $\boldsymbol{u}$. Generally, the current is known to be described with orbital magnetization $\boldsymbol{M}$ in the following form [275, 276]:

$$\boldsymbol{J} = -e\boldsymbol{J}_n + \boldsymbol{\nabla} \times \left(\sum_\alpha \int [d\boldsymbol{p}] \boldsymbol{m}_\alpha f_\alpha \right) - \boldsymbol{\nabla} \times \boldsymbol{M}, \tag{3.36}$$

where $\boldsymbol{m}_\alpha(\boldsymbol{p})$ is the angular momentum of the wave packet. Especially in the equilibrium state, the orbital magnetization $\boldsymbol{M}$ is expressed as

$$\begin{aligned} \boldsymbol{M} = &\sum_\alpha \int [d\boldsymbol{p}]\ \boldsymbol{m}_\alpha f_\alpha + \sum_\alpha \frac{1}{\beta} \\ &\times \int [d\boldsymbol{p}]\ \frac{e}{\hbar} \boldsymbol{\Omega}_\alpha \cdot \log\left(1 + e^{-\beta(\varepsilon_\alpha - \mu)}\right). \end{aligned} \tag{3.37}$$

In this study, to estimate the orbital magnetization in the local-equilibrium state, we phenomenologically assume that the microscopic expression is obtained by replacing the exponent ε_α in Eq. (3.37) with $\varepsilon_\alpha - \boldsymbol{u}\cdot\boldsymbol{p}$. Although this prescription is kind of phenomenological, the resulting formula obtained below seems to support the validity, because it guarantees the equivalence between the external electric field $\boldsymbol{E}$ and statistical force $\boldsymbol{\nabla}\mu$ for the transport current.

Under this assumption, we can express the transport current as

$$\begin{aligned} \boldsymbol{j} = &-e \sum_\alpha \int \dot{\boldsymbol{r}}_\alpha f_\alpha(t, \boldsymbol{r}, \boldsymbol{p}) \frac{d\boldsymbol{p}}{(2\pi\hbar)^d} \\ &- \sum_\alpha \boldsymbol{\nabla} \times \frac{1}{\beta} \int [d\boldsymbol{p}] \frac{e}{\hbar} \boldsymbol{\Omega}_\alpha(\boldsymbol{p}) \cdot \log\left(1 + e^{-\beta(\varepsilon_\alpha - \boldsymbol{u}\cdot\boldsymbol{p} - \mu)}\right). \end{aligned} \tag{3.38}$$

For the integration in the second term, we can estimate it up to the second order in $\boldsymbol{u}$:

$$\begin{aligned} &\frac{1}{\beta} \int [d\boldsymbol{p}] \frac{e}{\hbar} \boldsymbol{\Omega}_\alpha(\boldsymbol{p}) \cdot \log\left(1 + e^{-\beta(\varepsilon_\alpha - \boldsymbol{u}\cdot\boldsymbol{p} - \mu)}\right) \\ &= \int [d\boldsymbol{p}] \frac{e}{\hbar} \boldsymbol{\Omega}_\alpha(\boldsymbol{p}) (\boldsymbol{u}\cdot\boldsymbol{p}) f_0(t, \boldsymbol{r}, \boldsymbol{p}) + \mathcal{O}(u^3) \\ &\simeq \frac{e}{\hbar} {}^t\hat{C}^\alpha(\boldsymbol{r}) \boldsymbol{u}(\boldsymbol{r}), \end{aligned} \tag{3.39}$$

where we have used the fact that the Berry curvature is an odd function of the momentum around the Γ point due to the TRS. Finally, using the formula (3.33), we reach the hydrodynamic expression for the transport current as follows:

Relation between electric currents and velocity fields

$$\begin{aligned} \boldsymbol{J} = &-en\boldsymbol{u} - \frac{e}{\hbar} \Big[m(e\boldsymbol{E} + \boldsymbol{\nabla}\mu) \times ({}^t\hat{D}\boldsymbol{u}) \\ &+ \boldsymbol{\nabla} \times \left({}^t\hat{C}\boldsymbol{u} \right) + m(\boldsymbol{\nabla}T/T) \times ({}^t\hat{F}\boldsymbol{u}) \Big], \end{aligned} \tag{3.40}$$

where the first term is the conventional part appearing in the familiar hydrodynamics, and the others are anomalous parts reflecting the symmetry lowering of the fluids. Here, we note that $\boldsymbol{\nabla}$ does not act on $\hat{C}$. Remarkably, the second term in the bracket denotes

a generalization of *chiral vortical effect* in chiral fluids [4], because the term includes an anomalous current induced by the vorticity fields, which supports the above analogy. This phenomenon can be intuitively understood as the correction due to a magnetization current induced by the inhomogeneous velocity fields through the orbital Edelstein effect [277, 278]. In the following, we refer to this effect as *generalized vortical effect* (GVE).

Here, we note that the above expression of the current does not include the full intrinsic contributions with the first-order of spacial gradient. This is because, in the derivation of Eq. (3.40), we drop the contribution of the first-order deviation of the non-equilibrium distribution function from Eq. (3.17). Consequently, to recover the dropped contributions such as the Fourier's law for thermal gradient, we must proceed to the calculation of the next order perturbation, which is roughly proportional to the electron-electron scattering time τ_{ee} and thus negligible in the strong correlation limit ($\tau_{ee} \to 0$).

On the other hand, in optical experiments or scanning magnetic microscopy, we should consider the so-called local current, rather than transport current. For this case, as shown in Ref. [126], we can obtain a similar hydrodynamic formula, which is equivalent to Eq. (3.40) with geometrical coefficient C replaced by another geometrical coefficient,

$$\hat{M} = \sum_{\alpha} \hat{M}^{\alpha}, \quad M_{ij}^{\alpha} \equiv \int [d\boldsymbol{p}] \frac{\partial m_j^{\alpha}}{\partial p_i} f_{0\alpha}. \tag{3.41}$$

3.2.6 Summary of derivations

Summarizing the discussions so far, we have obtained two important hydrodynamic equations for noncentrosymmetric metals: Generalized Euler equation (3.35) and the hydrodynamic expression of transport current (3.40). By solving the former equation, we can analyze the dynamics of velocity field or momentum density. Then, by substituting the solutions into the hydrodynamic relation (3.40), we can estimate the observable dynamics of electric current.

Summary of our hydrodynamic theory

Generalized Euler equation:

$$\begin{aligned} &\frac{\partial \boldsymbol{u}}{\partial t} + (\boldsymbol{u}\cdot\boldsymbol{\nabla})\boldsymbol{u} + \frac{\boldsymbol{\nabla} P}{\rho} + \frac{e}{n\hbar}\left[\frac{1}{m}\hat{C}(\boldsymbol{\nabla}\times\boldsymbol{E})\right. \\ &\left. + \hat{F}\left(\boldsymbol{E}\times\frac{\boldsymbol{\nabla} T}{T}\right) + \hat{D}(\boldsymbol{E}\times\boldsymbol{\nabla}\mu)\right] + \frac{e}{m}\boldsymbol{E} = -\frac{\boldsymbol{u}}{\tau_{mr}}, \end{aligned} \tag{3.42}$$

Hydrodynamic description of transport current:

$$\begin{aligned} \boldsymbol{J} = &-en\boldsymbol{u} - \frac{e}{\hbar}\left[m(e\boldsymbol{E}+\boldsymbol{\nabla}\mu)\times({}^{t}\hat{D}\boldsymbol{u})\right. \\ &\left. + \boldsymbol{\nabla}\times\left({}^{t}\hat{C}\boldsymbol{u}\right) + m(\boldsymbol{\nabla}T/T)\times({}^{t}\hat{F}\boldsymbol{u})\right]. \end{aligned} \tag{3.43}$$

In the following, we will demonstrate how to use our hydrodynamic theory to describe various transport or optical phenomena, and give a further analysis on the relation between the equation and the crystal symmetry, based on the group theoretical method.

3.3 Results for Anomalous transport

In this section, we give several demonstrations of our hydrodynamic theory, which include nonlinear optical or thermal responses and finite size effects in the fluids. From the symmetry viewpoint, it is noteworthy that linear and local anomalous responses, such as the anomalous (thermal) Hall effect, are prohibited by TRS, so that nonlocal or nonlinear anomalous responses play a key role in our fluids.

First, in Sec. 3.3.1, we explain how to describe linear and nonlinear optical responses within our framework, and check the consistency with familiar results from the Drude theory or usual kinetic approaches. Next, we briefly discuss the responses to thermal gradient ∇T and chemical potential gradient $\nabla\mu$ in Sec. 3.3.2. Finally, we discuss unconventional hydrodynamic flow in narrow channels, dubbed *anomalous edge current* and *asymmetric Poiseuille flow*. These phenomena clearly characterize the electron hydrodynamics in noncentrosymmetric metals, and are believed to be observable through cutting edge technology of scanning magnetic microscope based on diamond NV centors [24, 33, 47, 48].

3.3.1 Linear and nonlinear optical responses

First, for the simplest problem, let us consider the first- and second- responses to a uniform electric field. In this case, we can express electric fields as $\boldsymbol{E} = \mathrm{Re}[\tilde{\boldsymbol{E}}e^{i\omega t}]$ with $\tilde{\boldsymbol{E}} \in \mathbb{C}$, and the electric current is denoted in the form $J_i = \mathrm{Re}[J_i^0 + J_i^\omega e^{i\omega t} + J_i^{2\omega} e^{2i\omega t}]$. Substituting the solution of Eq. (3.35) to Eq. (3.40), we easily reach the following expression of the linear and nonlinear conductivity tensor:

Drude conductivity and quantum nonlinear Hall susceptibility

$$\sigma^{(1)} = \frac{\sigma_D}{1+i\omega\tau_{mr}},\ \sigma^{(2)}_{ijk} = -\varepsilon_{ilk}\frac{e^3\tau_{mr}}{2(1+i\omega\tau_{mr})}D_{jl}, \tag{3.44}$$

where $J_i^\omega = \sigma^{(1)}\tilde{E}_i$, $J_i^0 = \sigma^{(2)}_{ijk}\tilde{E}_j\tilde{E}_k^*$, $J_i^{2\omega} = \sigma^{(2)}_{ijk}\tilde{E}_j\tilde{E}_k$ and $\sigma_D = ne^2\tau_{mr}/m$. The linear one is so-called Drude conductivity, and the nonlinear one agrees with the results of the quantum nonlinear Hall effect (QNHE) [279]. Under TRS, the QNHE gives a leading anomalous current, which has already been observed in several materials including hydrodynamic materials such as GaAs quantum well [249, 280, 281] and BL-graphene [282]. This result indicates that our theory can correctly reproduce the known results for the uniform electric responses formulated so far in the momentum-dissipative or ballistic regimes, but not in the hydrodynamic regime.

3.3.2 Anomalous thermoelectric responses

Furthermore, our hydrodynamic theory elucidates the anomalous nonlinear/nonlocal responses under non-uniform hydrodynamic variables. Let us start with the nonlinear thermoelectric transport induced by the coupling between $\boldsymbol{\nabla}T$ and $\boldsymbol{E}$. Imposing a uniform thermal gradient and electric field on the fluids, we obtain the following anomalous contribution proportional to the product of $\boldsymbol{\nabla}T$ and $\boldsymbol{E}$:

$$\boldsymbol{J}' = \frac{e^2}{\hbar T}\frac{\tau_{mr}}{1+i\omega\tau_{mr}}\left[\hat{F}(\tilde{\boldsymbol{E}}\times\boldsymbol{\nabla}T) + \boldsymbol{\nabla}T\times({}^t\hat{F}\tilde{\boldsymbol{E}})\right]. \tag{3.45}$$

Under TRS, this contribution gives a leading anomalous current under the thermal gradient. Interestingly, the second term is always perpendicular to $\boldsymbol{\nabla}T$, whereas the other is directed only by the tensor $\hat{F}$, whose form is determined by the crystal symmetry as shown

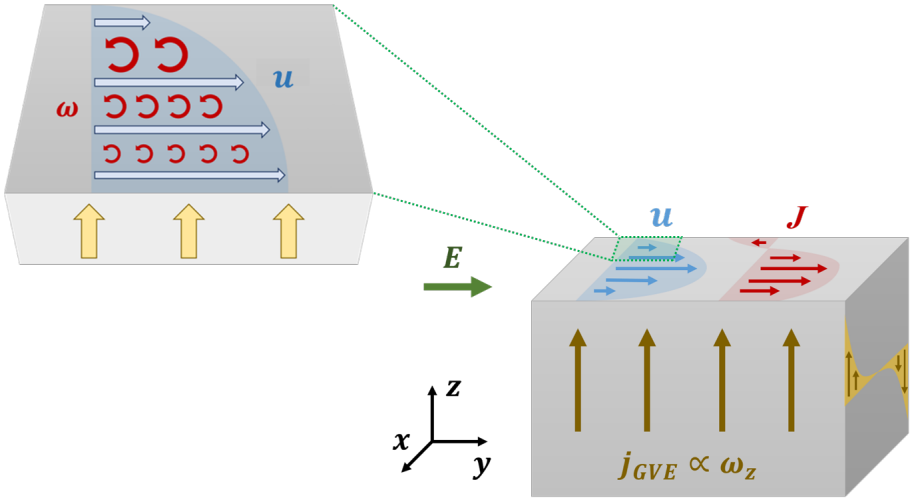

Figure 3.1: **Right**: Schematic picture of the asymmetric Poiseuille flow (red) and anomalous edge current (yellow) induced by the GVE in a 3D sample with finite width w in the x-direction. **Left**: Spatial profile of velocity field near the boundary of the sample. In Poiseuille flow, electron fluids have large velocity gradients and resulting vorticity field localized near the boudary, leading to anomalous surface currents.

below. These features enable us to control or switch the current direction by changing either direction of $\boldsymbol{\nabla} T$ or $\boldsymbol{E}$ without changing the other. Similar responses are also discussed in dissipative (ohmic) regime in Ref. [283]. Similarly, from our theory, we can calculate an anomalous current under chemical potential bias, which is proportional to the product of $\boldsymbol{E}$ and $\boldsymbol{\nabla}\mu$ and described by the Berry curvature dipole as in the case of QNHE. This phenomenon is in contrast to the *Magnus Hall effect*, which has been formulated in the ballistic regime [284] and describes the Hall current responding to $\boldsymbol{E} \parallel \boldsymbol{\nabla}\mu$. We note that our result is qualitatively different from that in Ref. [284], since the former describes the transport in the hydrodynamic regime and includes an anomalous response to $\boldsymbol{E} \perp \boldsymbol{\nabla}\mu$ as well as the correction due to the magnetization current.

3.3.3 Asymmetric Poiseuille flow and anomalous edge current

The most significant consequence of our theory is that the combination of the GVE and the viscosity effect gives rise to an unprecedented current flow in finite size systems, which is unexplored so far. For the demonstration, we consider the Poiseuille flow in 3D samples with finite width w in the x-direction (Fig. 3.1), which most clearly characterizes the hydrodynamic transport in noncentrosymmetric metals. Here, to estimate boundary effects, we introduce the viscosity term $\nu\Delta u$ into the Euler equation (3.35) [285]. When we apply an electric field in the y-direction, the electron fluids form the Poiseuille flow as in Fig. 3.1 and the velocity profile is given by

$$u_y(x) = \frac{e\tau_{mr}E}{m}\left[1 - \frac{\cosh(x/l)}{\cosh(w/2l)}\right], \tag{3.46}$$

and the vorticity is also calculated as

$$\omega_z(x) = \frac{\partial u_y}{\partial x} = \frac{e\tau_{mr}E}{ml}\frac{\sinh(x/l)}{\cosh(w/2l)}, \tag{3.47}$$

where $-w/2 \le x \le w/2$ and $l \equiv \sqrt{\nu\tau_{mr}}$. The expression (3.47) indicates that the vorticity distributes over a width of l from the boundaries. Using Eq. (3.40), the electric current is obtained as

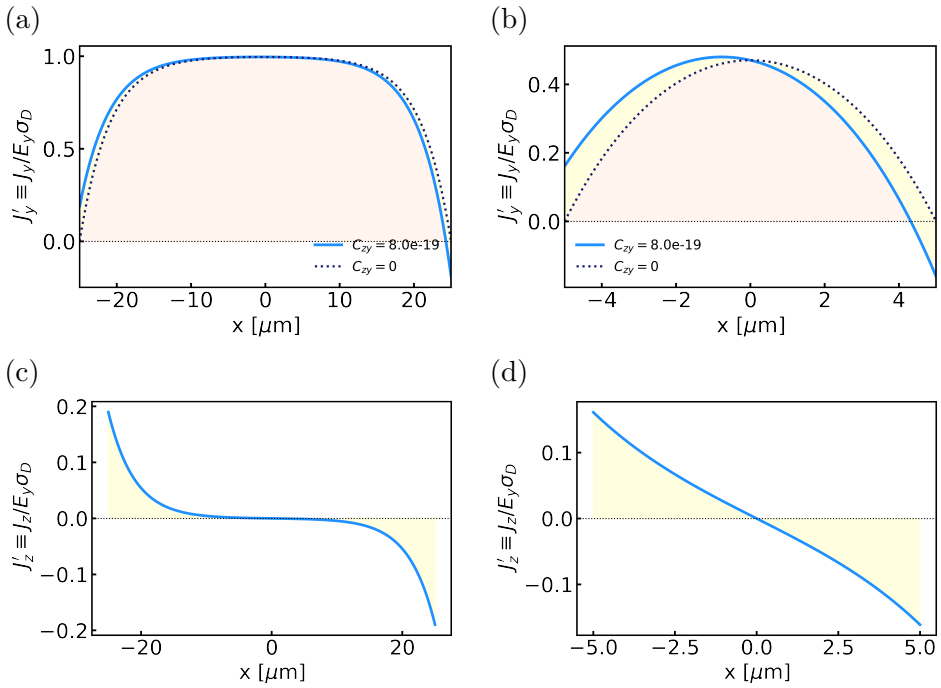

Figure 3.2: Plot of the normalized current profiles $j'_y(x)$ and $j'_z(x)$ in the x-range $[-w/2, w/2]$ [286]. (a), (c) : $w = 50\,\mu$m and (b), (d) : $w = 10\,\mu$m. We use the parameters; $\nu = 3.8 \times 10^{-2}$ m^2/s, $\tau_{mr} = 5 \times 10^{-10}$ s, $m = 1.2m_e$, $C_{yy} = C_{zy} = 8.0 \times 10^{-19}$ kg/s, where m_e is the bare electron mass. Here, the dotted lines in (a) and (b) show the usual Poiseuille flow realized in centrosymmetric metals ($C_{zy} = 0$).

Asymmetric Poiseuille flow and anomalous edge current

$$J_y = -enu_y + (e/\hbar)C_{yz}\omega_z, \;\; J_z = -(e/\hbar)C_{yy}\omega_z. \tag{3.48}$$

These results demonstrate the realization of two unprecedented phenomena : *anomalous edge currents* and *asymmetric Poiseuille flow*. Firstly, the second equation indicates that, through the diagonal component C_{yy}, the vorticity fields induce the z-directed anomalous current localized over a width of l from the boundaries (Fig. 3.1), which is directed oppositely at two sides. Secondly, the first equation means that the off-diagonal component C_{yz} causes an antisymmetric current distribution in the x-direction, which leads to the realization of an asymmetric x-distribution of the total current, i.e. *asymmetric Poiseuille flow*. In particular, it is noteworthy that, in the anomalous flow, there arises a backflow of electric current at one side, which is directed against the electric field. For example, as we discuss below, these phenomena could be realized in the hydrodynamic material such as WP_2, where we can estimate the length l as $w = 4\,\mu$m, using the typical values $\nu = 3.8 \times 10^{-2}$ m^2/s, $\tau_{mr} = 5 \times 10^{-10}$ s in the experiments at 4K [23]. In Fig. 3.2, we plot the current profile for width $w = 50\,\mu$m and $w = 10\,\mu$m with the above values of the parameters. Another possibility to detect the GVE is the measurement of the nonlocal resistivity in the so-called vicinity geometry [7, 31]. In this case, a large velocity gradient (especially, whirlpool) is formed around a narrow current injector, and thereby, the GVE is expected to give a finite contribution to the nonlocal resistivity.

Finally, we give a comment on the relation between our results and experiments with scanning magnetic microscopy. As mentioned in Sec. 1, modern development of scanning magnetic microscopy has enabled us to visualize an electric Poiseuille flow with high spatial

resolution. Asymmetric Poiseuille flow and anomalous surface current are also detectable through such a scanning technique, by replacing the coefficient $\hat{C}$ to $\hat{M}$. In the recent experiment in WTe_2 [24], which has low symmetry enough to exhibit asymmetric Poiseuille flow, the authors has reported an asymmetric profile of spatial current profile obtained by scanning magnetic microscopy, and they have suggested that the source of this asymmetry is currently unknown. This experimental results might be explained well by our proposals discussed here.

3.4 Symmetry consideration

Here, we provide a symmetry consideration on our hydrodynamic theory for two-dimensional (2D) and three-dimensional (3D) systems. The coefficients $\hat{D}$, $\hat{C}$, and $\hat{F}$ are second rank pseudo-tensors with the same symmetry, and known to become finite in the materials characterized by the so-called natural optical activity [64, 287, 288]. Based on the group theory, in the following, we give the symmetry classification and discuss how we can realize anomalous transport in the existing hydrodynamic materials. The results are summarized in Table 3.1.

(i) For 3D systems: As for the antisymmetric part of $\hat{A}$ (referred to as $\hat{A}^-$), we can represent it in terms of the dual polar vector $a_i \equiv \epsilon_{ijk}A^-_{jk}/2$. This vector is allowed to be finite only in the polar point group $\{C_n, C_{nv}\}$, with $n = 1, 2, 3, 4, 6$, and oriented along the polar axis. With this vector representation, for example, we can rewrite the second term in the bracket of Eq. (3.35) as

$$\hat{F}^- (\boldsymbol{E} \times \boldsymbol{\nabla} T/T) = -\boldsymbol{f} \times (\boldsymbol{E} \times \boldsymbol{\nabla} T/T)\,, \tag{3.49}$$

and the transport current (3.40) as

$$\begin{aligned} \boldsymbol{J}^- = -\frac{e}{\hbar}\,[&m(e\boldsymbol{E} + \boldsymbol{\nabla}\mu) \times (\boldsymbol{d} \times \boldsymbol{u}) + (\boldsymbol{c}(\boldsymbol{\nabla} \cdot \boldsymbol{u}) \\ &-(\boldsymbol{c} \cdot \boldsymbol{\nabla})\boldsymbol{u}) + m(\boldsymbol{\nabla} T/T) \times (\boldsymbol{f} \times \boldsymbol{u})]\,. \end{aligned} \tag{3.50}$$

In particular, the asymmetric Poiseuille flow is realized through this asymmetric contribution. As for the existing hydrodynamic materials, WP_2, which belongs to the polar point group C_{2v} [289], can take a finite value of $\boldsymbol{a}$. On the other hand, the other 3D hydrodynamic materials $PtSn_4$ and MoP are prohibited to have finite $\boldsymbol{a}$, each of which belongs to the point group D_{2h} and D_{3h} [42, 290].

Meanwhile, the symmetric part of $\hat{A}$ is allowed in any chiral groups $\{O, T, C_1, C_n, D_n\}$, with $n = 2, 3, 4, 6$, and specific non-chiral groups $\{C_s, C_{2v}, D_{2d}, S_4\}$, and it induces the anomalous edge current (3.48) in the Poiseuille flow. Especially the scalar component $C \equiv \mathrm{Tr}[\hat{C}]$ contributes to the GVE term in Eq. (3.40) in the form $C\boldsymbol{\omega}$ ($\boldsymbol{\omega} \equiv \boldsymbol{\nabla} \times \boldsymbol{u}$), which causes phenomena similar to the CVE in chiral fluids. However, although such a trace component is allowed to be finite in the chiral point group from a symmetry perspective, we can easily show that C is always zero under our approximation of parabolic dispersion.

(ii) For 2D systems: Next we consider 2D materials including the existing hydrodynamic materials such as mono/bi-layer graphene and GaAs quantum well. In this case, since the Berry curvature behaves as a pseudo-scalar, the coefficients $\hat{A}$ behave as pseudo-vectors constrained in the 2D plane: $A_{ij} = A_i\delta_{jz}$. The symmetry constraints force the vector $\boldsymbol{A}$ to be orthogonal to the mirror lines, and thus, $\boldsymbol{A}$ is allowed only in the crystals with less than two mirror lines in the plane. With this vector representation, we can rewrite the second terms in the bracket of Eq. (3.35) as

$$\hat{F}\,(\boldsymbol{E} \times \boldsymbol{\nabla} T/T) = (\boldsymbol{E} \times \boldsymbol{\nabla} T/T)_z\,\boldsymbol{F}, \tag{3.51}$$

Table 3.1: Symmetry constraints on the candidates for hydrodynamic materials. For comparison, we also refer to some TMD materials. Here, $\boldsymbol{m}$ and $\hat{A}$ represent the vector perpendicular to a mirror plane and either of $\hat{D}$, $\hat{C}$, and $\hat{F}$. The line "operations" denotes the operations needed to make $\hat{A}$ finite. For the symmetry consideration on BL-graphene and ML-MoS_2, implicitly, we also take into account the polar effect of the substrate: $D_{3h} \to C_{3v}$.

Material	point group	components	operations
MoP	D_{3h}	NO	—
WP_2	C_{2v}	A_{xy}, A_{yx}	—
$PdCoO_2$	D_{3d}	NO	—
(110)-GaAs	C_s	$\boldsymbol{A} \parallel \boldsymbol{m}$	—
ML-Graphene	D_{6h}	NO	—
BL-Graphene	$D_{3h} \to C_s$	$\boldsymbol{A} \parallel \boldsymbol{m}$	uniaxial strain
ML-WTe_2	C_s	$\boldsymbol{A} \parallel \boldsymbol{m}$	—
ML-MoS_2	$D_{3h} \to C_s$	$\boldsymbol{A} \parallel \boldsymbol{m}$	uniaxial strain

and the transport current (3.40) as

$$\begin{aligned}\boldsymbol{J} = -en\boldsymbol{u} - \frac{e}{\hbar}\left[m(\boldsymbol{D}\cdot\boldsymbol{u})\cdot(e\boldsymbol{E}+\boldsymbol{\nabla}\mu)\times\hat{\boldsymbol{e}}_z\right.\\ \left.+\boldsymbol{\nabla}\times[(\boldsymbol{C}\cdot\boldsymbol{u})\hat{\boldsymbol{e}}_z] + m(\boldsymbol{F}\cdot\boldsymbol{u})\cdot(\boldsymbol{\nabla}T/T)\times\hat{\boldsymbol{e}}_z\right].\end{aligned} \tag{3.52}$$

As for the existing hydrodynamic materials, GaAs quantum well satisfies the above conditions. In fact, (110)-asymmetric quantum well in GaAs possesses a crystal structure in the point group C_s and it is believed that the circular photogalvanic effect, which is characterized by $\boldsymbol{D}$, has already been observed in the system [281]. On the other hand, $\boldsymbol{A}$ is not allowed in either of ML or BL graphene, both of which have three mirror lines in the plane. However, if we apply a uniaxial strain on the (AB-stacked) BL-graphene, we can realize finite $\boldsymbol{A}$ since the operation reduces the mirror lines from three to one. In fact, very recently, similar strategy has been executed in the system for the observation of QNHE [282]. Moreover, at least from the symmetry viewpoint, monolayer transition metal dichalcogenides (ML-TMDs) could be promising candidates for electron hydrodynamics with finite $\boldsymbol{A}$ (see also the table 3.1).

3.5 Model for quantitative estimation

Finally, let us consider a simple model for strained TMDs or graphene with a staggered sublattice potential [291, 292] to estimate the quantitative behavior of $\boldsymbol{A}$. As is well-known, the Hamiltonian around the valleys K and K' is given by [279]

$$H_\alpha = vp_x\sigma_y - \alpha vp_y\sigma_x + \alpha sp_y\mathbb{1} + \Delta\sigma_z, \tag{3.53}$$

where $\alpha = \pm 1$ denotes the valley index at $\boldsymbol{P}_\pm = \frac{2\pi\hbar}{a}(\pm 2/3, 0)$. Δ is the mass gap and s denotes the strain parameter. This Hamiltonian has a mirror symmetry M_y and thus the hydrodynamic coefficients $\boldsymbol{A}$ must be directed in the y-direction. By diagonalizing the Hamiltonian, we can easily obtain the expression of the energy dispersion $\varepsilon_\alpha(\boldsymbol{p}) = \alpha sp_y + \mathrm{sgn}(\mu)(\Delta^2 + v^2\boldsymbol{p}^2)^{1/2}$ and the Berry curvature

$$\Omega_\alpha = \frac{\mathrm{sgn}(\mu)}{2}\frac{\alpha v^2\hbar^2\Delta}{(\Delta^2+v^2\boldsymbol{p}^2)^{3/2}}, \tag{3.54}$$

where $\mu > 0$ ($\mu < 0$) for the conduction (valence) band. Especially in the low carrier and week strain limit, we can approximate the dispersion with an isotropic parabolic form : $\varepsilon_\alpha(\boldsymbol{p}) \simeq \Delta + (\boldsymbol{p}+\boldsymbol{p}_\alpha)^2/2m + \mathcal{O}(s/v)^2$ where $m = \Delta/v^2$ and $\boldsymbol{p}_\alpha = (0, \alpha s\Delta/v^2)$. As for the Berry curvature dipole $\hat{D}$, the analytical formula at zero temperature has already been obtained in Ref. [279]. On the other hand, the other coefficient $\hat{C}$ can also be easily calculated in the above limit, and finally we obtain the following analytic formula: $c_x = C_{xz} = 0$ and

$$c_y = C_{yz} = \frac{s\Delta^2}{2\pi v^2}\left[\frac{2}{\Delta} - \frac{2\Delta^2 + 3(vp_F)^2}{(\Delta^2 + (vp_F)^2)^{3/2}}\right] + \mathcal{O}(s/v)^2 \tag{3.55}$$

where $p_F = \sqrt{2m|\mu - \Delta|}$ is the radius of the Fermi surface and, when $p_F = 0$, c_y becomes zero. We can estimate a typical scale of c_y for ML-TMDs as 1.9×10^{-28} kg·m/s, using the parameter $v \sim 4.5 \times 10^5$ m/s, $\Delta \simeq 1.5$ eV, $s/v = 0.1$ [279], and $\mu/\Delta = 0.1$, which corresponds to $n \simeq 8 \times 10^{13}$ cm^{-2}. Using these values and $l \sim 1\,\mu$m, we can estimate the anomalous (normalized) current in the asymmetric Poiseuille flow as $J'_y \equiv J_y/E_y\sigma_D = 0.02$ at $x = w/2$ ($w = 10\,\mu$m), which is large enough to detect in experiments.

3.6 Comments on further developments

After the paper [286], which includes the results in this chapter, was published, several researchers have generalized our formulation to the case where the effect of artificial electric fields is taken into consideration [293] and the case under static magnetic field [126] or with spataneous time-reversal breaking [294]. For example, in the case of Ref. [126], our formulas of hydrodynamic variables, such as the momentum flux, are modified by adding correction terms due to external magnetic field B as follows:

$$N = n + \frac{meB}{\hbar}(\boldsymbol{D}+\boldsymbol{N})\cdot\boldsymbol{u} + \mathcal{O}(B^2), \qquad \boldsymbol{P} = mn\boldsymbol{u} + \frac{eB}{\hbar}(\boldsymbol{C}+\boldsymbol{M}), \tag{3.56}$$

$$\boldsymbol{J}^n = n\boldsymbol{u} + \frac{me}{\hbar}(\boldsymbol{D}\cdot\boldsymbol{u} + YB)\cdot(\boldsymbol{E}\times\hat{\mathbf{e}}_z), \tag{3.57}$$

$$\Pi_{ij} = mnu_iu_j + p\delta_{ij} + \frac{e}{\hbar}\epsilon_{jk}E_kC_i + mB\left[(\boldsymbol{M}\cdot\boldsymbol{u})\delta_{ij} + M_iu_j\right] + \mathcal{O}(B^2), \tag{3.58}$$

$$\boldsymbol{F} = -en(\boldsymbol{E}+\boldsymbol{u}\times\boldsymbol{B}), \qquad \boldsymbol{\Gamma} = -mn\boldsymbol{u}/\tau. \tag{3.59}$$

Then, substituting these relations into the continuity equations, we end up with the follwing hydrodynamic equation for noncentrosymmetric electron fluids under external magnetic fields:

Anomalous magnetohydrodynamic equation

$$mn_0\frac{\partial u_i}{\partial t} + mn_0(\boldsymbol{u}\cdot\boldsymbol{\nabla})u_i + \partial_i p + en_0(E_i + \epsilon_{ikl}u_kB_l) + \frac{e}{\hbar}M_{ij}\frac{\partial B_j}{\partial t} + \frac{e}{\hbar}B_k\left[M_{lk}\partial_iu_l + M_{ik}\partial_ju_j + O_{il}\partial_ku_l\right] = -\frac{mn_0u_i}{\tau},$$

where we have neglected the contributions of $\boldsymbol{\nabla}T$ and $\boldsymbol{\nabla}\mu$ for simplicity. Interestingly, this equation can be utilized to describe the nonreciprocal surface plasmon modes and the enhancement of directional dicrhoism due to the resonance of the modes [126].

3.7 Conclusions and outlook of this chapter

Here, we conclude this chapter and provide possible future directions. In this chapter, we have developed a basic framework of electron hydrodynamics in noncentrosymmetric metals, which is composed of a generalized Euler equation (3.35) and the hydrodynamic expression of electric current (3.40). The obtained equation uncovers the analogy between electron fluids in crystals and chiral fluids in vacuum, and predicts various novel transport phenomena beyond linear and local responses. In particular, the generalized vortical effect, which highlights the above analogy, gives rise to unprecedented hydrodynamic transport, that is, the asymmetric Poiseuille flow and the anomalous edge current. We have confirmed that these phenomena can be found in various existing hydrodynamic materials such as WP_2, BL-graphene (under strain) and GaAs quantum well, with local current probes.

Although our formulation is based on the Fermi liquid theory, the obtained hydrodynamic theory itself might be applicable even to the strongly correlated systems beyond quasi-particle picture, since the equation is essentially no more than the continuity equation of electron momentum, which is valid irrespective of the correlation strength. It remains an intriguing problem to study what anomalous or critical behaviors the electron fluids show in noncentrosymmetric hydrodynamic materials beyond the Fermi liquid description.

Moreover, our furmulation in this chapter has based on parabolic approximation for electron's band dispersion. To treat more generic materials including Weyl semimetals more precicely, we need to relax such a condition and improve our formulation to be applicable to any complex band structures. In addition, we have not treated the electron viscosity directly in this work. Viscosity itself is a key ingredient to characterize electron fluids, and thus it would be an interesting problem to clarify how the geometrical structure of Bloch electrons affect the electron viscosity in crystals. These issues seem to be a difficult but challenging problem to be solved in the future.

Chapter 4

Plasmonically-driven geometical photocurrent

In this chapter, we aim to bridge two different research areas, plasmonics and anomalous transport driven by the quantum geometry. For this purpose, we focus on the geometrical photocurrent in two dimensional systems with plasmonic grating gates, and discuss how plasmonic resonances affect these phenomena. As a result, we clarify that the quantum nonlinear Hall effect can be dramatically enhanced over a very broad range of frequency by utilizing plasmonic resonances and near-field effects of grating gates. Especially under the resonant condition, the enhancement becomes several orders of magnitude larger than the case without the nanostructures, while the peaks of high-harmonic plasmons expand broadly and emerge under the off-resonant condition, leading to a remarkably broad spectrum. Furthermore, we clarify a universal relation between the photocurrent induced by the Berry curvature dipole and the optical absorption, which is essential for computational material design of long-wavelength photodetectors. Next we discuss a novel mechanism of geometrical photocurrent, which originates from an anomalous force induced by oscillating magnetic fields and is described by the dipole moment of orbital magnetic moments of Bloch electrons in the momentum space. Our theory is relevant to 2D quantum materials such as layered WTe_2 and twisted bilayer graphene, thereby providing a promising route toward a novel type of highly sensitive, broadband terahertz photodetectors.

In what follows, first we make clear the motivation of this work by overviewing the previous researches in both contexts of plasmonics and quantum geometry (Sec. 4.1). Then, we specify our experimental setup, which we refer to as a periodic plasmonic grating model, and a hydrodynamic flamework to analyze the impact of surface plasmons on the geometrical photocurrent (Sec. 4.2). Next, by solving hydrodynamic equations perturbatively, we obtain the geometrical photocurrent under the resonances of surface plasmons 4.3. In Sec. 4.4 and Sec. 4.6, we exhaustively treat the different two mechanisms of geometrical photocurrent, i.e. the plasmonic quantum nonlinear Hall current and the magnetically-driven plasmonic photocurrent, respectively. Especially, in Sec. 4.5, we show a universal relation between the photocurrent induced by the Berry curvature dipole and the optical absorption rate. Next, in Sec. 4.7, we give a brief comment on the effects of the electron viscosity on the plasmonic photocurrent. Moreover, we specify promising candidates to realize the plasmonic photocurrent obtained in this work (Sec. 4.8). Finally, in Sec. 4.9, we summarize this study with some prospects for future researches.

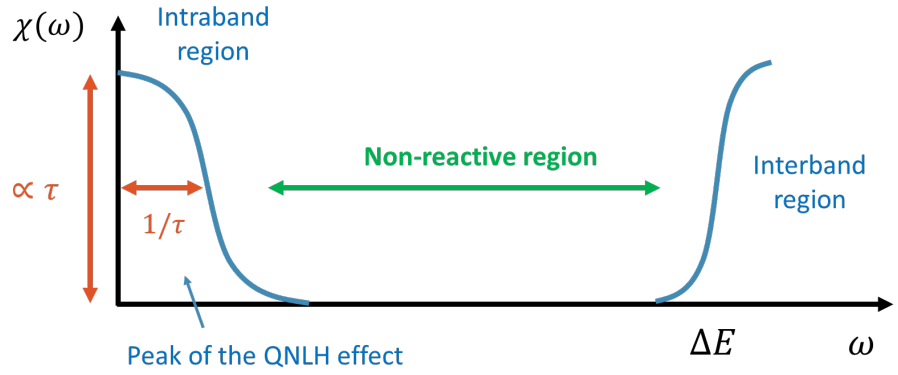

Figure 4.1: Schematic picture of spectrum of quantum nonlinear Hall current or optical absorption. Both of them have a Lorentzian peak at $\omega = 0$ and rapidly decrease over the threshold $1/\tau$. In particular, when we attempt to improve the amplitudes of optical absorption or photocurrent, we have to increase the relaxation time of samples. But, if the relaxation time is improved to be very high, the peak of QNLH effect becomes very sharp, and it cannnot access to THz region. This is the trade-off between the susceptibility and broadbandness of the responses.

4.1 Motivation

In the past decades, quantum geometry plays a crucial role in the linear/nonlinear optical responses of bulk crystals, as exemplified by natural optical activity [127, 128, 129, 130, 131, 132, 133, 134], bulk photovoltaic effect [295, 296, 297, 298, 299], and geometric photon drag [136]. These phenomena provide us with not only a deep insight into the band structure of crystals, but also a variety of functional optical devices, such as solar cells [300, 301] and infrared/terahertz photodetectors [302, 303, 304].

Very recently, Ref. [304] suggests that the QNLH effect has small noise-equivalent power and remarkably high intenal responsivity which is constant over a broad range of frequency. However, since its spectrum has a Lorentzian shape located at $\omega = 0$ with the half width $1/\tau$ and the peak values propprtional to τ, its external responsivity, i.e. its gain per incident power, rapidly decreases as ω^{-2} at frequencies $\omega \gg 1/\tau$ (Fig. 4.1), while the internal responsivity keeps a good value independent on the frequencies. In this way, the QNLH effect invariably suffers from the tradeoff between the bandwidth and the amplitude of the responses. For this reason, to make the QNLH effects work well even at moderately high frequency, we need to give it a twist to improve the external responsivity of the QNLH effect at the frequency over $1/\tau$.

On the other hand, plasmonic nanostructures also provide us with another type of efficient and electrically-tunable optical devices [139, 146, 220, 221, 305]. Such a plasmonic nanodevice achieves its remarkable performance by utilizing the nonlocality and the plasmonic enhancement triggered by the nanostructures. In particular, surface plasmons inherent in two-dimensional (2D) layered systems, such as graphene, are known to have remarkably long lifetimes and electrically-tunable dispersions in the terahertz or mid-infrared region [71, 148, 149]. These properties are ideal for plasmonic devices, and thus a lot of papers have been devoted to investigating the applications such as tunable terahertz photodetectors [29, 97, 102, 143] and broadband absorbers [306, 307, 308].

Notably, as far as we know, these research topics mentioned above, quantum geometry and plasmonics, are usually discussed separately so far, except for several exceptional studies [82, 83, 124, 125, 309]. However, our hydrodynamic formalisms developed in the

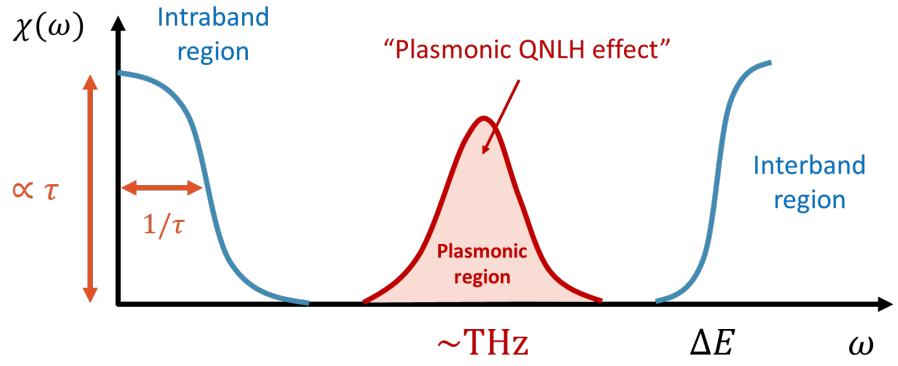

Figure 4.2: Basic idea of the plasmonic QNLH effect. By utilizing surface plasmons with the frequency near the THz regime, we will be able to dramatically enhance the QNLH effect, beyond the threshold of usual intraband responses.

previous chapter give us a powerful tool to investigate an interplay between quantum geometrical effects and surface plasmons through surface plasmonic structures. Actually, as mentioned in Sec. 2, hydrodynamic theory is often used to describe electronic collective modes [81, 82, 83, 84, 85, 86, 87, 88, 89] and nonlocality of optical responses [79, 90, 91, 92, 93, 94, 95, 96, 97, 98, 99, 100, 101, 102, 103, 104, 105]. With these backgrounds, we arrive at the following important questions:

our questions in this chapter

1. How do surface plasmons affect geometrical photocurrent under resonant conditions?
2. Can we improve the QNLH effect beyond the the frequency threshold $1/\tau$ by utilizing the physics of the surface plasmons?
3. Does high internal responsivity of the QNLH effect remain intact even in plasmonic resonances or not?

In this chapter, we tackle these problems based on the anomalous hydrodynamic theory formulated in the previous chapter and Ref. [126]. As a result, we will show that the QNLH effect is enhanced dramatically by plasmonic resonances and near-field effects of grating gates, which is dubbed the *plasmonic QNLH effect* (see also Fig. 4.2). It features multiple sharp peaks near the plasma frequencies, and could be enhanced by several orders of magnitude over a very broad range of frequency. Furthermore, assuming more generic situations, we uncover a universal relation between the photocurrent induced by the Berry curvature dipole and the optical absorption, which is essential for computational material design of long-wavelength photodetectors. Finally we discuss another type of novel geometrical photocurrent, the *magnetically-driven plasmonic photogalvanic effect*. This is a spatially dispersive contribution to the total photocurrent and originates from the anomalous driving force on electron fluids, which is described by the dipole moment of orbital magnetic moments in the momentum space.

4.2 Model

In this section, we will specify our model to describe the interplay between plasmonic resonances and quantum geometrial effects. First, we explain our experimental setup to discuss the plasmonic geometrical photocurrent, which is dubbed periodic plasmonic grating model. It is composed of a back gate to control the plasmon dispersion and a periodic grating gate to enable incident lights to couple with surface plasmons by breaking the macroscopic translational symmetry. Next we introduce anomalous hydrodynamic equations to describe electron dynamics under plasmonic gatings. As mentioned below, the equations can be quite simplified since we are interested only in spatially uniform responses.

4.2.1 Periodic plasmonic grating model

First let us specify our experimetal setup to describe noncentrosymmetric layered systems with plasmonic grating gates (see Fig. 4.3). We assume that the grating gate spatially modulates the normally incident light $\boldsymbol{E}_0(t) = \mathrm{Re}[\tilde{\boldsymbol{E}}_0 e^{i\omega t}]$, leading to the spatially dispersive electric field in 2D electron systems [70, 251]:

$$\boldsymbol{E}_{in}(t,x) = \left[1 + \hat{h}\cos(qx+\phi)\right]\boldsymbol{E}_0(t), \tag{4.1}$$

where the diagonal matrix $\hat{h} = \mathrm{diag}\{h_x, h_y\}$ is a phenomenological parameter to determine the direction of the modulated electric field. Although here we have neglected the high-harmonic modulations [310, 311, 312] for simplicity, we will give a consideration on them in the following. As also noted in Ref. [251], the field amplitude $\tilde{\boldsymbol{E}}$ should be smaller than the amplitude of the incident field due to the screening by the gates in reality. Moreover, in general, the grating parameter $\hat{h}$ strongly depends on frequencies [252, 312]. Nevertheless, we believe that our simplified model captures the key physics of the problem and is sufficient for clarifying the interplay between plasmonic nanostructures and quantum geometrical effects.

Especially when h_y is finite, the Faraday's law results in the presence of an out-of-plane magnetic field,

$$B(t,x) = \frac{qh_y}{\omega}\sin(qx+\phi)\,\mathrm{Re}[-i\tilde{E}_{0y}e^{i\omega t}]. \tag{4.2}$$

Since the grating gate strongly confines the incident light into the x-y plane with a fixed small wavelength, this magnetic field has non-negligible contributions especially in the low frequency limit, leading to a novel mechanism of the photovoltaic effect as discussed below.

When the gate electrode is separated from the channel by an insulator thin film with thickness d and gate-to-channel capacity $C = \varepsilon/4\pi d$, the 2D electron concentration $n(\boldsymbol{r},t)$ is approximately determined by the local gate-to-channel voltage $U(\boldsymbol{r},t)$: $n(\boldsymbol{r},t) = \frac{C}{e}U(\boldsymbol{r},t)$. Such an approximation is often referred to as a gradual channel approximation [57, 314], which is valid for smooth perturbation with $qd \ll 1$. In summary, the total electric field is given by the sum of the incident light $\boldsymbol{E}_{in}$ and the field coming from the density perturbation: $\boldsymbol{E} = \boldsymbol{E}_{in} + (e/C)\boldsymbol{\nabla}n$.

Finally we briefly comment on the role of grating gate to couple incident lights in free space with surface plasmons (see also Fig. 4.4). As also mentioned in Chap. 2, surface plasmons are usually decoupled from free-space lights due to the momentum mismatching, unless the surface has some artificial structure such as the Kretschmann configuration and grating structures [71, 155]. For the case of grating structures discussed above, these nanostructures break the spatial translational symmetry, leading to relaxation of the severe

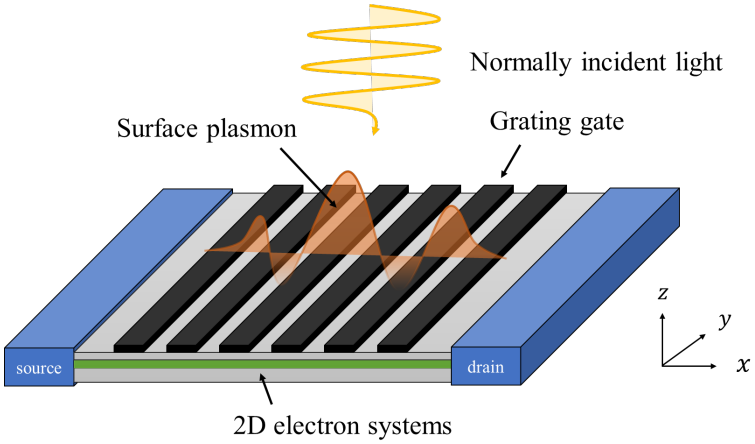

Figure 4.3: Our setup for plasmonically-driven geometrical photocurrent in noncentrosymmetric layerded systems with periodic grating gate [313]. Other types of experimental setups, such as plasmonic cavity or antenna, would be relevant to this work.

conditions for the conservation of photon momentum. More precisely, we can understand that, due to the symmetry reduction from the continuous translational symmetry to the discrete one, the grating gate enables surface plasmons to couple to free space photons with in-plane wavenumber different from that of plasmons by integer multiple of $q = 2\pi/L$, where L is the lattice constant of periodic grating gates:

$$k_{\text{photon}} \equiv k_{\text{plasmon}} \pmod{q}. \tag{4.3}$$

Here k_{photon} and k_{plasmon} are the wavenumbers of photon and surface plasmon respectively. This discussion is quite analogous to the band folding in the Bloch theory. In particular, k_{photon} equals to zero in our paper, since the free-space light is normally incident to the surface. For this reason, excited surface plasmons must have a wavenumber in the form $k_{\text{plasmon}} = mq$ ($m = \pm 1, \pm 2, \cdots$). Actually, this matching condition appears as the multiple peaks in the spectrum of geometrical photocurrent obtained below.

4.2.2 Hydrodynamic equations

Next let us consider the dynamics of electron fluids in noncentrosymmetric crystals with time-reversal symmetry. In this study, we focus on the hydrodynamic regime, where the rate of electron-electron scatterings $1/\tau_e$ exceeds that of other momentum-relaxing scatterings $1/\tau$, and thereby the total electron momentum can be regarded as a long-lived quantity (For details, please see Chap. 1). Under these conditions, the electron dynamics is described by an emergent hydrodynamic theory, whose form crucially depends on the symmetry of the systems.

In general, the continuity equations for electron momentum and particle density are obtained in the relaxation-time approximation as follows [126, 286]:

$$\partial_t N + \boldsymbol{\nabla} \cdot \boldsymbol{J}^n = 0, \tag{4.4}$$
$$\partial_t P_i + \partial_j \Pi_{ij} = F_i + \Gamma_i, \tag{4.5}$$

where N and P_i are respectively the density of electron momentum and particle number, $\boldsymbol{J}$ and Π_{ij} are the flux of them, $\boldsymbol{F}$ is the external force due to the applied electromagnetic fields, $\boldsymbol{\Gamma}$ is the disipative force due to the momentum relaxing scatterings. As mentioned briefly in the previous chapter, Ref. [126] has formulated an anomalous hydrodynamic

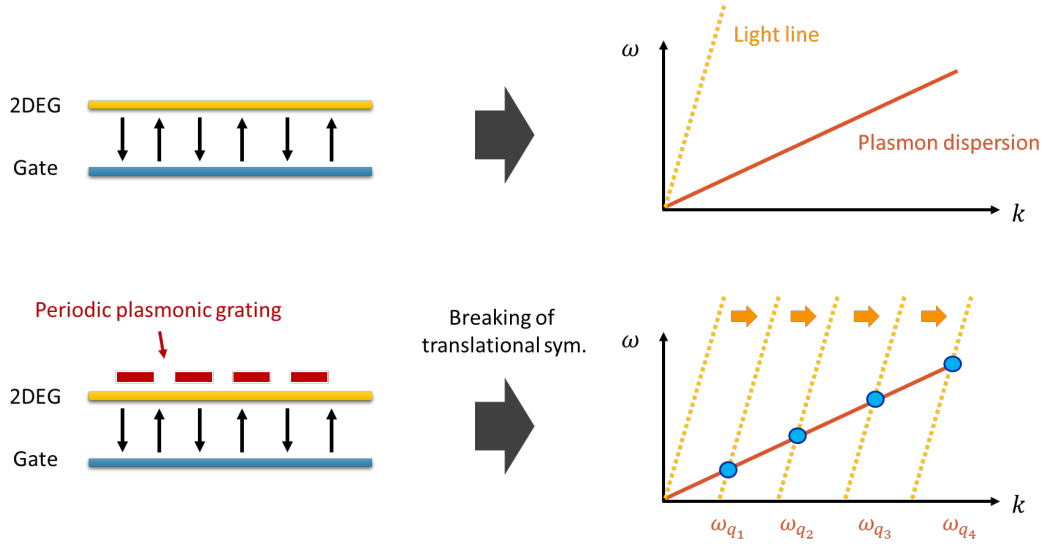

Figure 4.4: Schematic pictures of plasmon's dispersions with and without periodic plasmonic grating gate. Surface plasmons without external decorations are usually decoupled from free-space lights due to the momentum mismatching. On the other hand, by implementing periodic grating gate on the 2DEG, surface plasmons can couple to free-space photons with in-plane wavenumber different from that of plasmons by integer multiple of $q = 2\pi/L$.

theory for 2D noncentrosymmetric electron fluids with parabolic dispersion near some valleys, taking the effects of magnetic fields into account. According to the paper, the above quantities appearing in the continuity equations can be described with some hydrodynamic variables, such as velocity fields $\boldsymbol{u}$, as

$$\begin{aligned} N &= n + \frac{meB}{\hbar}(\boldsymbol{D}+\boldsymbol{N})\cdot\boldsymbol{u} + \mathcal{O}(B^2), \qquad \boldsymbol{P} = mn\boldsymbol{u} + \frac{eB}{\hbar}(\boldsymbol{C}+\boldsymbol{M}), \\ \boldsymbol{J}^n &= n\boldsymbol{u} + \frac{me}{\hbar}(\boldsymbol{D}\cdot\boldsymbol{u} + YB)\cdot(\boldsymbol{E}\times\hat{\mathbf{e}}_z), \\ \Pi_{ij} &= mnu_iu_j + p\delta_{ij} + \frac{e}{\hbar}\epsilon_{jk}E_kC_i + mB\left[(\boldsymbol{M}\cdot\boldsymbol{u})\delta_{ij} + M_iu_j\right] + \mathcal{O}(B^2), \\ \boldsymbol{F} &= -en(\boldsymbol{E}+\boldsymbol{u}\times\boldsymbol{B}), \qquad \boldsymbol{\Gamma} = -mn\boldsymbol{u}/\tau, \end{aligned} \tag{4.6}$$

where $\boldsymbol{E}$ is an applied in-plane electric field, $\boldsymbol{B} = (0,0,B)$ is an applied out-of-plane magnetic field, n is the particle density without the correction due to magnetic fields. $\boldsymbol{C}$, $\boldsymbol{D}$, $\boldsymbol{M}$, and $\boldsymbol{N}$ are the geometrical pseudovectors originating from the Berry curvature Ω_z^α or the magnetic moment of the Bloch wavepackets m_z^α, which are defined as follows respectively [1]:

$$\boldsymbol{C} = \sum_\alpha \int [d\boldsymbol{p}]\boldsymbol{p}\Omega_{\alpha,z}f_{0\alpha}, \qquad \boldsymbol{D} = \sum_\alpha \int [d\boldsymbol{p}]\frac{\partial\Omega_{\alpha,z}}{\partial\boldsymbol{p}}f_{0\alpha}, \tag{4.7}$$

$$\boldsymbol{M} = \sum_\alpha \int [d\boldsymbol{p}]\frac{\partial m_z^\alpha}{\partial\boldsymbol{p}}f_{0\alpha}, \qquad \boldsymbol{N} = -\frac{\hbar}{e}\sum_\alpha \int [d\boldsymbol{p}]\frac{\partial m_z^\alpha}{\partial\boldsymbol{p}}\frac{\partial f_{0\alpha}}{\partial\epsilon}, \tag{4.8}$$

where α is a valley index, $f_{0\alpha} = [1 + e^{-\beta(\varepsilon_\alpha(\boldsymbol{p})-\mu)}]^{-1}$ is the Fermi distribution function at the valley α, and we have introduced the notation $\int[d\boldsymbol{p}] \equiv \int d\boldsymbol{p}/(2\pi\hbar)^d$. In particular, the geometrical coefficient $\boldsymbol{D}$ is called as the so-called Berry curvature dipole (BCD) in

[1] Our definition of $\boldsymbol{M}$ is defferent from the one in Ref. [126] by a constant factor $m\hbar/e$.

previous literatures [279]. Here we note that Eqs (4.6) are correct up to the second order of the external perturbations, and $\mathcal{O}(B^2)$ terms in n and Π_{ij} are not explicitly shown in Eq. (4.6), since they never contribute to the results in this work. For example, in the analysis of the photocurrent, they always appear in the form of the time or spatial derivative, $\partial_{t,x}(O(B^2))$, and thus do not contribute to the spatially and temporally uniform currents. For the same reason, we do not need to consider the terms in the form $\partial_{t,x}(O(E^2, BE, B^2))$ in the following analyses. Furthermore, we note that, although geometrical pseudovectors, such as $\boldsymbol{C}$ and $\boldsymbol{D}$, depend on time t and spatial position $\boldsymbol{r}$ through chemical potential $\mu(t, \boldsymbol{r})$ or temperature $T(t, \boldsymbol{r})$, we can neglect higher-order corrections due to this dependence for the above reason.

Combining Eqs. (4.4) - (4.6), we obtain the following hydrodynamic equations for noncentrosymmetric electron fluids with parabolic dispersion:

Hydrodynamic equations for noncentrosymmetric metals

$$\begin{aligned} \frac{\partial \boldsymbol{u}}{\partial t} + (\boldsymbol{u}\cdot\boldsymbol{\nabla})\boldsymbol{u} + \frac{\boldsymbol{\nabla} P}{mn} + \frac{e}{m}(\boldsymbol{E} + \boldsymbol{u}\times\boldsymbol{B}) + \frac{\boldsymbol{M}}{n}\left(\frac{\partial B}{\partial t}\right) + \cdots = -\frac{\boldsymbol{u}}{\tau}, \\ \frac{\partial n}{\partial t} + \boldsymbol{\nabla}\cdot(n\boldsymbol{u}) + \cdots = 0, \end{aligned} \tag{4.9}$$

where "$\cdots$" denotes the negligible terms in the form $\partial_{t,x}(O(E^2, BE, B^2))$. The last term on the left-hand side is first derived in Ref [126], and represents a geometrical anomalous force due to oscillating magnetic fields, which is closely related with the so-called gyrotropic magnetic effect [130, 132, 133, 134].

Especially in our periodic plasmonic grating model, the 2D electron concentration $n(\boldsymbol{r}, t)$ is determined by the local gate-to-channel voltage $U(\boldsymbol{r}, t)$, and the total electric field is described as $\boldsymbol{E} = \boldsymbol{E}_{in} + (e/C)\boldsymbol{\nabla} n$. Therefore, Eqs. (4.9) can be rewritten in a more explicit form:

$$\begin{aligned} \frac{\partial \boldsymbol{u}}{\partial t} + (\boldsymbol{u}\cdot\boldsymbol{\nabla})\boldsymbol{u} + \frac{e}{m}(\boldsymbol{E}_{in} + \boldsymbol{u}\times\boldsymbol{B}) \\ + \frac{s^2}{n_0}\boldsymbol{\nabla}\delta n + \frac{\boldsymbol{M}}{n_0}\left(1 - \frac{\delta n}{n_0}\right)\left(\frac{\partial B}{\partial t}\right) + \cdots = -\frac{\boldsymbol{u}}{\tau}, \end{aligned} \tag{4.10}$$

$$\frac{\partial \delta n}{\partial t} + n_0 \boldsymbol{\nabla}\boldsymbol{u} + \cdots = 0, \tag{4.11}$$

where $s = \sqrt{n_0(e^2/mC + n_v/m\nu)}$ is the group velocity of the plasmon, $\nu = m/2\pi\hbar^2$ is the density of states per valley, n_v is the number of valleys, n_0 is the uniform particle density without perturbations, and then we introduced the notation $\delta n \equiv n - n_0$. In the derivation, we have used the formula $P \simeq n_v n^2/2\nu + n_v \nu T^2\pi^2/6$ in the 2D degenerate electrons with parabolic dispersion and neglect the thermoelectrical force $F_{th} \propto \boldsymbol{\nabla} T^2$ since it can be estimated as $F_{th} \propto \boldsymbol{\nabla}\boldsymbol{u}^2 \propto \partial_{t,x}(O(E^2, BE, B^2))$ discussed in Ref. [251].

Here it is notable that the velocity field itself is not an observable quantity, as in the case of the previous chapter. According to the Ref. [126], we have to relate the velocity field $\boldsymbol{u}$ with the observable electric current by using the following formula:

Relation between electric currents and velocity fields under electromagnetic fields

$$\boldsymbol{j} = -en\boldsymbol{u} - \frac{me^2}{\hbar}(\boldsymbol{D}\cdot\boldsymbol{u} + YB)\cdot(\boldsymbol{E}\times\hat{\mathbf{e}}_z) + \cdots, \tag{4.12}$$

where Y is a geometrical scalar coefficient, defined as

$$Y = \sum_{\alpha} Y^{\alpha}, \quad Y^{\alpha} = -\frac{1}{m}\int [d\boldsymbol{p}]\Omega_z^{\alpha} m_z^{\alpha} \partial_{\epsilon} f_0(\epsilon_0). \tag{4.13}$$

The first term in Eq. (4.12) is a familiar part known in conventional hydrodynamic theory, and the others are geometrical contributions due to the symmetry lowering of the fluids. In particular, the term proportional to the coefficient $\boldsymbol{D}$ describes the contribution of the so-called quantum nonlinear Hall (QNLH) effect [279, 286]. Here, we note that "$\cdots$" in Eq. (4.12) denotes the rotational currents, which cause several remarkable phenomena such as voriticity-induced anomalous currents [286], but does not contribute to the analysis in this work since rotational components never contribute to spatially uniform currents. We can calculate the electric current density $\boldsymbol{j}(x,t)$ by solving the above hydrodynamic equations under external fields, and substituting the obtained solution $\boldsymbol{u}(x,t)$ and $n(x,t)$ to the above hydrodynamic formula of eletctric current. Most important is that crystal symmetry imposes strong restrictions on the geometical pseudovectors $\boldsymbol{M}$ and $\boldsymbol{D}$, and thus we have to break any rotational symmetry and reduce the number of mirror lines to be less than two for these vectors to be finite.

4.3 Derivation of plasmonically-enhanced photocurrent

In the following, we perform a perturbative calculation to analyze plasmonically-enhanced photocurrents in noncetrosymmetric electron fluids. For this purpose, we perturbatively expand the velocity field $\boldsymbol{u}$, particle density n, and the total electric field $\boldsymbol{E}$ with respect to $\tilde{\boldsymbol{E}}_0$ as follows:

$$\begin{aligned} &\boldsymbol{u} = \boldsymbol{u}_1 + \boldsymbol{u}_2 + \cdots, \qquad n = n_0 + \delta n = n_0 + \delta n_1 + \delta n_2 + \cdots, \\ &\boldsymbol{E} = \boldsymbol{E}_1 + \boldsymbol{E}_2 + \cdots, \qquad B = B_1. \end{aligned} \tag{4.14}$$

With these notations, from Eq. (4.12), the leading photocurrent can be written as a sum of several contributions:

$$\boldsymbol{j}_{DC} = -e\left\langle \delta n_1 \boldsymbol{u}_1 + n_0 \boldsymbol{u}_2 \right\rangle_{t,x} - \frac{me^2}{\hbar}\left\langle (\boldsymbol{D}\cdot\boldsymbol{u}_1 + YB_1)\cdot(\boldsymbol{E}_1 \times \hat{\mathbf{e}}_z)\right\rangle_{t,x}, \tag{4.15}$$

where $\langle\cdots\rangle_{t,x}$ denotes the time and space averaging over the periods.

The first order contributions can be easily calculated from Eq (4.10) and we obtain

$$\begin{aligned} u_{1,x} &= \mathrm{Re}\left[\frac{e^{i\omega t}}{\omega^2 - \omega_q^2 - i\omega/\tau}\left(\frac{ie\omega}{m}(h_x\tilde{E}_{0x})\cos(qx+\phi)\right.\right. \\ &\qquad \left.\left. + \frac{i\omega q}{n_0}(h_y\tilde{E}_{0y})M_x\sin(qx+\phi)\right) - \frac{e}{m}\frac{e^{i\omega t}}{i\omega + 1/\tau}\tilde{E}_{0x}\right], \\ u_{1,y} &= \mathrm{Re}\left[-\frac{e^{i\omega t}}{i\omega + 1/\tau}\left(\frac{e}{m}(h_y\tilde{E}_{0y})\cos(qx+\phi)\right.\right. \\ &\qquad \left.\left. + \frac{q}{n_0}(h_y\tilde{E}_{0y})M_y\sin(qx+\phi)\right) - \frac{e}{m}\frac{e^{i\omega t}}{i\omega + 1/\tau}\tilde{E}_{0y}\right], \\ \delta n_1 &= \mathrm{Re}\left[\frac{e^{i\omega t}}{\omega^2 - \omega_q^2 - i\omega/\tau}\left(\frac{en_0 q}{m}(h_x\tilde{E}_{0x})\sin(qx+\phi) - (h_y\tilde{E}_{0y}q^2)M_x\cos(qx+\phi)\right)\right]. \end{aligned} \tag{4.16}$$

These results mean that the spatial modulation by the grating gate ($\boldsymbol{h} \neq 0$) causes a plasmonic resonance denoted by the prefactor $(\omega^2 - \omega_q^2 - i\omega/\tau)^{-1}$, whose imaginary part

has a strong peak with the half width $1/\tau$ near the plasmon frequency $\omega \sim \omega_q$ under the resonant condition.

Next let us consider the contributions in the second order of perturbations. From Eq. (4.10), the second order term of the velocity fields $\boldsymbol{u}_2$ satisfies

$$\frac{\partial \boldsymbol{u}_2}{\partial t} + (\boldsymbol{u}_1 \cdot \boldsymbol{\nabla})\boldsymbol{u}_1 + \frac{e}{m}(\boldsymbol{u}_1 \times \boldsymbol{B}_1) + \frac{s^2}{n_0}\boldsymbol{\nabla}\delta n_2 + \frac{\boldsymbol{M}}{n_0}\left(\frac{\delta n_1}{n_0}\right)\left(\frac{\partial B_1}{\partial t}\right) + \cdots = -\frac{\boldsymbol{u}_2}{\tau}. \quad (4.17)$$

Focusing on the time and space average of the velocity fields $\boldsymbol{u}_2$, this equation leads to the relation

$$\langle \boldsymbol{u}_2 \rangle_{t,x} = -\tau \left\langle (\boldsymbol{u}_1 \cdot \boldsymbol{\nabla})\boldsymbol{u}_1 + \frac{e}{m}(\boldsymbol{u}_1 \times \boldsymbol{B}_1) + \frac{\boldsymbol{M}}{n_0}\left(\frac{\delta n_1}{n_0}\right)\left(\frac{\partial B_1}{\partial t}\right) \right\rangle_{t,x}, \quad (4.18)$$

and each term can be calculated as follows:

$$\begin{aligned}
\langle (\boldsymbol{u}_1 \cdot \boldsymbol{\nabla})\boldsymbol{u}_1 \rangle_{t,x} &= \frac{eq^2}{4mn_0}\frac{\omega^2 h_x h_y}{(\omega^2 - \omega_q^2)^2 + (\omega/\tau)^2}\,\mathrm{Re}\left[E_{0x}E_{0y}^*\right](M_x \hat{\boldsymbol{e}}_x) \\
&\quad + \frac{eq^2}{4mn_0}\,\mathrm{Re}\left[\frac{i\omega}{(\omega^2 - \omega_q^2 - i\omega/\tau)(i\omega - 1/\tau)}\right. \\
&\quad \left. \times ((h_x\tilde{E}_{0x})(h_y\tilde{E}_{0y}^*)M_y + |h_y\tilde{E}_{0y}|^2 M_x)\right]\hat{\boldsymbol{e}}_y, \\
\left\langle \frac{e}{m}(\boldsymbol{u}_1 \times \boldsymbol{B}_1) \right\rangle_{t,x} &= \frac{eq^2}{4mn_0}\,\mathrm{Re}\left[\frac{1}{\omega^2 - \omega_q^2 - i\omega/\tau}|h_y\tilde{E}_{0y}|^2\right] M_x \hat{\boldsymbol{e}}_y \\
&\quad - \frac{eq^2}{4mn_0}\,\mathrm{Re}\left[\frac{1}{\omega^2 - i\omega/\tau}|h_y\tilde{E}_{0y}|^2\right] M_y \hat{\boldsymbol{e}}_x \\
\left\langle \frac{\boldsymbol{M}}{n_0}\left(\frac{\delta n_1}{n_0}\right)\left(\frac{\partial B_1}{\partial t}\right) \right\rangle_{t,x} &= \frac{eq^2}{4mn_0}\,\mathrm{Re}\left[\frac{1}{\omega^2 - \omega_q^2 - i\omega/\tau}(h_x\tilde{E}_{0x})(h_y\tilde{E}_{0y}^*)\boldsymbol{M}\right],
\end{aligned} \quad (4.19)$$

where $\hat{\mathbf{e}}_i$ is a unit vector in the direction of i-axis.

Substituting these results into Eq. (4.15), we obtain the total photocurrent $\boldsymbol{j}_{DC}$ as the sum of the contributions arising from different mechanisms as follows:

$$\boldsymbol{j}_{DC} = \boldsymbol{j}_{DC}^{BCD} + \boldsymbol{j}_{DC}^{MPP}, \quad (4.20)$$

where $\boldsymbol{j}_{DC}^{BCD}$ is the BCD-induced photocurrent,

$$\begin{aligned}
\boldsymbol{j}_{DC}^{BCD} &= \frac{e^3}{2\hbar}\,\mathrm{Re}\left[\frac{1}{i\omega + 1/\tau}(\boldsymbol{D} \cdot \tilde{\boldsymbol{E}}_0) \cdot (\tilde{\boldsymbol{E}}_0^* \times \hat{\mathbf{e}}_z)\right. \\
&\quad \left. + \frac{1}{2}\left(-\frac{i\omega}{\omega^2 - \omega_q^2 - i\omega/\tau}D_x h_x \tilde{E}_{0x} + \frac{1}{i\omega + 1/\tau}D_y h_y \tilde{E}_{0y}\right)(\hat{h}\tilde{\boldsymbol{E}}_0^* \times \hat{\mathbf{e}}_z)\right] \\
&\quad - \frac{e^5 n_0 q^2}{4\hbar m C}\,\mathrm{Re}\left[\frac{1}{(i\omega + 1/\tau)(\omega^2 - \omega_q^2 + i\omega/\tau)}\right. \\
&\quad \left. \times \left((h_y\tilde{E}_{0y})(h_x\tilde{E}_{0x}^*) + \left(\frac{mq}{en_0}\right)^2 M_y |h_y\tilde{E}_{0y}|^2\right)\right](D_y \hat{\mathbf{e}}_y).
\end{aligned} \quad (4.21)$$

On the other hand, $\boldsymbol{j}_{DC}^{MPP}$ is a magnetically-driven plasmonic photocurrent, which is proportional to the geometirical pseudovector $\boldsymbol{M}$, and obtained as the sum of contributions of several nolinear terms in the hydrodynamic equations or anomalous currents proportional to the geometrical scalar Y,

$$\boldsymbol{j}_{DC}^{MPP} = \boldsymbol{j}_{DC}^{density} + \boldsymbol{j}_{DC}^{inertia} + \boldsymbol{j}_{DC}^{Lorentz} + + \boldsymbol{j}_{DC}^{Y}, \quad (4.22)$$

where

$$\begin{aligned}\boldsymbol{j}_{DC}^{density} = &\frac{e^2q^2}{4m}\,\mathrm{Re}\left[\frac{\tau}{\omega^2-\omega_q^2-i\omega/\tau}(h_x\tilde{E}_{0x})(h_y\tilde{E}_{0y}^*)\boldsymbol{M}\right]\\ &+\frac{e^2q^2}{4m}\frac{\omega}{(\omega^2-\omega_q^2)^2+(\omega/\tau)^2}\,\mathrm{Re}\left[i(h_x\tilde{E}_{0x})(h_y\tilde{E}_{0y}^*)-i(h_y\tilde{E}_{0y})(h_x\tilde{E}_{0x}^*)\right](M_x\hat{\mathbf{e}}_x)\\ &+\frac{e^2q^2}{4m}\,\mathrm{Re}\left[\frac{i}{(i\omega-1/\tau)(\omega^2-\omega_q^2-i\omega/\tau)}\left(|h_y\tilde{E}_{0y}|^2M_x-(h_y\tilde{E}_{0x})(h_x\tilde{E}_{0y}^*)M_y\right)\right]\hat{\mathbf{e}}_y,\end{aligned} \tag{4.23}$$

$$\begin{aligned}\boldsymbol{j}_{DC}^{inertia} = &\frac{e^2q^2}{4m}\frac{\tau\omega^2h_xh_y}{(\omega^2-\omega_q^2)^2+(\omega/\tau)^2}\,\mathrm{Re}\left[E_{0x}E_{0y}^*\right](M_x\hat{\boldsymbol{e}}_x)\\ &+\frac{e^2q^2}{4m}\,\mathrm{Re}\left[\frac{i\omega\tau}{(i\omega-1/\tau)(\omega^2-\omega_q^2-i\omega/\tau)}((h_x\tilde{E}_{0x})(h_y\tilde{E}_{0y}^*)M_y+|h_y\tilde{E}_{0y}|^2M_x)\right]\hat{\boldsymbol{e}}_y,\end{aligned} \tag{4.24}$$

$$\begin{aligned}\boldsymbol{j}_{DC}^{Lorentz} = &\frac{e^2q^2}{4m}\,\mathrm{Re}\left[\frac{\tau}{\omega^2-\omega_q^2-i\omega/\tau}|h_y\tilde{E}_{0y}|^2\right]M_x\hat{\boldsymbol{e}}_y\\ &-\frac{e^2q^2}{4m}\,\mathrm{Re}\left[\frac{\tau}{\omega^2-i\omega/\tau}|h_y\tilde{E}_{0y}|^2\right]M_y\hat{\boldsymbol{e}}_x,\end{aligned} \tag{4.25}$$

$$\boldsymbol{j}_{DC}^{Y} = \frac{me^3q^4Y}{4\hbar C}\,\mathrm{Re}\left[\frac{i/\omega}{\omega^2-\omega_q^2+i\omega/\tau}M_x|h_y\tilde{E}_{0y}|^2\hat{\mathbf{e}}_x\right]. \tag{4.26}$$

Here $\boldsymbol{j}_{DC}^{density}$ is the photocurrent related with the first order spatial modulation of particle density δn_1, $\boldsymbol{j}_{DC}^{inertia}$ is the one arising from the inertia term $(\boldsymbol{u}\cdot\boldsymbol{\nabla})\boldsymbol{u}$, $\boldsymbol{j}_{DC}^{Lorentz}$ is the one arising from the Lorentz force term, $\boldsymbol{j}_{DC}^{Y}$ is the one related with the geometrical scalar coefficient Y. Although these formulas have quite complicated forms, we have easily found that each geometrical photocurrent is strongly enhanced near the plasmonic frequency $\omega=\omega_q$. In the following sections, we will give more detailed analyses of $\boldsymbol{j}_{DC}^{BCD}$ and $\boldsymbol{j}_{DC}^{MPP}$ respectively. Especially for the term $\boldsymbol{j}_{DC}^{BCD}$, we will show its universal relation with the optical absorption.

By introducing the notation

$$\tilde{E}_{0i}\tilde{E}_{0j}^* = \mathrm{Re}\left[\tilde{E}_{0i}\tilde{E}_{0j}^*\right]+i\,\mathrm{Im}\left[\tilde{E}_{0i}\tilde{E}_{0j}^*\right] = \mathcal{L}_{ij}-i\epsilon_{ijk}\mathcal{F}_k, \tag{4.27}$$

we can describe the polarization dependence of each term more clearly. Here we have defined $\mathcal{L}_{ij}=\mathrm{Re}\left[\tilde{E}_{0i}\tilde{E}_{0j}^*\right]$ and $\boldsymbol{\mathcal{F}}=\frac{i}{2}\tilde{\boldsymbol{E}}\times\tilde{\boldsymbol{E}}^*$, each of which represents the contribution of linearly-polarized light and circularly-polarized light respectively [299]. In particular, the trace of $\mathcal{L}_{ij}$, denoted as $\mathcal{I}=\frac{1}{2}\sum_i\mathcal{L}_{ii}$, is proportional to the intensity of an incident light. For example, when the incident light is a linearly-polarized light, such as $\tilde{\boldsymbol{E}}_0=\tilde{E}_0(1,\pm1,0)$, these indicators satisfy $\mathcal{I}=|\tilde{E}_0|^2$, $\mathcal{L}_{xy}=\pm|\tilde{E}_0|^2$ and $\boldsymbol{\mathcal{F}}=0$. On the other hand, when the incident light is a circularly-polarized light, i.e., $\tilde{\boldsymbol{E}}_0=\tilde{E}_0(1,\pm i,0)$, these indicators satisfy $\mathcal{I}=|\tilde{E}_0|^2$, $\mathcal{L}_{ij}=0$ and $\boldsymbol{\mathcal{F}}=\pm|\tilde{E}_0|^2\hat{\boldsymbol{e}}_z$. Using these notations, we can rewrite the above results as

$$
\begin{aligned}
j_{DC,i}^{BCD} = \frac{e^3}{2\hbar}\Bigg[& \frac{\tau}{1+(\omega\tau)^2}\sum_j\left(1+\frac{\omega^2(1+(\omega\tau)^2)h_x h_j}{2\tau^2[(\omega^2-\omega_q^2)^2+(\omega/\tau)^2]}\right)\epsilon_{ij}D_x L_{xj} \\
& + \frac{\tau}{1+(\omega\tau)^2}\sum_j(1+h_y h_j)\epsilon_{ij}D_y L_{yj} \\
& + \frac{\omega\tau^2}{1+(\omega\tau)^2}\left(1-\frac{\omega(\omega^2-\omega_q^2)(1+(\omega\tau)^2)h_x h_y}{2\tau[(\omega^2-\omega_q^2)^2+(\omega/\tau)^2]}\right)\mathcal{F}_z D_x\delta_{ix} \\
& + \frac{\omega\tau^2}{1+(\omega\tau)^2}(1+h_x h_y)\mathcal{F}_z D_y\delta_{iy}\Bigg] \\
+ \frac{e^5 n_0 q^2}{4\hbar m C}\frac{1}{(1+(\omega\tau)^2)((\omega^2-\omega_q^2)^2+(\omega/\tau)^2)}\Bigg[& \tau\omega_q^2 h_x h_y\mathcal{L}_{xy} \\
& - \omega(1+\tau^2(\omega^2-\omega_q^2))h_x h_y\mathcal{F}_z + \tau\omega_q^2\left(\frac{mq}{en_0}\right)^2 M_y h_y^2\mathcal{L}_{yy}\Bigg] D_y\delta iy,
\end{aligned}
\tag{4.28}
$$

$$
\begin{aligned}
\boldsymbol{j}_{DC}^{density} = & \frac{e^2q^2}{4m}\left[\frac{\tau(\omega^2-\omega_q^2)h_x h_y}{(\omega^2-\omega_q^2)^2+(\omega/\tau)^2}\mathcal{L}_{xy}+\frac{\omega h_x h_y}{(\omega^2-\omega_q^2)^2+(\omega/\tau)^2}\mathcal{F}_z\right]\boldsymbol{M} \\
& + \frac{e^2q^2}{2m}\frac{\omega h_x h_y}{(\omega^2-\omega_q^2)^2+(\omega/\tau)^2}\mathcal{F}_z M_x\hat{\mathbf{e}}_x \\
& + \frac{e^2q^2}{4m}\frac{1}{(1+(\omega\tau)^2)((\omega^2-\omega_q^2)^2+(\omega/\tau)^2)} \\
& \times\left[\omega(1+\tau^2(\omega^2-\omega_q^2))(h_y^2\mathcal{L}_{yy}M_x - h_x h_y\mathcal{L}_{xy}M_y)-\tau\omega_q^2 h_x h_y\mathcal{F}_z M_x\right]\hat{\mathbf{e}}_y,
\end{aligned}
\tag{4.29}
$$

$$
\begin{aligned}
\boldsymbol{j}_{DC}^{inertia} = & \frac{e^2q^2}{4m}\frac{\omega^2\tau h_x h_y}{(\omega^2-\omega_q^2)^2+(\omega/\tau)^2}\mathcal{L}_{xy}M_x\hat{\mathbf{e}}_x \\
& + \frac{e^2q^2}{4m}\frac{\omega\tau}{(1+(\omega\tau)^2)((\omega^2-\omega_q^2)^2+(\omega/\tau)^2)} \\
& \times\left[\omega(1+\tau^2(\omega^2-\omega_q^2))(h_y^2\mathcal{L}_{yy}M_x + h_x h_y\mathcal{L}_{xy}M_y)+\tau\omega_q^2 h_x h_y\mathcal{F}_z M_y\right]\hat{\mathbf{e}}_y,
\end{aligned}
\tag{4.30}
$$

$$
\boldsymbol{j}_{DC}^{Lorentz} = \frac{e^2q^2}{4m}\frac{\tau(\omega^2-\omega_q^2)h_y^2}{(\omega^2-\omega_q^2)^2+(\omega/\tau)^2}\mathcal{L}_{yy}M_x\hat{\boldsymbol{e}}_y - \frac{e^2q^2}{4m}\frac{\tau^3 h_y^2}{1+(\omega\tau)^2}\mathcal{L}_{yy}M_y\hat{\boldsymbol{e}}_x,
\tag{4.31}
$$

$$
\boldsymbol{j}_{DC}^{Y} = \frac{me^3q^4Y}{4\hbar C}\frac{1/\tau}{(\omega^2-\omega_q^2)^2+(\omega/\tau)^2}\mathcal{L}_{yy}M_x\hat{\mathbf{e}}_x.
\tag{4.32}
$$

4.4 Plasmonic quantum nonlinear Hall effect

In what follows, we will answer the question raised in Sec. 4.1, i.e., to what extent the plasmonic resonces improve the susceptivility of the QNLH effect in the frequency regime

over the threshold $1/\tau$. Here, for simplicity, let us consider x-polarized incident light $\tilde{\boldsymbol{E}}_0 = (\tilde{E}_{0x}, 0, 0)$. In this case, by substituting $\mathcal{L}_{xx} = |\tilde{E}_{0x}|^2$ and $\mathcal{L}_{xy} = \mathcal{L}_{yy} = \mathcal{F}_z = 0$ into Eqs. (4.28) - (4.32), we find that the total photocurrent is exactly attributed only to the contribution of the QNLH term $\boldsymbol{j}_{DC}^{BCD}$ and it is described by a simple beautiful form as follows:

Plasmonic QNLH current under x-polarized light

$$\boldsymbol{j}_{DC} = \boldsymbol{j}_{DC}^{BCD} = -\frac{e^3}{2\hbar}\frac{\tau\beta_\omega}{1+(\omega\tau)^2} D_x |\tilde{E}_{0x}|^2 \hat{\boldsymbol{e}}_y, \tag{4.33}$$

where $\hat{\boldsymbol{e}}_y$ is a unit vector in the y-direction, β_ω is an amplification factor due to the plasmonic resonance,

Amplification factor in plasmonic QNLH effect

$$\beta_\omega = 1 + \frac{\tilde{\omega}^2(1+\tilde{\tau}^2\tilde{\omega}^2)h_x^2}{2[\tilde{\tau}^2(\tilde{\omega}^2-1)^2+\tilde{\omega}^2]}, \tag{4.34}$$

and we have introduced two dimensionless paramters: $\tilde{\tau} = \omega_q\tau$ and $\tilde{\omega} = \omega/\omega_q$. Here ω_q is the plasmon frequency $\omega_q = sq$, and s is the group velocity of the plasmon. This is one of our main results in this work, and we refer to it as the *plasmonic QNLH effect*. In Fig. 4.5 (a), we have plotted the spectrum of β_ω for various values of $\tilde{\tau}$.

In the low-frequency limit ($\tilde{\omega} \to 0$), the amplification factor β_ω approaches one and Eq. (4.33) becomes equivalent to that in Ref. [279], which means that the original peak of the QNLH effect at $\omega = 0$ remains intact regardless of the existence of the grating gate. On the other hand, at the plasmon frequency $\omega = \omega_q$, it features another sharp peak with a width $\Delta\omega \sim 1/\tau$ in the resonant regime ($\tilde{\tau} \gg 1$), and the amplitude of the QNLH current is strongly enhanced by the dimensionless factor $|\beta_{\omega_q}| \sim |h_x\tilde{\tau}|^2/2$, compared to the case without grating gate. In particular, by utilizing near-field enhancement of gold grating gates, it is possible for the grating factor h_x to be compareble to or much larger than one ($h_x \gg 1$) [252, 312, 315]. This means that the QNLH current could be enhanced by several orders of magnitude under the resonant condition ($\tilde{\tau} \gg 1$).

In the discussion so far, we have focused on a specific harmonic mode with the wavenumber q in Eq. (4.1) for simplicity. However, we note that, in general, the grating gate creates high-harmonic modulations of in-plane electric fields with the wavenumbers $2q$, $3q$, $\cdots$, Nq [310, 311, 316, 317], which can be described as

$$E_{in,i}(t,x) = \left[1 + \sum_{m=1}^{\infty} \hat{h}_i^{(m)} \cos\left(mqx + \phi_i^{(m)}\right)\right] E_{0i}(t). \tag{4.35}$$

These modulations result in multiple plasmonic resonant peaks at $\omega = \omega_{nq}$ ($n = 1, 2, \cdots$), leading to a remarkably broadband photocurrent spectrum. In particular, since the result in Eq. (4.33) does not depend on the phases $\phi_i^{(m)}$ and the signs of $h_x^{(m)}$, all the contributions of high-harmonic plasmons flow in the same direction, and thereby strongly enhance the total photocurrent. This is in sharp contrast to the case of the so-called ratchet effect [251, 317], which is strongly dependent on these parameters, and thus, each plasma mode often cancels each other. In conclusion, the enhancement factor (4.34) is modified by high-harmonic plasmons as follows:

$$\beta_\omega = 1 + \sum_{m=1}^{\infty} \frac{\tilde{\omega}^2(1+\tilde{\tau}^2\tilde{\omega}^2)(h_x^{(m)})^2}{2[m^2\tilde{\tau}^2(\tilde{\omega}^2-m^2)^2+\tilde{\omega}^2]}. \tag{4.36}$$

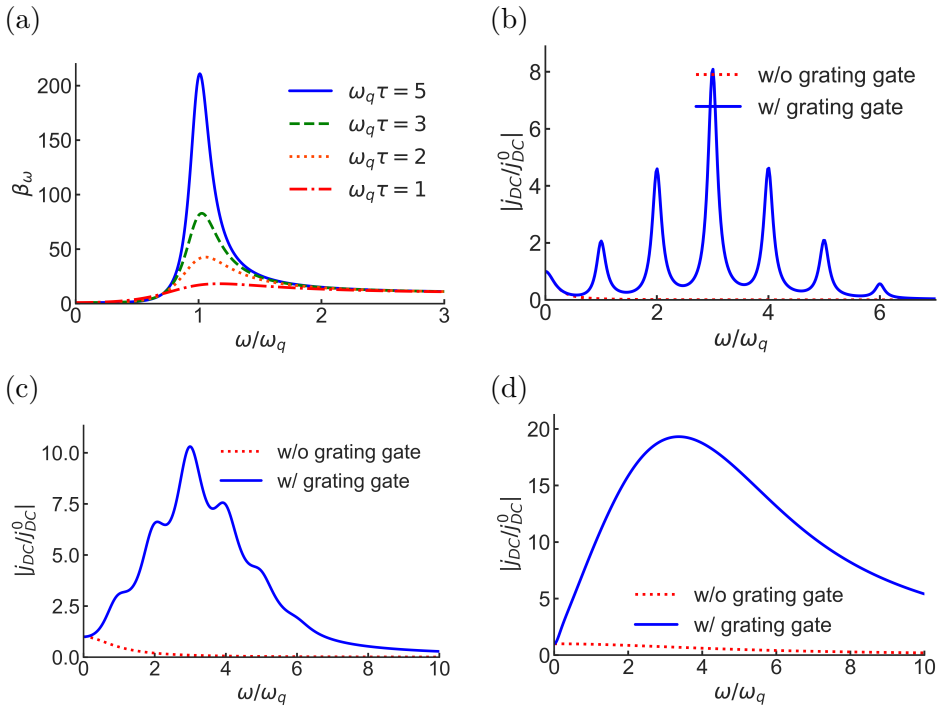

Figure 4.5: Frequency dependence of the enhancement factor β_ω and the plasmonic QNLH current $j_{DC} = j^{BCD}_{DC}$ [313]. (a) We plot the enhancement factor, Eq. (4.34), which comes from only one plasmonic peak, with $h_x = 4$ and various values of $\tilde{\tau} = \omega_q\tau$. (b-d) Considering the enhancement factor, Eq. (4.36), due to high-harmonic plasmons, we plot the plasmonic QNLH current, Eq. (4.33), normalized by $j^0_{DC} \equiv j_{DC}(\omega = 0)$. We set the paramter $\tilde{\tau} = \omega_q\tau$ as (b) $\omega_q\tau = 5$, (c) $\omega_q\tau = 1$, and (d) $\omega_q\tau = 0.2$ and, for demonstration purposes, assume phenomenologically that $(h^{(1)}_x, h^{(2)}_x, h^{(3)}_x, h^{(4)}_x, h^{(5)}_x, h^{(6)}_x) = (2, 3, 4, 3, 2, 1)$ and $h^{(i)} = 0$ $(i \geq 7)$. For comparison, we also plot the spectrum of the usual QNLH current with a red dotted line.

In Fig. 4.5 (b-d), We have plotted the spectrum of the plasmonic QNLH current (blue line), and campared it with that of the normal QNLH effect. From these figures, we find that the QNLH current is dramatically enhanced by several orders of amplitude, over a very broad range of frequency above the original frequency threshold $1/\tau$. Similar enhancement effects due to high-harmonic plasma modes have ever been discussed in the context of terahertz light absorption [92, 310, 318, 319] and plasmonic ratchet effect [252, 312].

4.5 Universal internal responsivity

Here, assuming more general situations, we elucidate a universal relation between the photocurrent induced by the BCD and the light absorption by 2D electron systems. First, in general, the BCD-induced photocurrent is obtained from Eq. (4.12) in the following form,

$$\boldsymbol{j}_{DC}^{BCD} = -\frac{me^2}{\hbar} \langle (\boldsymbol{D} \cdot \boldsymbol{u}(\boldsymbol{r},t))(\boldsymbol{E}(\boldsymbol{r},t) \times \hat{\boldsymbol{e}}_z) \rangle_{t,\boldsymbol{r}} \,, \tag{4.37}$$

where $\langle \cdots \rangle_{t,\boldsymbol{r}}$ denotes the time and space averaging over the periods. Especially for x-polarized incident light, it leads to $\boldsymbol{j}_{DC}^{BCD} = \frac{me^2}{\hbar} D_x \langle u_x E_x \rangle_{t,\boldsymbol{r}} \hat{\boldsymbol{e}}_y$. On the other hand, the optical power absorbed by 2D electron systems can be calculated as $\mathcal{P} = S \langle j_x E_x \rangle_{t,\boldsymbol{r}}$, where $S = L_x L_y$ is the area of our system and L_i is the sample's size in the i-direction. In the linear order of external perturbations, the electric current is related with the velocity field as $j_x = -en_0 u_x$ from Eq. (4.12), where n_0 is the equilibrium particle density. Combining these formulas, we reach the desired universal relation between $\boldsymbol{j}_{DC}^{BCD}$ and $\mathcal{P}$ as follows:

$$\boldsymbol{j}_{DC}^{BCD} = -\frac{emD_x \mathcal{P}}{\hbar n_0 S} \hat{\boldsymbol{e}}_y. \tag{4.38}$$

This relation means that the plasmonic QNLH effect discussed above comes from the plasmonic enhancement of the total optical absorption by grating gate. As understood from the derivation, Eq. (4.38) will be satisfied in more generic situations beyond our 2D grating model, such as plasmonic cavities [320, 321, 322, 323] or antennas [29, 324], as far as the frequency is low enough for interband transitions to be negligible.

Here we note that, in the case of y-polarized incident light, additional Hall currents induced by the oscillating magnetic field, which causes spatially dispersive terms such as $\boldsymbol{j}_{DC}^{Lorentz}$, slightly breaks this relation. Similarly, Eq. (4.38) does not hold for the circular photogalvanic current induced by the BCD. Furthermore, since we use the fact that the particle density n is spatially uniform in equilibrium to take it outside of $\langle \cdots \rangle_{t,\boldsymbol{r}}$, this relation will break in the case where strong static built-in fields is applied on the 2D electron systems by periodic doping gate as investigated in Ref. [251, 317].

From Eq. (4.38), we can immediately obtain the internal current responsivity of the BCD-induced Hall photocurrent, which is one of the most important figures of merit quantifying the performance of THz detectors [143] and defined as the current gain per absorbed light power,

$$\mathcal{R}_I \equiv \frac{I_y}{\mathcal{P}} = \frac{emD_x}{\hbar n_0 L_y}. \qquad (I_y = j_{DC,y}^{BCD} L_x) \tag{4.39}$$

This is another important result in this chapter. Eq. (4.39) states that the responsivity is entirely determined by the band structure (and the carrier density) of electron sytems, and completely independent on incident frequencies and their environment such as grating or cavity structures. Clearly, this peroperty is very beneficial for computational material design toword terahertz-infrared photodetectors. To realize a high-performance photodetector utilizing the BCD-induced photocurrent, first we should search quantum materials

with a collossal effective mass m and BCD by performing ab-initio calculations or experiments, and then, improve their optical absorption by decorating or designing those promising materials with some plasmonic or cavity structures.

For the latter purpose, 2D layered materials, which are very flexible to various device designs, seem to be more advantageous than 3D bulk materials. Recent experiments [325] have reported that the external voltage responsivity of bilayer WTe_2 reaches a value of 2×10^4 V/W^{-1} around $\omega \simeq 100$ Hz at $T = 10$ K, which is notably large and comparable to the best values in existing rectifiers [325, 326]. Furthermore, Ref. [327] has theoretically suggested that strained twisted bilayer graphene achieves a further large responsivity that is 20 times larger than the above values. However, since these materials work well only at low temperature, further investigations of promising materials, which show a remarkably large value of the BCD, will be needed to realize terahertz photodetectors working at room temperature.

4.6 Magnetically-driven plasmonic photogalvanic effect

Next let us consider a novel type of photocurrent, $\boldsymbol{j}_{DC}^{MPP}$, obtained in Eq. (4.22), which is regarded as a spatially dispersive correction to the total photocurrent and proportional to q^2 or q^4. For this reason, this effect is peculiar to spatially structured systems like our grating model, and does not appear in spatially uniform cases.

As shown in detail in the supplemental materials, the MPP effect originates from an anomalous driving force induced by oscillating magnetic fields ($\propto \boldsymbol{M}(\partial B/\partial t)$) in Eq. (4.9), and thus, they are described by the geometrical pseudovector, $\boldsymbol{M}$, i.e., the dipole moment of orbital magnetic moments of Bloch electrons in the momentum space (for the detailed derivation and expression, see the supplemental materials). In particular, at plasmon frequencies, the MPP current also has a sharp peak, as in the case of the plasmonic QNLH effect, and the peak amplitude is obtained under the resonant condition ($\tilde{\tau} \gg 1$) as follows [2]:

$$\begin{aligned}\boldsymbol{j}_{DC}^{MPP}(\omega = \omega_q) = &\frac{e^2\tau}{4ms^2}[\tilde{\tau} h_x h_y \mathcal{F}_z(\boldsymbol{M} + 2M_x \hat{\boldsymbol{e}}_x) \\ &+ \tilde{\tau}^2 h_x h_y \mathcal{L}_{xy} M_x \hat{\boldsymbol{e}}_x] + \mathcal{O}(\tilde{\tau}^0).\end{aligned} \tag{4.40}$$

Here we have introduced $\mathcal{F}_z = \frac{i}{2}(\tilde{E}_{0x}\tilde{E}_{0y}^* - \tilde{E}_{0y}\tilde{E}_{0x}^*)$ and $\mathcal{L}_{xy} = \frac{1}{2}(\tilde{E}_{0x}\tilde{E}_{0y}^* + \tilde{E}_{0y}\tilde{E}_{0x}^*)$, each of which represents a circular photogalvanic effect and a linear photogalvanic effect. Focusing on its circular photogalvanic effect in the x-direction, the value of MPP current is around 0.01 nA/W with typical values of parameters, $m \sim m_e$, $s \sim 1 \times 10^6$ m/s, $\tau \sim 1 \times 10^{-12}$ s and an estimated value of M_x obtained in Ref. [126] for strained graphene, $M_x \sim 3 \times 10^{17}$ s·A/kg·m, assuming the resonant case $|\tilde{\tau} h_x h_y| \sim 10$. Although this is much smaller than the measured value of QNLH current (~ 100 nA/W) in monolayer WTe_2 [328] around $\omega \simeq 30$ THz at 150 K, we might be able to improve the MPP current furthermore by seeking materials with a much larger value of $\boldsymbol{M}$. In such a situation, since the plasmonic term of the BCD-induced circular photocurrent is proportional to $\omega^2 - \omega_q^2$ and thus vanishes at the plasmon frequency, the MPP effect will dominate the total photocurrent. This might be one of good optical probes for the geometical strctures of Bloch electrons in 2D quantum systems.

[2] Here we have neglected the term proportional to geometrical scalar Y for simplicity, since it is a higher-order spatially disperive term, which is proportional to q^4, and thus much smaller than other terms for typical values of q.

4.7 Comment on the viscous effect

In the hydrodynamic regime, viscosity is one of key ingredients to characterize electron fluids. Actually, a lot of recent works have ever been devoted to measurements of the signature of viscosity in nonlocal transport phenomena [7, 11, 15, 18, 19, 20, 23]. The hydrodynamic equations obtained in Ref. [126, 286] do not include explicitly the contribution of the viscosity since they focus on the formulation in the limit of $(\omega\tau_e)^{-1} \to 0$, while the viscosity is a correction term in the first order of τ_e^{-1}. Here ω is the characteristic scale of the frequency we discuss. However, the viscous effects on our results are worth discussing by introducing viscosity terms into the theory phenomenologically. In what follows, we briefly discuss the viscous effects especially at the level of linear responses, which is enough to consider the modification of the QNLH term $\boldsymbol{j}_{DC}^{BCD}$.

First we can incorporate the viscous effects into our theory by adding the terms $\nu\Delta u + \zeta\boldsymbol{\nabla}(\boldsymbol{\nabla}\cdot\boldsymbol{u})$ to the right side of Eq. (4.10). Here ν is the kinematic viscosity, and ζ is the bulk viscosity (devided by the mass density mn). As easily checked, we can modify the results in Eq. (4.16) by replacing the dissipation rate $1/\tau$ appearing in the prefactor $(\omega^2 - \omega_q^2 - i\omega/\tau)^{-1}$ with $1/\tau + (\nu+\zeta)q^2$ for the case of longitudinal waves ($\boldsymbol{E}_0 \parallel \hat{\boldsymbol{e}}_x$). Clearly, this means that the viscosity of electron fluids gives rise to a spatial dispersive contribution in the lifetime of plasmons. When we assume that $\tau = 1\times10^{-12}$ s^{-1} and $\nu = 1\times10^{-1}$ m^{2}s^{-1} [7], the viscosity effect becomes comparable or superior to that of the momentum relaxing scattering rate $1/\tau$ under the condition that $2\pi/q \lesssim 1$ μm.

In particular, focusing on the enhancement factor β_ω, the electron viscosity modifies the factor as

$$\beta_\omega = 1 - \frac{\tilde{\omega}^2(1+\tilde{\tau}^2\tilde{\omega}^2)h_x^2}{2[\tilde{\tau}^2(\tilde{\omega}^2-1)^2+\tilde{\omega}^2]} \quad\longrightarrow\quad 1 - \frac{\tilde{\omega}^2(1+\tilde{\tau}^2\tilde{\omega}^2)(\tilde{\tau}_v/\tilde{\tau})h_x^2}{2[\tilde{\tau}_v^2(\tilde{\omega}^2-1)^2+\tilde{\omega}^2]}, \tag{4.41}$$

leading to the broadening of the peak width $1/\tilde{\tau} \to 1/\tilde{\tau}_v$ under the resonant condition, and the suppression of the peak amplitude $|\beta_{\omega_q}| \simeq |h_x\tilde{\tau}|^2/2 \to h_x^2\tilde{\tau}\tilde{\tau}_v/2$. Here we have introduced a new dimensionless parameter $\tilde{\tau}_v = \omega_q(1/\tau + (\nu+\zeta)q^2)^{-1}$ $(<\tilde{\tau})$. This means that, for typical values of parameters $\tau = 1\times10^{-12}$ [s^{-1}] and $\nu = 1\times10^{-1}$ [m^{2}s^{-1}] [7], the viscosity causes non-negligible contributions to the plasmon lifetime when the cycle length $L = 2\pi/q$ becomes μm-order or less. Consequently, it might be possible to optically probe mysterious aspects of strongly correlated electron systems such as twisted bilayer graphene [329, 330, 331, 332], through the peculiar temperature dependence of plasmon lifetime, since the electron viscosity behaves as $\nu \sim v_F l_{ee} \propto 1/T^2$ in Fermi liquids [23, 38, 333], while $\nu \propto 1/T$ in typical non-Fermi liquids [23, 53, 334, 335].

4.8 Candidates for our theory

Here we briefly discuss possible candidates to observe the novel types of plasmonic photocurrents obtained in this work. In the past few years, many pieces of evidence for hydrodynamic electron flow have been reported in various materials, including monolayer/bilayer graphene [7, 9, 10, 11, 13, 30], GaAs quantum wells [16, 17, 18, 19, 20, 21], 2D monovalent layered metal $PdCoO_2$ [15], Weyl semimetal WP_2 [23], and WTe_2 [24, 25, 26]. Among these materials, promising candidates for our work are graphene with some deformation and layered transition metal dichalcogenide WTe_2. These materials have crystal symmetries low enough to exhibit intriguing optical phenomena, such as the QNLH effect [279], which is required for the geometrical pseudovectors $\boldsymbol{D}$ and $\boldsymbol{M}$ to be finite. As a matter of fact, the QNLH effect itself has already been observed in layered WTe_2 [325, 328, 336, 337] and artificially corrugated bilayer graphene [338]. In particular, bilayer WTe_2 is reported

to show remarkably high responsivity [325] as already mentioned, and further dramatic enhancement of the BCD is suggested by twisting the two layers in Ref. [339].

Another possible candidate is (110) quantum well in GaAs, since it also has crystal symmetries low enough to show the QNLH effect [249, 280, 281, 340] and another type of GaAs quantum well has already shown various hydrodynamic signatures [16, 17, 19, 20, 21**?**]. Furthermore, twisted bilayer graphene, a novel layered system attracting great interest recently, might also be a candidate for our work, since this material is theoretically suggested to realize the hydrodynamic regime [341] and to show a remarkably high responsivity of the QNLH effect [327].

4.9 Conclusions and outlook of this chapter

In summary, based on an electron hydrodynamic theory, we have formulated plasmonically-driven geometrical photocurrents in nocentrosymmetric 2D layered systems with periodic grating gates. As a result, we have clarified that the quantum nonlinear Hall effect can be dramatically enhanced over a very broad range of frequency by utilizing plasmonic resonances and near-field effects of grating gates. This plasmonic QNLH effect is closely related with the optical absorption rate of the systems in general, and this property is crucially important to design the novel THz photodetectors using the QNLH effect.

Finally, we briefly give a future perspective of this work. First, our framework could be generalized to various types of problems in plasmonics, such as plasmonic responses of 1D vdW materials [342, 343] and gate-controlled optical activity [344], plasmon-to-current converters (plasmon detectors) [106, 345, 346]. For example, various microstructured graphene devices, such as graphene microdiscs [347] and graphene micro-ribbon arrays [148], have been enthusiastically discussed so far in the context of plasmonics. These devices achieve a strong THz absorption and the spectra are highly controllable by changing the sample size, gate voltage, and the layer number. By applying our formulation to these plasmonic systems, we can maybe obtain more efficient and tunable THz photodetectors that utilize the plasmonic QNLH effect. Moreover, although we have mainly focused on the two-dimensional systems, the universal relation between optical absorption and the BCD-induced photocurrent holds even in three-dimensional systems. In particular, as shown in Refs. [304, 348], Weyl semimetals have relatively large BCD due to the divergence of the Berry curvature near the Weyl nodes, and the (surface) plasmons have several unique features since they are essentially electron-hole liquids with linear dispersion and chiral anomaly [82, 349, 350, 351]. Generalizing our framework to include these materials might be an interesting problem from both theoretical and experimental perspectives.

Furthermore, the scope of applications of our formulation is not restricted to photogalvanic responses, but includes other various optical phenomena such as gate-controlled optical activity and plasmon-to-current conversion. For example, optical activities in two-dimensional systems without nanostructures, which are often described by geometrical quantities [127, 128, 129, 130, 131, 132, 133, 134], are typically small in the low frequency regime, due to the scale separation between the wavelength of incident lights and the microscopic length scale of electron systems. By utilizing the plasmonic resonance, we might be able to enhance these phenomena, leading to compact and electrically-controllable THz modulators.

We believe that these results provide us with a new way to investigate the role of quantum geometry in plasmonics, leading to a promising route toward a novel type of highly sensitive, broadband and electrically-controllable terahertz plasmonic devices.

Chapter 5

Conclusion

In this thesis, we have focused on anomalous electron hydrodynamics in noncentrosymmetric metals and its application to novel Thz photodetectors. As introduced in Chapter 1, although electron hydrodynamics is rapidly growing into a mature research area in the condensed matter physics in the last few years, there still remain many open problems related to the crystal symmetries and the geometrical structure of Bloch electrons. In particular, motivated by recent discovery of hydrodynamic materials without inversion symmetry, we have aimed to clarify the role of inversion symmetry breaking in electron hydrodynamics, and answer how we cam utilize these novel materials to develop practical optical devices.

In Chap. 3, we have formulated an anomalous hydrodynamic theory that can describe the quantum geometrical effects as anomalous driving forces. By using this framework, we can predict novel types of hydrodynamic flows, i.e. anomalous edge current and asymmetric Poiseuille flow. These phenomena are expected to be observable by using state-of-the-art experimental techniques, such as scanning magnetosensors with diamond nitrogen-vacancy center. We have also provided a group theoretical classification of electron fluids, and specified which existing hydrodynamic materials can exhibit anomalous hydrodynamic flows mentioned above.

In Chapter 4, we have investigated the interplay between quantum geometrical effects and surface plasmons, assuming the two-dimensional electron systems with surface plasmonic nanostructures, which is referred to as the periodic plasmonic grating model. As a result, we have clarified that the surface plasmon resonance plays an important role in enhancing the quantum nonlinear Hall (QNLH) effect in the frequency regime beyond its characteristic threshold. We have also proven a universal relation between the photocurrent induced by the Berry curvature dipole and the optical absorption rate of the electron systems. This relation is crucially important for the computational design of novel THz photodetectors that utilize the QNLH effect, and gives us a helpful roadmap to improve the external and internal responsivity of the photodetectors.

We believe that, through these works, we have opened up a new frontier of research that bridges several different research areas, inculuding electron hydrodynamics, quantum geometry, and plasmonics, which have been usually studied separately. In particular, incorporating plasmon physics into quantum geometrical physics is not only interesting from theoretical viewpoints, but also practically important problems, and it will lead to developing novel functional devices using novel quantum materials such as topological semimetals and van der Waals layered materials.

References

[1] N. W. Ashcroft and N. D. Mermin, *Solid State Physics* (Brooks/Cole, Cengage Learning, 1976).

[2] D. Xiao, M.-C. Chang, and Q. Niu, Rev. Mod. Phys. **82**, 1959 (2010).

[3] L. P. Kouwenhoven, G. Schön, and L. L. Sohn, "Introduction to mesoscopic electron transport," in *Mesoscopic Electron Transport*, edited by L. L. Sohn, L. P. Kouwenhoven, and G. Schön (Springer Netherlands, Dordrecht, 1997) pp. 1–44.

[4] D. T. Son and P. Surówka, Phys. Rev. Lett. **103**, 191601 (2009).

[5] K. Fukushima, D. E. Kharzeev, and H. J. Warringa, Phys. Rev. D **78**, 074033 (2008).

[6] R. Pasechnik and M. Šumbera, Universe **3** (2017), 10.3390/universe3010007.

[7] D. A. Bandurin, I. Torre, R. K. Kumar, M. Ben Shalom, A. Tomadin, A. Principi, G. H. Auton, E. Khestanova, K. S. Novoselov, I. V. Grigorieva, L. A. Ponomarenko, A. K. Geim, and M. Polini, **351**, 1055 (2016).

[8] F. Ghahari, H.-Y. Xie, T. Taniguchi, K. Watanabe, M. S. Foster, and P. Kim, Phys. Rev. Lett. **116**, 136802 (2016).

[9] R. K. Kumar, D. Bandurin, F. Pellegrino, Y. Cao, A. Principi, H. Guo, G. Auton, M. B. Shalom, L. A. Ponomarenko, G. Falkovich, *et al.*, Nature Physics **13**, 1182 (2017).

[10] D. A. Bandurin, A. V. Shytov, L. S. Levitov, R. K. Kumar, A. I. Berdyugin, M. Ben Shalom, I. V. Grigorieva, A. K. Geim, and G. Falkovich, Nature Communications **9**, 4533 (2018).

[11] A. I. Berdyugin, S. G. Xu, F. M. D. Pellegrino, R. Krishna Kumar, A. Principi, I. Torre, M. Ben Shalom, T. Taniguchi, K. Watanabe, I. V. Grigorieva, M. Polini, A. K. Geim, and D. A. Bandurin, Science **364**, 162 (2019), https://science.sciencemag.org/content/364/6436/162.full.pdf .

[12] C. Tan, D. Y. H. Ho, L. Wang, J. I. A. Li, I. Yudhistira, D. A. Rhodes, T. Taniguchi, K. Watanabe, K. Shepard, P. L. McEuen, C. R. Dean, S. Adam, and J. Hone, "Realization of a universal hydrodynamic semiconductor in ultra-clean dual-gated bilayer graphene," (2019), arXiv:1908.10921 .

[13] J. A. Sulpizio, L. Ella, A. Rozen, J. Birkbeck, D. J. Perello, D. Dutta, M. Ben-Shalom, T. Taniguchi, K. Watanabe, T. Holder, R. Queiroz, A. Principi, A. Stern, T. Scaffidi, A. K. Geim, and S. Ilani, Nature **576**, 75 (2019).

[14] P. Gallagher, C.-S. Yang, T. Lyu, F. Tian, R. Kou, H. Zhang, K. Watanabe, T. Taniguchi, and F. Wang, Science **364**, 158 (2019), https://science.sciencemag.org/content/364/6436/158.full.pdf .

[15] P. J. W. Moll, P. Kushwaha, N. Nandi, B. Schmidt, and A. P. Mackenzie, Science **351**, 1061 (2016), http://science.sciencemag.org/content/351/6277/1061.full.pdf .

[16] L. W. Molenkamp and M. J. M. de Jong, Phys. Rev. B **49**, 5038 (1994).

[17] M. J. M. de Jong and L. W. Molenkamp, Phys. Rev. B **51**, 13389 (1995).

[18] G. M. Gusev, A. D. Levin, E. V. Levinson, and A. K. Bakarov, AIP Advances **8**, 025318 (2018), https://doi.org/10.1063/1.5020763 .

[19] G. M. Gusev, A. D. Levin, E. V. Levinson, and A. K. Bakarov, Phys. Rev. B **98**, 161303 (2018).

[20] A. D. Levin, G. M. Gusev, E. V. Levinson, Z. D. Kvon, and A. K. Bakarov, Phys. Rev. B **97**, 245308 (2018).

[21] B. A. Braem, F. M. D. Pellegrino, A. Principi, M. Röösli, C. Gold, S. Hennel, J. V. Koski, M. Berl, W. Dietsche, W. Wegscheider, M. Polini, T. Ihn, and K. Ensslin, Phys. Rev. B **98**, 241304 (2018).

[22] A. Gupta, J. J. Heremans, S. Fallahi, and M. J. Manfra, "Hydrodynamic electron pumping in two-dimensional electron systems as a signature of viscous transport," (2019), arXiv:1907.00836 .

[23] J. Gooth, F. Menges, C. Shekhar, V. Süß, N. Kumar, Y. Sun, U. Drechsler, R. Zierold, C. Felser, and B. Gotsmann, Nature Communications **9**, 4093 (2018).

[24] U. Vool, A. Hamo, G. Varnavides, Y. Wang, T. X. Zhou, N. Kumar, Y. Dovzhenko, Z. Qiu, C. A. C. Garcia, A. T. Pierce, J. Gooth, P. Anikeeva, C. Felser, P. Narang, and A. Yacoby, Nature Physics **17**, 1216 (2021).

[25] Y.-G. Choi, M.-H. Doan, G.-M. Choi, and M. N. Chernodub, "Pseudo-hydrodynamic flow of quasiparticles in semimetal wte2 at room temperature," (2022), arXiv:2201.08331 .

[26] A. Aharon-Steinberg, T. Völkl, A. Kaplan, A. K. Pariari, I. Roy, T. Holder, Y. Wolf, A. Y. Meltzer, Y. Myasoedov, M. E. Huber, B. Yan, G. Falkovich, L. S. Levitov, M. Hücker, and E. Zeldov, "Direct observation of vortices in an electron fluid," (2022), arXiv:2202.02798 .

[27] M. Polini and A. K. Geim, Physics Today **73**, 28 (2020), https://doi.org/10.1063/PT.3.4497 .

[28] R. N. Gurzhi, Sov. Phys. JETP **44**, 771 (1963).

[29] D. A. Bandurin, D. Svintsov, I. Gayduchenko, S. G. Xu, A. Principi, M. Moskotin, I. Tretyakov, D. Yagodkin, S. Zhukov, T. Taniguchi, K. Watanabe, I. V. Grigorieva, M. Polini, G. N. Goltsman, A. K. Geim, and G. Fedorov, Nature Communications **9**, 5392 (2018).

[30] J. Crossno, J. K. Shi, K. Wang, X. Liu, A. Harzheim, A. Lucas, S. Sachdev, P. Kim, T. Taniguchi, K. Watanabe, T. A. Ohki, and K. C. Fong, Science **351**, 1058 (2016), https://science.sciencemag.org/content/351/6277/1058.full.pdf .

[31] I. Torre, A. Tomadin, A. K. Geim, and M. Polini, Phys. Rev. B **92**, 165433 (2015).

[32] J. Geurs, Y. Kim, K. Watanabe, T. Taniguchi, P. Moon, and J. H. Smet, "Rectification by hydrodynamic flow in an encapsulated graphene tesla valve," (2020), arXiv:2008.04862 .

[33] M. Palm, W. Huxter, P. Welter, S. Ernst, P. Scheidegger, S. Diesch, K. Chang, P. Rickhaus, T. Taniguchi, K. Watanabe, K. Ensslin, and C. Degen, Phys. Rev. Applied **17**, 054008 (2022).

[34] G. M. Gusev, A. S. Jaroshevich, A. D. Levin, Z. D. Kvon, and A. K. Bakarov, Scientific Reports **10**, 7860 (2020).

[35] A. Gupta, J. J. Heremans, G. Kataria, M. Chandra, S. Fallahi, G. C. Gardner, and M. J. Manfra, Phys. Rev. Lett. **126**, 076803 (2021).

[36] A. i. e. i. f. C. Keser, D. Q. Wang, O. Klochan, D. Y. H. Ho, O. A. Tkachenko, V. A. Tkachenko, D. Culcer, S. Adam, I. Farrer, D. A. Ritchie, O. P. Sushkov, and A. R. Hamilton, Phys. Rev. X **11**, 031030 (2021).

[37] W. Huang, T. Paul, K. Watanabe, T. Taniguchi, M. L. Perrin, and M. Calame, "Electronic poiseuille flow in hexagonal boron nitride encapsulated graphene fets," (2022), arXiv:2211.00398 .

[38] P. S. Alekseev, Phys. Rev. Lett. **117**, 166601 (2016).

[39] A. Principi and G. Vignale, Phys. Rev. Lett. **115**, 056603 (2015).

[40] M. Zarenia, T. B. Smith, A. Principi, and G. Vignale, Phys. Rev. B **99**, 161407 (2019).

[41] A. Jaoui, B. Fauqué, and K. Behnia, Nature Communications **12**, 195 (2021).

[42] N. Kumar, Y. Sun, M. Nicklas, S. J. Watzman, O. Young, I. Leermakers, J. Hornung, J. Klotz, J. Gooth, K. Manna, V. Süß, S. N. Guin, T. Förster, M. Schmidt, L. Muechler, B. Yan, P. Werner, W. Schnelle, U. Zeitler, J. Wosnitza, S. S. P. Parkin, C. Felser, and C. Shekhar, Nature Communications **10**, 2475 (2019).

[43] C.-w. Cho, P. Wang, F. Tang, S. Park, M. He, R. Lortz, G. Gu, Q. Li, and L. Zhang, Phys. Rev. B **105**, 085132 (2022).

[44] A. Jaoui, B. Fauqué, C. W. Rischau, A. Subedi, C. Fu, J. Gooth, N. Kumar, V. Süß, D. L. Maslov, C. Felser, and K. Behnia, npj Quantum Materials **3**, 64 (2018).

[45] R. Sano and M. Matsuo, "Breaking down the magnonic wiedemann-franz law in the hydrodynamic regime," (2022), arXiv:2208.14458 .

[46] Y.-T. Tu and S. D. Sarma, "Wiedemann-franz law in graphene," (2022), arXiv:2211.05192 .

[47] M. J. H. Ku, T. X. Zhou, Q. Li, Y. J. Shin, J. K. Shi, C. Burch, L. E. Anderson, A. T. Pierce, Y. Xie, A. Hamo, U. Vool, H. Zhang, F. Casola, T. Taniguchi, K. Watanabe, M. M. Fogler, P. Kim, A. Yacoby, and R. L. Walsworth, Nature **583**, 537 (2020).

[48] A. Jenkins, S. Baumann, H. Zhou, S. A. Meynell, Y. Daipeng, K. Watanabe, T. Taniguchi, A. Lucas, A. F. Young, and A. C. Bleszynski Jayich, Phys. Rev. Lett. **129**, 087701 (2022).

[49] L. Ella, A. Rozen, J. Birkbeck, M. Ben-Shalom, D. Perello, J. Zultak, T. Taniguchi, K. Watanabe, A. K. Geim, S. Ilani, and J. A. Sulpizio, Nature Nanotechnology **14**, 480 (2019).

[50] C. Kumar, J. Birkbeck, J. A. Sulpizio, D. Perello, T. Taniguchi, K. Watanabe, O. Reuven, T. Scaffidi, A. Stern, A. K. Geim, and S. Ilani, Nature **609**, 276 (2022).

[51] A. Aharon-Steinberg, T. Völkl, A. Kaplan, A. K. Pariari, I. Roy, T. Holder, Y. Wolf, A. Y. Meltzer, Y. Myasoedov, M. E. Huber, B. Yan, G. Falkovich, L. S. Levitov, M. Hücker, and E. Zeldov, Nature **607**, 74 (2022).

[52] M. Müller, J. Schmalian, and L. Fritz, Phys. Rev. Lett. **103**, 025301 (2009).

[53] P. K. Kovtun, D. T. Son, and A. O. Starinets, Phys. Rev. Lett. **94**, 111601 (2005).

[54] M. Mendoza, H. J. Herrmann, and S. Succi, Phys. Rev. Lett. **106**, 156601 (2011).

[55] D. Di Sante, J. Erdmenger, M. Greiter, I. Matthaiakakis, R. Meyer, D. R. Fernández, R. Thomale, E. van Loon, and T. Wehling, Nature Communications **11**, 3997 (2020).

[56] A. Gabbana, M. Polini, S. Succi, R. Tripiccione, and F. M. D. Pellegrino, Phys. Rev. Lett. **121**, 236602 (2018).

[57] M. Dyakonov and M. Shur, Phys. Rev. Lett. **71**, 2465 (1993).

[58] C. B. Mendl and A. Lucas, Applied Physics Letters **112**, 124101 (2018), https://doi.org/10.1063/1.5022187 .

[59] C. B. Mendl, M. Polini, and A. Lucas, Applied Physics Letters **118**, 013105 (2021), https://doi.org/10.1063/5.0030869 .

[60] J. Crabb, X. Cantos-Roman, J. M. Jornet, and G. R. Aizin, Phys. Rev. B **104**, 155440 (2021).

[61] J. H. Farrell, N. Grisouard, and T. Scaffidi, "Terahertz radiation from the dyakonov-shur instability of hydrodynamic electrons in a corbino geometry," (2021), arXiv:2112.07683 .

[62] P. O. Sukhachov, E. V. Gorbar, and I. A. Shovkovy, Phys. Rev. Lett. **127**, 176602 (2021).

[63] V. Galitski, M. Kargarian, and S. Syzranov, Phys. Rev. Lett. **121**, 176603 (2018).

[64] E. M. L. L. D. Landau and L. P. Pitaevskii, *Course of Theoretical Physics: Electrodynamics of Continuous Media 2nd Edition* (Pergamon, New York, 1984).

[65] R. Beck, A. Brandenburg, D. Moss, A. Shukurov, and D. Sokoloff, Annual Review of Astronomy and Astrophysics **34**, 155 (1996), https://doi.org/10.1146/annurev.astro.34.1.155 .

[66] P. Charbonneau, Annual Review of Astronomy and Astrophysics **52**, 251 (2014), https://doi.org/10.1146/annurev-astro-081913-040012 .

[67] A. Hui, V. Oganesyan, and E.-A. Kim, Phys. Rev. B **103**, 235152 (2021).

[68] D. Y. H. Ho, I. Yudhistira, N. Chakraborty, and S. Adam, Phys. Rev. B **97**, 121404 (2018).

[69] C. Tan, D. Y. H. Ho, L. Wang, J. I. A. Li, I. Yudhistira, D. A. Rhodes, T. Taniguchi, K. Watanabe, K. Shepard, P. L. McEuen, C. R. Dean, S. Adam, and J. Hone, Science Advances **8**, eabi8481 (2022), https://www.science.org/doi/pdf/10.1126/sciadv.abi8481 .

[70] E. Mönch, S. O. Potashin, K. Lindner, I. Yahniuk, L. E. Golub, V. Y. Kachorovskii, V. V. Bel'kov, R. Huber, K. Watanabe, T. Taniguchi, J. Eroms, D. Weiss, and S. D. Ganichev, Phys. Rev. B **105**, 045404 (2022).

[71] D. N. Basov, M. M. Fogler, and F. J. G. de Abajo, Science **354**, aag1992 (2016), https://www.science.org/doi/pdf/10.1126/science.aag1992 .

[72] A. Figotin and I. Vitebsky, Phys. Rev. E **63**, 066609 (2001).

[73] R. J. Pollard, A. Murphy, W. R. Hendren, P. R. Evans, R. Atkinson, G. A. Wurtz, A. V. Zayats, and V. A. Podolskiy, Phys. Rev. Lett. **102**, 127405 (2009).

[74] A. A. Orlov, P. M. Voroshilov, P. A. Belov, and Y. S. Kivshar, Phys. Rev. B **84**, 045424 (2011).

[75] G. A. Wurtz, R. Pollard, W. Hendren, G. P. Wiederrecht, D. J. Gosztola, V. A. Podolskiy, and A. V. Zayats, Nature Nanotechnology **6**, 107 (2011).

[76] P. Lodahl, S. Mahmoodian, S. Stobbe, A. Rauschenbeutel, P. Schneeweiss, J. Volz, H. Pichler, and P. Zoller, Nature **541**, 473 (2017).

[77] Z. Guo, H. Jiang, and H. Chen, Journal of Applied Physics **127**, 071101 (2020), https://doi.org/10.1063/1.5128679 .

[78] K. Cho, *Optical response of nanostructures: microscopic nonlocal theory*, Vol. 139 (Springer Science & Business Media, 2003).

[79] S. Raza, S. I. Bozhevolnyi, M. Wubs, and N. A. Mortensen, Journal of Physics: Condensed Matter **27**, 183204 (2015).

[80] N. Rivera and I. Kaminer, Nature Reviews Physics **2**, 538 (2020).

[81] A. Principi, M. I. Katsnelson, and G. Vignale, Phys. Rev. Lett. **117**, 196803 (2016).

[82] E. V. Gorbar, V. A. Miransky, I. A. Shovkovy, and P. O. Sukhachov, Phys. Rev. Lett. **118**, 127601 (2017).

[83] Y. Zhang, B. Guo, F. Zhai, and W. Jiang, Phys. Rev. B **97**, 115455 (2018).

[84] S. S.-L. Zhang and G. Vignale, Phys. Rev. B **97**, 224408 (2018).

[85] D. Svintsov, Phys. Rev. B **97**, 121405 (2018).

[86] P. O. Sukhachov, E. V. Gorbar, I. A. Shovkovy, and V. A. Miransky, Journal of Physics: Condensed Matter **30**, 275601 (2018).

[87] E. V. Gorbar, V. A. Miransky, I. A. Shovkovy, and P. O. Sukhachov, Phys. Rev. B **97**, 121105 (2018).

[88] B. N. Narozhny, I. V. Gornyi, and M. Titov, Phys. Rev. B **103**, 115402 (2021).

[89] K. Kapralov and D. Svintsov, "Ballistic-to-hydrodynamic transition and collective modes for two-dimensional electron systems in magnetic field," (2022), arXiv:2203.04479 .

[90] M. Mendoza, H. J. Herrmann, and S. Succi, Scientific Reports **3**, 1052 (2013).

[91] D. Forcella, J. Zaanen, D. Valentinis, and D. van der Marel, Phys. Rev. B **90**, 035143 (2014).

[92] B. Yan, X.-X. Yang, J.-Y. Fang, Y.-D. Huang, H. Qin, and S.-Q. Qin, Chinese Physics B **24**, 015203 (2015).

[93] Z. Sun, D. N. Basov, and M. M. Fogler, Phys. Rev. B **97**, 075432 (2018).

[94] Z. Sun, D. N. Basov, and M. M. Fogler, Proceedings of the National Academy of Sciences **115**, 3285 (2018), https://www.pnas.org/doi/pdf/10.1073/pnas.1717010115 .

[95] P. S. Alekseev, Phys. Rev. B **98**, 165440 (2018).

[96] P. S. Alekseev and A. P. Alekseeva, Phys. Rev. Lett. **123**, 236801 (2019).

[97] V. Ryzhii, T. Otsuji, and M. Shur, Applied Physics Letters **116**, 140501 (2020), https://doi.org/10.1063/1.5140712 .

[98] S. O. Potashin, V. Y. Kachorovskii, and M. S. Shur, Phys. Rev. B **102**, 085402 (2020).

[99] M. W. Shabbir and M. N. Leuenberger, Scientific Reports **10**, 17540 (2020).

[100] P. S. Alekseev and A. P. Alekseeva, "Microwave-induced resistance oscillations in highly viscous electron fluid," (2021), arXiv:2105.01035 .

[101] L. F. Man, W. Xu, Y. M. Xiao, H. Wen, L. Ding, B. Van Duppen, and F. M. Peeters, Phys. Rev. B **104**, 125420 (2021).

[102] Y. Zhang and M. S. Shur, Journal of Applied Physics **129**, 053102 (2021), https://doi.org/10.1063/5.0038775 .

[103] F. De Luca, M. Ortolani, and C. Ciracì, Phys. Rev. B **103**, 115305 (2021).

[104] Y. A. Pusep, M. D. Teodoro, V. Laurindo, E. R. Cardozo de Oliveira, G. M. Gusev, and A. K. Bakarov, Phys. Rev. Lett. **128**, 136801 (2022).

[105] D. Valentinis, G. Baker, D. A. Bonn, and J. Schmalian, "Kinetic theory of the non-local electrodynamic response in anisotropic metals: skin effect in 2d systems," (2022), arXiv:2204.13344 .

[106] I. Torre, A. Tomadin, R. Krahne, V. Pellegrini, and M. Polini, Phys. Rev. B **91**, 081402 (2015).

[107] F. M. D. Pellegrino, I. Torre, A. K. Geim, and M. Polini, Phys. Rev. B **94**, 155414 (2016).

[108] F. M. D. Pellegrino, I. Torre, and M. Polini, Phys. Rev. B **96**, 195401 (2017).

[109] T. Scaffidi, N. Nandi, B. Schmidt, A. P. Mackenzie, and J. E. Moore, Phys. Rev. Lett. **118**, 226601 (2017).

[110] H. Guo, E. Ilseven, G. Falkovich, and L. S. Levitov, Proceedings of the National Academy of Sciences **114**, 3068 (2017), https://www.pnas.org/content/114/12/3068.full.pdf .

[111] M. Chandra, G. Kataria, D. Sahdev, and R. Sundararaman, Phys. Rev. B **99**, 165409 (2019).

[112] K. A. Guerrero-Becerra, F. M. D. Pellegrino, and M. Polini, Phys. Rev. B **99**, 041407 (2019).

[113] R. J. Doornenbal, M. Polini, and R. A. Duine, Journal of Physics: Materials **2**, 015006 (2019).

[114] A. Hui, S. Lederer, V. Oganesyan, and E.-A. Kim, Phys. Rev. B **101**, 121107 (2020).

[115] Y. Tokura and N. Nagaosa, Nature Communications **9**, 3740 (2018).

[116] R. Kubo, Journal of the Physical Society of Japan **12**, 570 (1957), https://doi.org/10.1143/JPSJ.12.570 .

[117] G. L. J. A. Rikken and E. Raupach, Nature **390**, 493 (1997).

[118] G. L. J. A. Rikken and E. Raupach, Phys. Rev. E **58**, 5081 (1998).

[119] Y. Iguchi, S. Uemura, K. Ueno, and Y. Onose, Phys. Rev. B **92**, 184419 (2015).

[120] S. Seki, Y. Okamura, K. Kondou, K. Shibata, M. Kubota, R. Takagi, F. Kagawa, M. Kawasaki, G. Tatara, Y. Otani, and Y. Tokura, Phys. Rev. B **93**, 235131 (2016).

[121] T. J. Sato, D. Okuyama, T. Hong, A. Kikkawa, Y. Taguchi, T.-h. Arima, and Y. Tokura, Phys. Rev. B **94**, 144420 (2016).

[122] G. Gitgeatpong, Y. Zhao, P. Piyawongwatthana, Y. Qiu, L. W. Harriger, N. P. Butch, T. J. Sato, and K. Matan, Phys. Rev. Lett. **119**, 047201 (2017).

[123] A. L. Fetter, Phys. Rev. B **32**, 7676 (1985).

[124] J. C. W. Song and M. S. Rudner, Proceedings of the National Academy of Sciences **113**, 4658 (2016), https://www.pnas.org/doi/pdf/10.1073/pnas.1519086113 .

[125] A. Kumar, A. Nemilentsau, K. H. Fung, G. Hanson, N. X. Fang, and T. Low, Phys. Rev. B **93**, 041413 (2016).

[126] R. Sano, R. Toshio, and N. Kawakami, Phys. Rev. B **104**, L241106 (2021).

[127] A. Malashevich and I. Souza, Phys. Rev. B **82**, 245118 (2010).

[128] J. Orenstein and J. E. Moore, Phys. Rev. B **87**, 165110 (2013).

[129] S. Zhong, J. Orenstein, and J. E. Moore, Phys. Rev. Lett. **115**, 117403 (2015).

[130] J. Ma and D. A. Pesin, Phys. Rev. B **92**, 235205 (2015).

[131] P. Hosur and X.-L. Qi, Phys. Rev. B **91**, 081106 (2015).

[132] S. Zhong, J. E. Moore, and I. Souza, Phys. Rev. Lett. **116**, 077201 (2016).

[133] F. Flicker, F. de Juan, B. Bradlyn, T. Morimoto, M. G. Vergniory, and A. G. Grushin, Phys. Rev. B **98**, 155145 (2018).

[134] Y.-Q. Wang, T. Morimoto, and J. E. Moore, Phys. Rev. B **101**, 174419 (2020).

[135] Y. Gao and D. Xiao, Phys. Rev. Lett. **122**, 227402 (2019).

[136] L.-k. Shi, D. Zhang, K. Chang, and J. C. W. Song, Phys. Rev. Lett. **126**, 197402 (2021).

[137] F. H. L. Koppens, D. E. Chang, and F. J. García de Abajo, Nano Letters **11**, 3370 (2011).

[138] A. N. Grigorenko, M. Polini, and K. S. Novoselov, Nature Photonics **6**, 749 (2012).

[139] T. Low and P. Avouris, ACS Nano **8**, 1086 (2014).

[140] M. L. Brongersma and V. M. Shalaev, Science **328**, 440 (2010), https://www.science.org/doi/pdf/10.1126/science.1186905 .

[141] V. J. Sorger, R. F. Oulton, R.-M. Ma, and X. Zhang, MRS Bulletin **37**, 728–738 (2012).

[142] T. J. Davis, D. E. Gómez, and A. Roberts, Nanophotonics **6**, 543 (2017).

[143] F. H. L. Koppens, T. Mueller, P. Avouris, A. C. Ferrari, M. S. Vitiello, and M. Polini, Nature Nanotechnology **9**, 780 (2014).

[144] M. Li, S. K. Cushing, and N. Wu, Analyst **140**, 386 (2015).

[145] K. Catchpole and A. Polman, Opt. Express **16**, 21793 (2008).

[146] H. A. Atwater and A. Polman, Nature Materials **9**, 205 (2010).

[147] Y. H. Jang, Y. J. Jang, S. Kim, L. N. Quan, K. Chung, and D. H. Kim, Chemical Reviews **116**, 14982 (2016).

[148] L. Ju, B. Geng, J. Horng, C. Girit, M. Martin, Z. Hao, H. A. Bechtel, X. Liang, A. Zettl, Y. R. Shen, and F. Wang, Nature Nanotechnology **6**, 630 (2011).

[149] Y. Li, Z. Li, C. Chi, H. Shan, L. Zheng, and Z. Fang, Advanced Science **4**, 1600430 (2017), https://onlinelibrary.wiley.com/doi/pdf/10.1002/advs.201600430 .

[150] T. Otsuji and M. Shur, IEEE Microwave Magazine **15**, 43 (2014).

[151] A. Rogalski, M. Kopytko, and P. Martyniuk, Opto-Electronics Review **28**, 107 (2020).

[152] M. Tonouchi, Nature Photonics **1**, 97 (2007).

[153] J. B. Baxter and G. W. Guglietta, Analytical Chemistry **83**, 4342 (2011).

[154] D. Nicoletti and A. Cavalleri, Adv. Opt. Photon. **8**, 401 (2016).

[155] X. Zhang, Q. Xu, L. Xia, Y. Li, J. Gu, Z. Tian, C. Ouyang, J. Han, and W. Zhang, Advanced Photonics **2**, 014001 (2020).

[156] X. C. Zhang, A. Shkurinov, and Y. Zhang, Nature Photonics **11**, 16 (2017).

[157] R. A. Lewis, Journal of Physics D: Applied Physics **47**, 374001 (2014).

[158] R. A. Lewis, Journal of Physics D: Applied Physics **52**, 433001 (2019).

[159] M. Walther, P. Plochocka, B. Fischer, H. Helm, and P. Uhd Jepsen, Biopolymers **67**, 310 (2002), https://onlinelibrary.wiley.com/doi/pdf/10.1002/bip.10106 .

[160] M. Walther, B. Fischer, M. Schall, H. Helm, and P. Jepsen, Chemical Physics Letters **332**, 389 (2000).

[161] K. Kawase, Y. Ogawa, Y. Watanabe, and H. Inoue, Opt. Express **11**, 2549 (2003).

[162] B. M. Fischer, M. Hoffmann, H. Helm, R. Wilk, F. Rutz, T. Kleine-Ostmann, M. Koch, and P. U. Jepsen, Opt. Express **13**, 5205 (2005).

[163] X. Yang, X. Zhao, K. Yang, Y. Liu, Y. Liu, W. Fu, and Y. Luo, Trends in Biotechnology **34**, 810 (2016).

[164] L. Yu, L. Hao, T. Meiqiong, H. Jiaoqi, L. Wei, D. Jinying, C. Xueping, F. Weiling, and Z. Yang, RSC Adv. **9**, 9354 (2019).

[165] A. Ahmadivand, B. Gerislioglu, R. Ahuja, and Y. Kumar Mishra, Materials Today **32**, 108 (2020).

[166] D. Rodrigo, O. Limaj, D. Janner, D. Etezadi, F. J. G. de Abajo, V. Pruneri, and H. Altug, Science **349**, 165 (2015), https://www.science.org/doi/pdf/10.1126/science.aab2051 .

[167] S. J. Park, J. T. Hong, S. J. Choi, H. S. Kim, W. K. Park, S. T. Han, J. Y. Park, S. Lee, D. S. Kim, and Y. H. Ahn, Scientific Reports **4**, 4988 (2014).

[168] R. Adato, A. A. Yanik, J. J. Amsden, D. L. Kaplan, F. G. Omenetto, M. K. Hong, S. Erramilli, and H. Altug, Proceedings of the National Academy of Sciences **106**, 19227 (2009), https://www.pnas.org/doi/pdf/10.1073/pnas.0907459106 .

[169] E. Pickwell and V. P. Wallace, Journal of Physics D: Applied Physics **39**, R301 (2006).

[170] A. J. Fitzgerald, E. Berry, N. N. Zinov'ev, S. Homer-Vanniasinkam, R. E. Miles, J. M. Chamberlain, and M. A. Smith, J Biol Phys **29**, 123 (2003).

[171] E. Pickwell, A. J. Fitzgerald, B. E. Cole, P. F. Taday, R. J. Pye, T. Ha, M. Pepper, and V. P. Wallace, Journal of Biomedical Optics **10**, 064021 (2005).

[172] Y.-C. Shen, International Journal of Pharmaceutics **417**, 48 (2011), advanced characterization techniques.

[173] T. Kleine-Ostmann and T. Nagatsuma, Journal of Infrared, Millimeter, and Terahertz Waves **32**, 143 (2011).

[174] Z. Chen, X. Ma, B. Zhang, Y. Zhang, Z. Niu, N. Kuang, W. Chen, L. Li, and S. Li, China Communications **16**, 1 (2019).

[175] T. S. Rappaport, Y. Xing, O. Kanhere, S. Ju, A. Madanayake, S. Mandal, A. Alkhateeb, and G. C. Trichopoulos, IEEE Access **7**, 78729 (2019).

[176] R. Piesiewicz, T. Kleine-Ostmann, N. Krumbholz, D. Mittleman, M. Koch, J. Schoebel, and T. Kurner, IEEE Antennas and Propagation Magazine **49**, 24 (2007).

[177] Y. Yang, A. Shutler, and D. Grischkowsky, Opt. Express **19**, 8830 (2011).

[178] D. M. Slocum, E. J. Slingerland, R. H. Giles, and T. M. Goyette, Journal of Quantitative Spectroscopy and Radiative Transfer **127**, 49 (2013).

[179] H. Friis, Proceedings of the IRE **34**, 254 (1946).

[180] T. Rappaport, English (US) *Wireless communications: Principles and practice*, 2nd ed., Prentice Hall communications engineering and emerging technologies series (Prentice Hall, 2002) includes bibliographical references and index.

[181] T. Rappaport, R. Heath, R. Daniels, and J. Murdock, English (US) *Millimeter wave wireless communications* (Prentice Hall, 2015) includes bibliographical references (pages 585-651) and index.

[182] T. S. Rappaport, Y. Xing, G. R. MacCartney, A. F. Molisch, E. Mellios, and J. Zhang, IEEE Transactions on Antennas and Propagation **65**, 6213 (2017).

[183] K. KrishneGowda, T. Messinger, A. C. Wolf, R. Kraemer, I. Kallfass, and J. C. Scheytt, in *2015 IEEE International Conference on Ubiquitous Wireless Broadband (ICUWB)* (2015) pp. 1–5.

[184] J. Webber, A. Oshiro, S. Iwamatsu, Y. Nishida, M. Fujita, and T. Nagatsuma, Electronics Letters **57**, 668 (2021), https://ietresearch.onlinelibrary.wiley.com/doi/pdf/10.1049/ell2.12219 .

[185] T. Kürner, Terahertz science and technology **5**, 11 (2012).

[186] S. Dong, J.-M. Liu, S.-W. Cheong, and Z. Ren, Advances in Physics **64**, 519 (2015), https://doi.org/10.1080/00018732.2015.1114338 .

[187] T. Kampfrath, A. Sell, G. Klatt, A. Pashkin, S. Mährlein, T. Dekorsy, M. Wolf, M. Fiebig, A. Leitenstorfer, and R. Huber, Nature Photonics **5**, 31 (2011).

[188] M. B. Jungfleisch, W. Zhang, and A. Hoffmann, Physics Letters A **382**, 865 (2018).

[189] R. Shimano and N. Tsuji, Annual Review of Condensed Matter Physics **11**, 103 (2020), https://doi.org/10.1146/annurev-conmatphys-031119-050813 .

[190] D. Fausti, R. I. Tobey, N. Dean, S. Kaiser, A. Dienst, M. C. Hoffmann, S. Pyon, T. Takayama, H. Takagi, and A. Cavalleri, Science **331**, 189 (2011), https://www.science.org/doi/pdf/10.1126/science.1197294 .

[191] M. Mitrano, A. Cantaluppi, D. Nicoletti, S. Kaiser, A. Perucchi, S. Lupi, P. Di Pietro, D. Pontiroli, M. Riccò, S. R. Clark, D. Jaksch, and A. Cavalleri, Nature **530**, 461 (2016).

[192] A. Cavalleri, Contemporary Physics **59**, 31 (2018).

[193] R. Matsunaga, Y. I. Hamada, K. Makise, Y. Uzawa, H. Terai, Z. Wang, and R. Shimano, Phys. Rev. Lett. **111**, 057002 (2013).

[194] R. Matsunaga, N. Tsuji, H. Fujita, A. Sugioka, K. Makise, Y. Uzawa, H. Terai, Z. Wang, H. Aoki, and R. Shimano, Science **345**, 1145 (2014), https://www.science.org/doi/pdf/10.1126/science.1254697 .

[195] R. Matsunaga, N. Tsuji, K. Makise, H. Terai, H. Aoki, and R. Shimano, Phys. Rev. B **96**, 020505 (2017).

[196] V. Ardizzone, L. D. Marco, M. D. Giorgi, L. Dominici, D. Ballarini, and D. Sanvitto, Nanophotonics **8**, 1547 (2019).

[197] Z. Fang, S. Thongrattanasiri, A. Schlather, Z. Liu, L. Ma, Y. Wang, P. M. Ajayan, P. Nordlander, N. J. Halas, and F. J. García de Abajo, ACS Nano **7**, 2388 (2013).

[198] B. Chakraborty, J. Gu, Z. Sun, M. Khatoniar, R. Bushati, A. L. Boehmke, R. Koots, and V. M. Menon, Nano Letters **18**, 6455 (2018).

[199] F. Sun, L. Xia, C. Nie, C. Qiu, L. Tang, J. Shen, T. Sun, L. Yu, P. Wu, S. Yin, S. Yan, and C. Du, Applied Physics Express **12**, 042009 (2019).

[200] S. Dai, Q. Ma, T. Andersen, A. S. Mcleod, Z. Fei, M. K. Liu, M. Wagner, K. Watanabe, T. Taniguchi, M. Thiemens, F. Keilmann, P. Jarillo-Herrero, M. M. Fogler, and D. N. Basov, Nature Communications **6**, 6963 (2015).

[201] P. Li, M. Lewin, A. V. Kretinin, J. D. Caldwell, K. S. Novoselov, T. Taniguchi, K. Watanabe, F. Gaussmann, and T. Taubner, Nature Communications **6**, 7507 (2015).

[202] S. Wu, S. Buckley, J. R. Schaibley, L. Feng, J. Yan, D. G. Mandrus, F. Hatami, W. Yao, J. Vučković, A. Majumdar, and X. Xu, Nature **520**, 69 (2015).

[203] D. Sanvitto and S. Kéna-Cohen, Nature Materials **15**, 1061 (2016).

[204] X. Liu, T. Galfsky, Z. Sun, F. Xia, E.-c. Lin, Y.-H. Lee, S. Kéna-Cohen, and V. M. Menon, Nature Photonics **9**, 30 (2015).

[205] K. J. A. Ooi and D. T. H. Tan, Proceedings of the Royal Society A: Mathematical, Physical and Engineering Sciences **473**, 20170433 (2017), https://royalsocietypublishing.org/doi/pdf/10.1098/rspa.2017.0433 .

[206] J. Gu, V. Walther, L. Waldecker, D. Rhodes, A. Raja, J. C. Hone, T. F. Heinz, S. Kéna-Cohen, T. Pohl, and V. M. Menon, Nature Communications **12**, 2269 (2021).

[207] I. Alonso Calafell, J. D. Cox, M. Radonjić, J. R. M. Saavedra, F. J. García de Abajo, L. A. Rozema, and P. Walther, npj Quantum Information **5**, 37 (2019).

[208] M. Nalabothula, P. K. Jha, T. Low, and A. Kumar, Phys. Rev. B **102**, 045416 (2020).

[209] D. Nigro, V. D'Ambrosio, D. Sanvitto, and D. Gerace, Communications Physics **5**, 34 (2022).

[210] M. Ono, M. Hata, M. Tsunekawa, K. Nozaki, H. Sumikura, H. Chiba, and M. Notomi, Nature Photonics **14**, 37 (2020).

[211] Z. Cheng, R. Cao, K. Wei, Y. Yao, X. Liu, J. Kang, J. Dong, Z. Shi, H. Zhang, and X. Zhang, Advanced Science **8**, 2003834 (2021), https://onlinelibrary.wiley.com/doi/pdf/10.1002/advs.202003834 .

[212] Y. Li, K. Tantiwanichapan, A. K. Swan, and R. Paiella, Nanophotonics **9**, 1901 (2020).

[213] J. Takahara, S. Yamagishi, H. Taki, A. Morimoto, and T. Kobayashi, Opt. Lett. **22**, 475 (1997).

[214] K. Kneipp, Y. Wang, H. Kneipp, L. T. Perelman, I. Itzkan, R. R. Dasari, and M. S. Feld, Phys. Rev. Lett. **78**, 1667 (1997).

[215] S. Nie and S. R. Emory, Science **275**, 1102 (1997), https://www.science.org/doi/pdf/10.1126/science.275.5303.1102 .

[216] T. W. Ebbesen, H. J. Lezec, H. F. Ghaemi, T. Thio, and P. A. Wolff, Nature **391**, 667 (1998).

[217] J. B. Pendry, Phys. Rev. Lett. **85**, 3966 (2000).

[218] V. Amendola, R. Pilot, M. Frasconi, O. M. Maragò, and M. A. Iatì, Journal of Physics: Condensed Matter **29**, 203002 (2017).

[219] N. C. Panoiu, W. E. I. Sha, D. Y. Lei, and G.-C. Li, Journal of Optics **20**, 083001 (2018).

[220] K. Yao and Y. Liu, Nanotechnology Reviews **3**, 177 (2014).

[221] M. Hentschel, M. Schäferling, X. Duan, H. Giessen, and N. Liu, Science Advances **3**, e1602735 (2017), https://www.science.org/doi/pdf/10.1126/sciadv.1602735 .

[222] D. K. Gramotnev and S. I. Bozhevolnyi, Nature Photonics **4**, 83 (2010).

[223] J. A. Schuller, E. S. Barnard, W. Cai, Y. C. Jun, J. S. White, and M. L. Brongersma, Nature Materials **9**, 193 (2010).

[224] L. Novotny and N. van Hulst, Nature Photonics **5**, 83 (2011).

[225] W. Cai, U. K. Chettiar, A. V. Kildishev, and V. M. Shalaev, Nature Photonics **1**, 224 (2007).

[226] V. M. Shalaev, Nature Photonics **1**, 41 (2007).

[227] B. Luk'yanchuk, N. I. Zheludev, S. A. Maier, N. J. Halas, P. Nordlander, H. Giessen, and C. T. Chong, Nature Materials **9**, 707 (2010).

[228] S. Kawata, Y. Inouye, and P. Verma, Nature Photonics **3**, 388 (2009).

[229] H. Xu, E. J. Bjerneld, M. Käll, and L. Börjesson, Phys. Rev. Lett. **83**, 4357 (1999).

[230] A. V. Kabashin, P. Evans, S. Pastkovsky, W. Hendren, G. A. Wurtz, R. Atkinson, R. Pollard, V. A. Podolskiy, and A. V. Zayats, Nature Materials **8**, 867 (2009).

[231] J. R. Mejía-Salazar and O. N. Oliveira Jr., Chemical Reviews **118**, 10617 (2018).

[232] A. M. Shrivastav, U. Cvelbar, and I. Abdulhalim, Communications Biology **4**, 70 (2021).

[233] D. E. Chang, A. S. Sørensen, E. A. Demler, and M. D. Lukin, Nature Physics **3**, 807 (2007).

[234] A. Gonzalez-Tudela, D. Martin-Cano, E. Moreno, L. Martin-Moreno, C. Tejedor, and F. J. Garcia-Vidal, Phys. Rev. Lett. **106**, 020501 (2011).

[235] M. S. Tame, K. R. McEnery, Ş. K. Özdemir, J. Lee, S. A. Maier, and M. S. Kim, Nature Physics **9**, 329 (2013).

[236] A. Chaplik, Surface Science Reports **5**, 289 (1985).

[237] J. Chen, M. Badioli, P. Alonso-González, S. Thongrattanasiri, F. Huth, J. Osmond, M. Spasenović, A. Centeno, A. Pesquera, P. Godignon, A. Zurutuza Elorza, N. Camara, F. J. G. de Abajo, R. Hillenbrand, and F. H. L. Koppens, Nature **487**, 77 (2012).

[238] Z. Fei, A. S. Rodin, G. O. Andreev, W. Bao, A. S. McLeod, M. Wagner, L. M. Zhang, Z. Zhao, M. Thiemens, G. Dominguez, M. M. Fogler, A. H. C. Neto, C. N. Lau, F. Keilmann, and D. N. Basov, Nature **487**, 82 (2012).

[239] C. Ciracì, J. B. Pendry, and D. R. Smith, ChemPhysChem **14**, 1109 (2013), https://chemistry-europe.onlinelibrary.wiley.com/doi/pdf/10.1002/cphc.201200992 .

[240] A. V. Krasavin, P. Ginzburg, and A. V. Zayats, Laser & Photonics Reviews **12**, 1700082 (2018), https://onlinelibrary.wiley.com/doi/pdf/10.1002/lpor.201700082 .

[241] A. Reserbat-Plantey, I. Epstein, I. Torre, A. T. Costa, P. A. D. Gonçalves, N. A. Mortensen, M. Polini, J. C. W. Song, N. M. R. Peres, and F. H. L. Koppens, ACS Photonics **8**, 85 (2021).

[242] B. N. Narozhny, La Rivista del Nuovo Cimento (2022), 10.1007/s40766-022-00036-z.

[243] A. Lucas and K. C. Fong, Journal of Physics: Condensed Matter **30**, 053001 (2018).

[244] I. Torre, L. Vieira de Castro, B. Van Duppen, D. Barcons Ruiz, F. m. c. M. Peeters, F. H. L. Koppens, and M. Polini, Phys. Rev. B **99**, 144307 (2019).

[245] V. Ryzhii, A. Satou, and T. Otsuji, Journal of Applied Physics **101**, 024509 (2007), https://doi.org/10.1063/1.2426904 .

[246] E. H. Hwang and S. Das Sarma, Phys. Rev. B **75**, 205418 (2007).

[247] J. Hofmann and S. Das Sarma, Phys. Rev. B **91**, 241108 (2015).

[248] M. Dyakonov and M. Shur, IEEE Transactions on Electron Devices **43**, 380 (1996).

[249] P. Olbrich, S. A. Tarasenko, C. Reitmaier, J. Karch, D. Plohmann, Z. D. Kvon, and S. D. Ganichev, Phys. Rev. B **79**, 121302 (2009).

[250] E. L. Ivchenko and S. D. Ganichev, JETP Letters **93**, 673 (2011).

[251] I. V. Rozhansky, V. Y. Kachorovskii, and M. S. Shur, Phys. Rev. Lett. **114**, 246601 (2015).

[252] P. Olbrich, J. Kamann, M. König, J. Munzert, L. Tutsch, J. Eroms, D. Weiss, M.-H. Liu, L. E. Golub, E. L. Ivchenko, V. V. Popov, D. V. Fateev, K. V. Mashinsky, F. Fromm, T. Seyller, and S. D. Ganichev, Phys. Rev. B **93**, 075422 (2016).

[253] S. D. Ganichev, D. Weiss, and J. Eroms, Annalen der Physik **529**, 1600406 (2017), https://onlinelibrary.wiley.com/doi/pdf/10.1002/andp.201600406 .

[254] V. Popov, M. Shur, G. Tsymbalov, and D. Fateev, International Journal of High Speed Electronics and Systems **17**, 557 (2007).

[255] W. Knap, J. Lusakowski, T. Parenty, S. Bollaert, A. Cappy, V. V. Popov, and M. S. Shur, Applied Physics Letters **84**, 2331 (2004), https://doi.org/10.1063/1.1689401 .

[256] A. El Fatimy, N. Dyakonova, Y. Meziani, T. Otsuji, W. Knap, S. Vandenbrouk, K. Madjour, D. Théron, C. Gaquiere, M. A. Poisson, S. Delage, P. Prystawko, and C. Skierbiszewski, Journal of Applied Physics **107**, 024504 (2010), https://doi.org/10.1063/1.3291101 .

[257] T. Watanabe, A. Satou, T. Suemitsu, W. Knap, V. V. Popov, and T. Otsuji, in *CLEO: 2013* (Optica Publishing Group, 2013) p. CW3K.7.

[258] M. I. Dyakonov and M. S. Shur, Applied Physics Letters **67**, 1137 (1995), https://doi.org/10.1063/1.114986 .

[259] L. D. Landau and E. M. Lifshitz, *Course of Theoretical Physics: Fluid Mechanics 2nd Edition* (Pergamon, New York, 1987).

[260] P. Reimann, Physics Reports **361**, 57 (2002).

[261] P. Hänggi and F. Marchesoni, Rev. Mod. Phys. **81**, 387 (2009).

[262] C. O. Reichhardt and C. Reichhardt, Annual Review of Condensed Matter Physics **8**, 51 (2017), https://doi.org/10.1146/annurev-conmatphys-031016-025522 .

[263] M. Matsuo, D. A. Bandurin, Y. Ohnuma, Y. Tsutsumi, and S. Maekawa, "Spin hydrodynamic generation in graphene," (2020), arXiv:2005.01493 .

[264] G. Tatara, Phys. Rev. B **104**, 184414 (2021).

[265] H. Funaki, R. Toshio, and G. Tatara, Phys. Rev. Research **3**, 033075 (2021).

[266] M. M. Glazov, 2D Materials **9**, 015027 (2021).

[267] R. Sano, D. Oue, and M. Matsuo, "Valley hydrodynamics in gapped graphene," (2022), arXiv:2204.02409 .

[268] K. S. Denisov, K. A. Baryshnikov, and P. S. Alekseev, "Spin imaging of poiseuille flow of viscous electronic fluid," (2022), arXiv:2205.02647 .

[269] A. Jaoui, A. Gourgout, G. Seyfarth, A. Subedi, T. Lorenz, B. Fauqué, and K. Behnia, Phys. Rev. X **12**, 031023 (2022).

[270] X. Huang and A. Lucas, Phys. Rev. B **103**, 155128 (2021).

[271] E. M. Lifshitz and L. P. Pitaevskii, *Course of Theoretical Physics: Physical Kinetics* (Pergamon, New York, 1981).

[272] A. Lucas and K. C. Fong, Journal of Physics: Condensed Matter **30**, 053001 (2018).

[273] A. L. Fetter and J. D. Walecka, *Quantum Theory of Many-Particle Systems* (Pergamon, New York, 2003).

[274] Y. Hidaka, S. Pu, and D.-L. Yang, Phys. Rev. D **97**, 016004 (2018).

[275] D. Xiao, Y. Yao, Z. Fang, and Q. Niu, Phys. Rev. Lett. **97**, 026603 (2006).

[276] N. R. Cooper, B. I. Halperin, and I. M. Ruzin, Phys. Rev. B **55**, 2344 (1997).

[277] T. Yoda, T. Yokoyama, and S. Murakami, Scientific Reports **5**, 12024 (2015).

[278] T. Yoda, T. Yokoyama, and S. Murakami, Nano Letters **18**, 916 (2018).

[279] I. Sodemann and L. Fu, Phys. Rev. Lett. **115**, 216806 (2015).

[280] S. D. Ganichev, E. L. Ivchenko, S. N. Danilov, J. Eroms, W. Wegscheider, D. Weiss, and W. Prettl, Phys. Rev. Lett. **86**, 4358 (2001).

[281] J. E. Moore and J. Orenstein, Phys. Rev. Lett. **105**, 026805 (2010).

[282] S.-C. Ho, C.-H. Chang, Y.-C. Hsieh, S.-T. Lo, B. Huang, T.-H.-Y. Vu, C. Ortix, and T.-M. Chen, "Zero-magnetic-field hall effects in artificially corrugated bilayer graphene," (2019), arXiv:1910.07509 .

[283] R. Nakai and N. Nagaosa, Phys. Rev. B **99**, 115201 (2019).

[284] M. Papaj and L. Fu, Phys. Rev. Lett. **123**, 216802 (2019).

[285] Viscosity is defined through the momentum flux Π_{ij} as $\Pi_{ij} \propto \eta_{ijkl}\partial_k u_l$ and, without external fields, the form agrees with the conventional one in Ref.[259] under the approximation of the isotropic parabolic dispersion. Although additional viscosity terms will appear through the anomalous velocity when we apply electric field on the fluids, they contribute in the order of $E\partial u \sim \mathcal{O}(E^2)$ and thus are negligible in the present example.

[286] R. Toshio, K. Takasan, and N. Kawakami, Phys. Rev. Research **2**, 032021 (2020).

[287] P. S. Halasyamani and K. R. Poeppelmeier, Chemistry of Materials **10**, 2753 (1998), https://doi.org/10.1021/cm980140w .

[288] D. Puggioni and J. M. Rondinelli, Nature Communications **5**, 3432 (2014).

[289] N. Kumar, Y. Sun, N. Xu, K. Manna, M. Yao, V. Süss, I. Leermakers, O. Young, T. Förster, M. Schmidt, H. Borrmann, B. Yan, U. Zeitler, M. Shi, C. Felser, and C. Shekhar, Nature Communications **8**, 1642 (2017).

[290] C. Fu, T. Scaffidi, J. Waissman, Y. Sun, R. Saha, S. J. Watzman, A. K. Srivastava, G. Li, W. Schnelle, P. Werner, M. E. Kamminga, S. Sachdev, S. S. P. Parkin, S. A. Hartnoll, C. Felser, and J. Gooth, "Thermoelectric signatures of the electron-phonon fluid in ptsn4," (2018), arXiv:1802.09468 .

[291] D. Xiao, W. Yao, and Q. Niu, Phys. Rev. Lett. **99**, 236809 (2007).

[292] G. Giovannetti, P. A. Khomyakov, G. Brocks, P. J. Kelly, and J. van den Brink, Phys. Rev. B **76**, 073103 (2007).

[293] O. Tavakol and Y. B. Kim, Phys. Rev. Research **3**, 013290 (2021).

[294] E. H. Hasdeo, J. Ekström, E. G. Idrisov, and T. L. Schmidt, Phys. Rev. B **103**, 125106 (2021).

[295] C. Aversa and J. E. Sipe, Phys. Rev. B **52**, 14636 (1995).

[296] J. E. Sipe and A. I. Shkrebtii, Phys. Rev. B **61**, 5337 (2000).

[297] N. Nagaosa and T. Morimoto, Advanced Materials **29**, 1603345 (2017), https://onlinelibrary.wiley.com/doi/pdf/10.1002/adma.201603345 .

[298] J. Ahn, G.-Y. Guo, and N. Nagaosa, Phys. Rev. X **10**, 041041 (2020).

[299] H. Watanabe and Y. Yanase, Phys. Rev. X **11**, 011001 (2021).

[300] L. Z. Tan, F. Zheng, S. M. Young, F. Wang, S. Liu, and A. M. Rappe, npj Computational Materials **2**, 16026 (2016).

[301] A. M. Cook, B. M. Fregoso, F. de Juan, S. Coh, and J. E. Moore, Nature Communications **8**, 14176 (2017).

[302] J. Liu, F. Xia, D. Xiao, F. J. García de Abajo, and D. Sun, Nature Materials **19**, 830 (2020).

[303] H. Isobe, S.-Y. Xu, and L. Fu, Science Advances **6**, eaay2497 (2020), https://www.science.org/doi/pdf/10.1126/sciadv.aay2497 .

[304] Y. Zhang and L. Fu, Proceedings of the National Academy of Sciences **118**, e2100736118 (2021), https://www.pnas.org/doi/pdf/10.1073/pnas.2100736118 .

[305] W. Yang, Q. Liu, H. Wang, Y. Chen, R. Yang, S. Xia, Y. Luo, L. Deng, J. Qin, H. Duan, and L. Bi, Nature Communications **13**, 1719 (2022).

[306] S. Ke, B. Wang, and P. Lu, in *2015 IEEE MTT-S International Microwave Workshop Series on Advanced Materials and Processes for RF and THz Applications (IMWS-AMP)* (2015) pp. 1–1.

[307] K. Chaudhuri, M. Alhabeb, Z. Wang, V. M. Shalaev, Y. Gogotsi, and A. Boltasseva, ACS Photonics **5**, 1115 (2018).

[308] J. Huang, J. Li, Y. Yang, J. Li, J. Li, Y. Zhang, and J. Yao, Opt. Express **28**, 17832 (2020).

[309] A. Arora, M. S. Rudner, and J. C. W. Song, Nano Letters (2022), 10.1021/acs.nanolett.2c03126.

[310] V. V. Popov, O. V. Polischuk, T. V. Teperik, X. G. Peralta, S. J. Allen, N. J. M. Horing, and M. C. Wanke, Journal of Applied Physics **94**, 3556 (2003), https://doi.org/10.1063/1.1599051 .

[311] E. L. Ivchenko and M. I. Petrov, Physics of the Solid State **56**, 1833 (2014).

[312] V. V. Popov, D. V. Fateev, E. L. Ivchenko, and S. D. Ganichev, Phys. Rev. B **91**, 235436 (2015).

[313] R. Toshio and N. Kawakami, Phys. Rev. B **106**, L201301 (2022).

[314] M. Shur, *GaAs Devices and Circuits* (Plenum Press, New York, 1987).

[315] T. W. W. Maß, V. H. Nguyen, U. Schnakenberg, and T. Taubner, Opt. Express **27**, 10524 (2019).

[316] D. V. Fateev, V. V. Popov, and M. S. Shur, Semiconductors **44**, 1406 (2010).

[317] P. Olbrich, J. Karch, E. L. Ivchenko, J. Kamann, B. März, M. Fehrenbacher, D. Weiss, and S. D. Ganichev, Phys. Rev. B **83**, 165320 (2011).

[318] A. V. Muravjov, D. B. Veksler, V. V. Popov, O. V. Polischuk, N. Pala, X. Hu, R. Gaska, H. Saxena, R. E. Peale, and M. S. Shur, Applied Physics Letters **96**, 042105 (2010), https://doi.org/10.1063/1.3292019 .

[319] N. Guo, W.-D. Hu, X.-S. Chen, L. Wang, and W. Lu, Opt Express **21**, 1606 (2013).

[320] K. Li, J. M. Fitzgerald, X. Xiao, J. D. Caldwell, C. Zhang, S. A. Maier, X. Li, and V. Giannini, ACS Omega **2**, 3640 (2017).

[321] J. T. Hugall, A. Singh, and N. F. van Hulst, ACS Photonics **5**, 43 (2018).

[322] X. Xiao, X. Li, J. D. Caldwell, S. A. Maier, and V. Giannini, Applied Materials Today **12**, 283 (2018).

[323] I. Epstein, D. Alcaraz, Z. Huang, V.-V. Pusapati, J.-P. Hugonin, A. Kumar, X. M. Deputy, T. Khodkov, T. G. Rappoport, J.-Y. Hong, N. M. R. Peres, J. Kong, D. R. Smith, and F. H. L. Koppens, Science **368**, 1219 (2020), https://www.science.org/doi/pdf/10.1126/science.abb1570 .

[324] Z. Ullah, G. Witjaksono, I. Nawi, N. Tansu, M. Irfan Khattak, and M. Junaid, Sensors **20** (2020), 10.3390/s20051401.

[325] Q. Ma, S.-Y. Xu, H. Shen, D. MacNeill, V. Fatemi, T.-R. Chang, A. M. Mier Valdivia, S. Wu, Z. Du, C.-H. Hsu, S. Fang, Q. D. Gibson, K. Watanabe, T. Taniguchi, R. J. Cava, E. Kaxiras, H.-Z. Lu, H. Lin, L. Fu, N. Gedik, and P. Jarillo-Herrero, Nature **565**, 337 (2019).

[326] G. Auton, J. Zhang, R. K. Kumar, H. Wang, X. Zhang, Q. Wang, E. Hill, and A. Song, Nature Communications **7**, 11670 (2016).

[327] C.-P. Zhang, J. Xiao, B. T. Zhou, J.-X. Hu, Y.-M. Xie, B. Yan, and K. T. Law, Phys. Rev. B **106**, L041111 (2022).

[328] S.-Y. Xu, Q. Ma, H. Shen, V. Fatemi, S. Wu, T.-R. Chang, G. Chang, A. M. M. Valdivia, C.-K. Chan, Q. D. Gibson, J. Zhou, Z. Liu, K. Watanabe, T. Taniguchi, H. Lin, R. J. Cava, L. Fu, N. Gedik, and P. Jarillo-Herrero, Nature Physics **14**, 900 (2018).

[329] Y. Cao, D. Chowdhury, D. Rodan-Legrain, O. Rubies-Bigorda, K. Watanabe, T. Taniguchi, T. Senthil, and P. Jarillo-Herrero, Phys. Rev. Lett. **124**, 076801 (2020).

[330] J. González and T. Stauber, Phys. Rev. Lett. **124**, 186801 (2020).

[331] P. Cha, A. A. Patel, and E.-A. Kim, Phys. Rev. Lett. **127**, 266601 (2021).

[332] S. Das Sarma and F. Wu, Phys. Rev. Research **4**, 033061 (2022).

[333] Z. Qian and G. Vignale, Phys. Rev. B **71**, 075112 (2005).

[334] R. A. Davison, K. Schalm, and J. Zaanen, Phys. Rev. B **89**, 245116 (2014).

[335] B. N. Narozhny, Annals of Physics **411**, 167979 (2019).

[336] H. Wang and X. Qian, npj Computational Materials **5**, 119 (2019).

[337] K. Kang, T. Li, E. Sohn, J. Shan, and K. F. Mak, Nature Materials **18**, 324 (2019).

[338] S.-C. Ho, C.-H. Chang, Y.-C. Hsieh, S.-T. Lo, B. Huang, T.-H.-Y. Vu, C. Ortix, and T.-M. Chen, Nature Electronics **4**, 116 (2021).

[339] Z. He and H. Weng, npj Quantum Materials **6**, 101 (2021).

[340] H. Diehl, V. A. Shalygin, V. V. Bel'kov, C. Hoffmann, S. N. Danilov, T. Herrle, S. A. Tarasenko, D. Schuh, C. Gerl, W. Wegscheider, W. Prettl, and S. D. Ganichev, New Journal of Physics **9**, 349 (2007).

[341] M. Zarenia, I. Yudhistira, S. Adam, and G. Vignale, Phys. Rev. B **101**, 045421 (2020).

[342] M. Freitag, T. Low, W. Zhu, H. Yan, F. Xia, and P. Avouris, Nature Communications **4**, 1951 (2013).

[343] J. Guo, R. Xiang, T. Cheng, S. Maruyama, and Y. Li, ACS Nanoscience Au **2**, 3 (2022).

[344] T.-T. Kim, S. S. Oh, H.-D. Kim, H. S. Park, O. Hess, B. Min, and S. Zhang, Science Advances **3**, e1701377 (2017), https://www.science.org/doi/pdf/10.1126/sciadv.1701377 .

[345] V. V. Popov, Applied Physics Letters **102**, 253504 (2013), https://doi.org/10.1063/1.4811706 .

[346] H. Shokri Kojori, J.-H. Yun, Y. Paik, J. Kim, W. A. Anderson, and S. J. Kim, Nano Letters **16**, 250 (2016).

[347] H. Yan, X. Li, B. Chandra, G. Tulevski, Y. Wu, M. Freitag, W. Zhu, P. Avouris, and F. Xia, Nature Nanotechnology **7**, 330 (2012).

[348] Y. Zhang, Y. Sun, and B. Yan, Phys. Rev. B **97**, 041101 (2018).

[349] J. Hofmann and S. Das Sarma, Phys. Rev. B **93**, 241402 (2016).

[350] J. C. W. Song and M. S. Rudner, Phys. Rev. B **96**, 205443 (2017).

[351] T. Tamaya, T. Kato, K. Tsuchikawa, S. Konabe, and S. Kawabata, Journal of Physics: Condensed Matter **31**, 305001 (2019).

Acknowledgments

First, I would like to express my gratitude to Prof. Norio Kawakami for his kind help during my master and doctoral courses. His support ranges from his insightful suggestions on physics to his advice on everyday life. His supervision is essential for the completion of my works so far.

I am grateful to Mr. Ryotaro Sano, Dr. Kazuaki Takasan, Dr. Hiroshi Funaki, and Prof. Gen Tatara for the collaboration in my studies on electron hydrodynamics so far. They provide me with deep insight into electron hydrodynamics in terms of nonlinear optics and spintronics, and the fruitful discussion with them stimulated me, leading to the motivations of my studies. I also thank Dr. Hikaru Watanabe, Prof. Atsuo Shitade and Prof. Akito Daido for having various discussions on quantum geometry and nonlinear optics, and giving me a lot of helpful advices.

In terms of my daily life in Condensed Matter Theory group of Kyoto University, I would like to thank the staffs, Prof. Youichi Yanase, Prof. Ryusuke Ikeda, Prof. Robert Peters, Prof. Masaki Tezuka, Prof. Tsuneya Yoshida, and Prof. Akito Daido for their support. I have enjoyed various discussions on physics and other topics with my colleagues, Mr. Ryotaro Sano, Mr. Kosuke Nogaki, Mr. Shin Kaneshiro, and all the other members in my group. I acknowledge the financial supports from JSPS Research Fellowship for Young Scientists (JSPS KAKENHI No. 20J22612) and WISE program of MEXT.

Last but not least, I would like to express my deepest gratitude to my family for their continuous support during my life from the birth to the present. I also would like to thank my friends for giving me spent and enjoyable times.